

Formation of Black Powder Components by Dewing and Hygroscopic Corrosion
Processes

A thesis presented to
the faculty of
the Russ College of Engineering and Technology of Ohio University

In partial fulfillment
of the requirement for the degree
Master of Science

Martin L. Colahan

April 2017

© 2017 Martin L. Colahan. All Rights Reserved

This thesis titled
Formation of Black Powder Components by Dewing and Hygroscopic Corrosion
Processes

by

MARTIN L. COLAHAN

has been approved for
the Department of Chemical and Biomolecular Engineering
and the Russ College of Engineering and Technology by

David Young

Research Associate Professor of Chemical and Biomolecular Engineering

Dennis Irwin

Dean, Russ College of Engineering and Technology

ABSTRACT

COLAHAN, MARTIN L., M.S., April 2017, Chemical Engineering

Formation of Black Powder Components by Dewing and Hygroscopic Corrosion Processes

Director of Thesis: David Young

The presence of black powder in natural gas pipelines can lead to equipment erosion, valve failure, instrumentation malfunction, and increased pressure drop. However, despite its impact on downstream and midstream operations, black powder production is poorly understood. In the present work, black powder formation as a result of corrosion was investigated by simulating sales gas conditions in a glass cell. Steel specimens were systematically exposed to a range of CO₂, H₂S, and O₂ partial pressures at differing water condensation rates. The potential for hygroscopic material assisting black powder formation was also investigated. Friable corrosion products found in dewing conditions consisted of siderite, mackinawite, and hematite. Buckle-driven delamination was identified as a leading cause of black powder production from FeS. The presence of hygroscopic NaCl crystals facilitated corrosion at relative humidities as low as 33%, but flakey corrosion products were only found if deliquescence occurred.

DEDICATION

In memory of my beloved aunt:

Jamell Faith Cazer

1973 – 2014

ACKNOWLEDGEMENTS

I would like express my deepest gratitude to my family and friends for without their support none of this work would have been possible.

I would also like to thank my thesis committee members Dr. Marc Singer, Dr. Rebecca Barlag, Dr. Kevin Crist, and Dr. Srdjan Nestic for their guidance. A special thanks go to the technical staff at the Institute for Corrosion and Multiphase Technology (ICMT) namely Mr. Cody Shafer, Mr. Al Schubert, Mr. Alexis Barxias, and Mr. Phil Bullington for their technical expertise and assistance with my experimental work. I would like to thank The Petroleum Institute in Abu Dhabi, United Arab Emirates for their financial support. A special thanks goes to Dr. Bruce Brown of the ICMT, and Dr. Ricardo Nogueira and Dr. Yves Gunaltun of The Petroleum Institute for their support and insightful discussions.

Last but certainly not least, I would like to thank my advisor, Dr. David Young. One could not ask for a better mentor. His steady guidance has been the foundation to all the work herein and has helped me remember why I fell in love with science and engineering as a child. Thank you so very much.

TABLE OF CONTENTS

	Page
Abstract.....	3
Dedication.....	4
Acknowledgements.....	5
List of Tables	9
List of Figures.....	10
Chapter 1: Introduction.....	16
Chapter 2: Background and Literature Review	20
2.1 Sales Gas	20
2.2 Corrosion of Steel in Oil and Gas Environments.....	22
2.2.1 Water Chemistry.....	23
2.2.2 Formation of Corrosion Product Layers	25
2.2.3 Effect of O ₂ on CO ₂ and H ₂ S Corrosion.....	27
2.2.4 Crystal Structures of Corrosion Product Species.....	28
2.3 Black Powder	29
2.4 Water Availability.....	31
2.4.1 Top-of-the-Line Corrosion.....	33
2.4.2 Hygroscopic Uptake of Water by Salts.....	35
2.4.3 Hygroscopic Corrosion	36
2.5 Gaps in Understanding Black Powder Formation.....	40
Chapter 3: Research Objectives and Hypotheses	41

	7
3.1 Objective	41
3.2 Hypotheses	41
3.3 Motivation	42
Chapter 4: Methodology and Experimental Design	43
4.1 Overview	43
4.2 Test Conditions	43
4.3 Black Powder Formation in Dewing Conditions	46
4.3.1 Dewing Corrosion Equipment	46
4.3.2 Dewing Corrosion Experimental Procedures.....	51
4.4 Black Powder Formation in Hygroscopic Conditions.....	52
4.4.1 Hygroscopic Corrosion Equipment and Procedures	52
4.5 Analytical Methods	55
4.6 Safety.....	56
Chapter 5: Results and Discussion	58
5.1 Dewing Corrosion	58
5.1.1 Effect of H ₂ S Partial Pressure on Dewing Corrosion	58
5.1.2 Effect of Time on Sour Dewing Corrosion.....	66
5.1.3 FeS Layer Buckling	70
5.1.4 Effect of O ₂ on Sweet Dewing Corrosion.....	72
5.1.5 Effect of Cyclic Water Condensation	77
5.1.6 Black Powder Formation in Dewing Conditions	82
5.2 Hygroscopic Corrosion	84

	8
5.2.1 Salt Layer Generation	84
5.2.2 Hygroscopic Corrosion in Sweet Environments.....	86
5.2.3 Hygroscopic Corrosion in Sour Environments.....	93
5.2.4 Corrosion Below the Deliquescence Relative Humidity	101
5.2.5 Black Powder Formation through Hygroscopic Corrosion Processes	103
5.3 Experiment Repeatability.....	104
Chapter 6: Conclusions and Future Work	106
6.1 Summary of Results	106
6.2 Hypotheses Revisited	106
6.3 Comments on Black Powder Mitigation	108
6.4 Future Work	108
References.....	110
Appendix A: Peltier Temperature Controller Design.....	115
Appendix B: Calculations	119
Appendix C: Additional Microscopy.....	123

LIST OF TABLES

	Page
Table 1: Typical sales gas specifications pertinent to black powder formation [7].....	21
Table 2: Typical H ₂ S, CO ₂ , O ₂ , and H ₂ O sales gas specifications and measured levels within the Saudi Aramco sales gas network [8].....	21
Table 3: Common phases found in corrosion products formed in CO ₂ , H ₂ S, and O ₂ corrosion	29
Table 4: Sales gas composition from which experimental parameters are derived.....	44
Table 5: Composition of API 5L X65 steel used for testing (wt.%).....	45
Table 6: Test matrix for studying the effect of H ₂ S partial pressure on dewing corrosion.	59
Table 7: Test matrix for analyzing the effect of time on sour dewing systems	66
Table 8: Test matrix for the investigation of the effect of O ₂ on sweet dewing corrosion.....	72
Table 9: Test matrix for the investigation of the effect of cyclic water condensation.....	77
Table 10: Hygroscopic corrosion test matrix.....	84

LIST OF FIGURES

	Page
Figure 1: Turbine blade eroded due to exposure to black powder. Reproduced with permission from NACE International, Houston, TX. All rights reserved. Smart, Paper 11089 presented at CORROSION/2011, Houston, TX. © NACE International 2011 [6].	18
Figure 2: (a) Measured dew point temperatures and (b) corresponding moisture contents of sales gas measured during July and February at sampling locations in the Saudi Aramco sales gas network [8].	32
Figure 3: Ambient temperatures in the Eastern Province of Saudi Arabia. Points below the red dotted line indicate times when dew may form in the pipeline. Reproduced with permission from NACE International, Houston, TX. All rights reserved. A.M. Sherik, S.R. Zaidi, E.V. Tuzan, J.P. Perez, Paper 08415 presented at CORROSION/2008, New Orleans, LA. © NACE International 2008 [8].	33
Figure 4: Flaky FeS corrosion product produced in marginally sour TLC conditions. (Test Conditions: Duration: 7 days, p_{H_2S} : 0.15 H_2S , p_{CO_2} : 0.93 bar, Water Condensation Rate: 0.25 ± 0.04 ml/m ² /s, T_{gas} : 40°C, T_{steel} : 28°C T_{steel}). Reproduced with permission from NACE International, Houston, TX. All rights reserved. N. Yaakob, F. Farelas, M. Singer, S. Nesic, D. Young, Paper 7695 presented at CORROSION/2016, Vancouver, BC. © NACE International 2016 [37].	35
Figure 5: (a) Corrosion rates and (b) optical images taken after extraction of specimens with NaCl deposits exposed to CO ₂ /H ₂ S gas mixtures with the indicated relative humidity. Reproduced with permission from NACE International, Houston, TX. All rights reserved. W. Litke, J. Bojes, P. Blais, J. Lerbscher, W. Wamburi, Paper 2339 presented at CORROSION/2013, Orlando, FL. © NACE International 2013. [42]	38
Figure 6: (a) Corrosion rates and (b) optical images taken after extraction of specimens with MgCl ₂ deposits exposed to CO ₂ /H ₂ S gas mixtures with the indicated relative humidity. Reproduced with permission from NACE International, Houston, TX. All rights reserved. W. Litke, J. Bojes, P. Blais, J. Lerbscher, W. Wamburi, Paper 2339 presented at CORROSION/2013, Orlando, FL. © NACE International 2013. [42]	39
Figure 7: Microstructure of the X65 steel specimens. Ferrite and cementite are found in the dark and white locations, respectively.	45
Figure 8: Dewing corrosion glass cell. Image courtesy of Cody Shafer.	48

Figure 9: Specimen holding and control stack including (A) specimen holder, (B) Peltier, (C) Water cooled heat sink, and (D) Anchor bar and bolts. Image courtesy of Cody Shafer.	49
Figure 10: XRD specimen holder. Image courtesy of Cody Shafer.	49
Figure 11: Hygroscopic corrosion glass cell. Image courtesy of Cody Shafer.	53
Figure 12: Effect of H ₂ S partial pressure and water condensation rate on corrosion product morphology.	61
Figure 13: XRD data showing the effect of H ₂ S partial pressure and WCR on corrosion product composition.	62
Figure 14: Effect of H ₂ S partial pressure and water condensation rate on corrosion rate.	63
Figure 15: Effect of H ₂ S partial pressure and water condensation rate (L = low, H = high) on the measured and theoretical corrosion product masses.	64
Figure 16: Effect of H ₂ S partial pressure on maximum possible black powder production rate in a 100 km, 42 inch ID pipeline.	65
Figure 17: Effect of Time on Corrosion Product Morphology (0.3 mbar H ₂ S, 0.96 bar CO ₂ , 0 mbar O ₂ , 0.015 ml/m ² /s WCR, 25 T _{steel} , 30°C T _{gas}).	67
Figure 18: Effect of time on corrosion product composition.	68
Figure 19: Effect of time on corrosion rate at 0.3 mbar pH ₂ S and low WCR.	69
Figure 20: Effect of time on (a) corrosion product mass and (b) maximum possible black powder production rate in a 100 km long, 42 in. ID pipeline at 0.3 mbar pH ₂ S and low WCR.	70
Figure 21: Effect of O ₂ on (a) corrosion rate, (b) measured and theoretical corrosion product mass, and (c) maximum possible black powder production rate in a 100 km, 42 in. ID pipeline.	73
Figure 22: Surface analysis of corrosion products formed after a 3 day exposure to a 10 mbar O ₂ – 0.92 bar CO ₂ atmosphere at the low WCR.	75
Figure 23: (a) XRD and (b) Raman spectroscopy compositional analysis of corrosion product formed after a 3-day exposure to a 10 mbar O ₂ – 0.92 bar CO ₂ atmosphere at the low WCR. The red hematite spectrum is added as a reference [50].	76
Figure 24: Effect of cyclic water condensation on corrosion product morphology.	79
Figure 25: Effect of cyclic water condensation on the corrosion product composition. ..	80

Figure 26: Effect of temperature cycling on (a) corrosion rate, (b) measure and theoretical corrosion product mass, and (c) maximum possible black powder production rate in a 100 km, 42 in. ID pipeline.	81
Figure 27: SEM analysis of the NaCl layer formed before specimen insertion into test environment. The specimen was coated with palladium to minimize electron beam charging.....	85
Figure 28: Slight localized corrosion on the outside boundary of a salt crystal formed by drying NaCl.....	86
Figure 29: (a) Surface microscopy after a 3 day exposures to CO ₂ atmosphere at 75% RH. The region outlined in red is enlarged in (b).....	87
Figure 30: EDS of corrosion product after a 3 day exposure to a CO ₂ environment at 75% RH. NQ: Not Quantified.	88
Figure 31: XRD corrosion product composition analysis of specimens recovered after a 3 day exposure to CO ₂ at 75% RH. Peak labels are S: siderite (FeCO ₃), H: halite (NaCl), and Fe: ferrite (Fe).	88
Figure 32: Surface profilometry of specimen recovered after a 3 day exposure to CO ₂ at 75% RH. Scale bar units are in nm.	90
Figure 33: Surface microscopy and XRD compositional analysis after a 3 day exposure to CO ₂ at 58 and 33% RH.	91
Figure 34: Effect of relative humidity on (a) general corrosion rate, (b) measured and theoretical corrosion product mass, and (c) maximum possible black powder production rate in a 100 km, 42 in. ID pipeline under hygroscopic CO ₂ conditions.	92
Figure 35: Effect of H ₂ S partial pressure on corrosion product morphology in deliquescing conditions (75% RH, 0.97 bar CO ₂).	94
Figure 36: Effect of H ₂ S partial pressure on corrosion product composition. Phases are M: mackinawite, S: siderite, H: halite, and Fe: ferrite. Peaks labeled with an asterisk (*) correspond to unknown phases.	96
Figure 37: Effect of H ₂ S partial pressure on surface morphology at 58 and 33% RH.	97
Figure 38: Effect of H ₂ S partial pressure on corrosion product composition. Phases are M: mackinawite, H: halite, and Fe: ferrite.	99
Figure 39: Effect of H ₂ S partial pressure on (a) general corrosion rate, (b) measured and theoretical corrosion product mass, and (c) maximum possible black powder production rate in a 100 km, 42 in. ID pipeline under hygroscopic conditions.	100

Figure 40: Peltier controller schematic.	116
Figure 41: Cross-section view of the XRD specimen holder. Image courtesy of Cody Shafer.	118
Figure 42: Conditions: p_{H_2S} : 0 mbar, p_{CO_2} : 0.96 bar, WCR: 0.05 ml/m ² /s, Steel Temperature: 15°C, Gas Temperature: 30°C, Duration: 3 days.	123
Figure 43: Conditions: p_{H_2S} : 0 mbar, p_{CO_2} : 0.96 bar, WCR: 0.015 ml/m ² /s, Steel Temperature: 25°C, Gas Temperature: 30°C, Duration: 3 days. Images (a) and (b) were from the same test as that shown in Chapter 5, whereas images (c)-(f) were from a test with inconclusive gravimetric measurements. The corrosion product in the inconclusive test was of a similar morphology to the CO ₂ /O ₂ test.	124
Figure 44: Conditions: p_{H_2S} : 0.1 mbar, p_{CO_2} : 0.96 bar, WCR: 0.05 ml/m ² /s, Steel Temperature: 15°C, Gas Temperature: 30°C, Duration: 3 days.	125
Figure 45: Conditions: p_{H_2S} : 0.1 mbar, p_{CO_2} : 0.96 bar, WCR: 0.015 ml/m ² /s, Steel Temperature: 25°C, Gas Temperature: 30°C, Duration: 3 days.	125
Figure 46: Conditions: p_{H_2S} : 0.3 mbar, p_{CO_2} : 0.96 bar, WCR: 0.05 ml/m ² /s, Steel Temperature: 15°C, Gas Temperature: 30°C, Duration: 3 days.	126
Figure 47: Conditions: p_{H_2S} : 0.3 mbar, p_{CO_2} : 0.96 bar, WCR: 0.015 ml/m ² /s, Steel Temperature: 25°C, Gas Temperature: 30°C, Duration: 6 hours.	126
Figure 48: Conditions: p_{H_2S} : 0.3 mbar, p_{CO_2} : 0.96 bar, WCR: 0.015 ml/m ² /s, Steel Temperature: 25°C, Gas Temperature: 30°C, Duration: 1 day.	127
Figure 49: Conditions: p_{H_2S} : 0.3 mbar, p_{CO_2} : 0.96 bar, WCR: 0.015 ml/m ² /s, Steel Temperature: 25°C, Gas Temperature: 30°C, Duration: 3 days.	128
Figure 50: Conditions: p_{H_2S} : 0.3 mbar, p_{CO_2} : 0.96 bar, WCR: 0.015 ml/m ² /s, Steel Temperature: 25°C, Gas Temperature: 30°C, Duration: 7 days.	129
Figure 51: Conditions: p_{H_2S} : 0.3 mbar, p_{CO_2} : 0.96 bar, WCR: 0.015 ml/m ² /s, Steel Temperature: 25°C, Gas Temperature: 30°C, Duration: 10 days.	130
Figure 52: Conditions: p_{H_2S} : 1.0 mbar, p_{CO_2} : 0.96 bar, WCR: 0.05 ml/m ² /s, Steel Temperature: 15°C, Gas Temperature: 30°C, Duration: 3 days.	131
Figure 53: Conditions: p_{H_2S} : 1.0 mbar, p_{CO_2} : 0.96 bar, WCR: 0.015 ml/m ² /s, Steel Temperature: 25°C, Gas Temperature: 30°C, Duration: 3 days.	132
Figure 54: Conditions: p_{H_2S} : 0.3 mbar, p_{CO_2} : 0.96 bar, WCR: 0.015 ml/m ² /s, Steel Temperature: 25°C, Gas Temperature: 30°C, Duration: 6 hours.	133

Figure 55: Conditions: p_{H_2S} : 0.3 mbar, p_{CO_2} : 0.96 bar, WCR: 0.015/0 ml/m ² /s, Steel Temperature: 25/40°C, Gas Temperature: 30°C, Duration: 3 days, Cycle Period: 1 day.	134
Figure 56: Conditions: p_{H_2S} : 0.3 mbar, p_{CO_2} : 0.96 bar, WCR: 0.015/0 ml/m ² /s, Steel Temperature: 25/40°C, Gas Temperature: 30°C, Duration: 7 days, Cycle Period: 1 day.	135
Figure 57: Conditions: p_{H_2S} : 0 mbar, p_{CO_2} : 0.96 bar, RH: 75%, Temperature: 25°C, Duration: 3 days, Salt Layer Composition: NaCl. (d) and (e): after DI water rinse, (f): after Clarke.....	136
Figure 58: Conditions: p_{H_2S} : 0 mbar, p_{CO_2} : 0.96 bar, RH: 58%, Temperature: 25°C, Duration: 3 days, Salt Layer Composition: NaCl. Micrograph (a): after extraction, (b): after DI water rinse, and (c): after Clarke.	137
Figure 59: Conditions: p_{H_2S} : 0 mbar, p_{CO_2} : 0.96 bar, RH: 33%, Temperature: 25°C, Duration: 3 days, Salt Layer Composition: NaCl. Micrograph (a): after extraction, (b): after DI water rinse, and (c): after Clarke.	138
Figure 60: Conditions: p_{H_2S} : 0.1 mbar, p_{CO_2} : 0.96 bar, RH: 75%, Temperature: 25°C, Duration: 3 days, Salt Layer Composition: NaCl.....	139
Figure 61: Conditions: p_{H_2S} : 0.1 mbar, p_{CO_2} : 0.96 bar, RH: 58%, Temperature: 25°C, Duration: 3 days, Salt Layer Composition: NaCl.	139
Figure 62: Conditions: p_{H_2S} : 0.1 mbar, p_{CO_2} : 0.96 bar, RH: 33%, Temperature: 25°C, Duration: 3 days, Salt Layer Composition: NaCl.	140
Figure 63: Conditions: p_{H_2S} : 0.3 mbar, p_{CO_2} : 0.97 bar, RH: 75%, Temperature: 25°C, Duration: 3 days, Salt Layer Composition: NaCl.	141
Figure 64: Conditions: p_{H_2S} : 0.3 mbar, p_{CO_2} : 0.97 bar, RH: 58%, Temperature: 25°C, Duration: 3 days, Salt Layer Composition: NaCl.	142
Figure 65: Conditions: p_{H_2S} : 0.3 mbar, p_{CO_2} : 0.97 bar, RH: 33%, Temperature: 25°C, Duration: 3 days, Salt Layer Composition: NaCl.	142
Figure 66: Conditions: p_{H_2S} : 1.0 mbar, p_{CO_2} : 0.97 bar, RH: 75%, Temperature: 25°C, Duration: 3 days, Salt Layer Composition: NaCl. (c): after DI water rinse, (d): after Clarke.....	143
Figure 67: Conditions: p_{H_2S} : 1.0 mbar, p_{CO_2} : 0.97 bar, RH: 58%, Temperature: 25°C, Duration: 3 days, Salt Layer Composition: NaCl. Micrographs (c) and (d): after DI water rinse.	144

Figure 68: Conditions: p_{H_2S} : 1.0 mbar, p_{CO_2} : 0.97 bar, RH: 33%, Temperature: 25°C, Duration: 3 days, Salt Layer Composition: NaCl. Micrographs (c) and (d): after DI water rinse..... 145

CHAPTER 1: INTRODUCTION

The global economy is driven by the consumption of useful forms of energy. Historically, energy demand in the industrialized world has largely been fulfilled through the consumption of fossil fuels such as coal, oil, and natural gas. Investments into alternative energy sources (e.g., wind, solar, and nuclear energy) have been made in an attempt to diversify the global energy portfolio, but limitations including supply intermittency, energy storage, and large up-front capital costs currently prevent the overall transformation from a fossil fuel based economy into an alternative energy based economy.

Unless groundbreaking discoveries are made in alternative energy, the consumption of fossil fuels is likely to remain a primary source of energy. The United States Energy Information Administration (EIA) [1] projects global energy consumption to increase by 48% between the years 2012 and 2040 to 815 quadrillion Btu, fossil fuels are expected to supply 78% of this demand. The energy source with the largest increase in consumption is projected to be natural gas. The abundance and low cost of natural gas makes it an economically attractive energy source, particularly for the industrial and electrical power generation sectors. Governmental policies aimed at reducing greenhouse gas emissions also make natural gas attractive as it generates significantly less CO₂ per kWh produced, as well as combusting more cleanly, than both coal and liquid fossil fuels [2].

Natural gas is a byproduct of the decomposition of plant and animal matter trapped underground at high pressures and temperatures over millions of years. The resulting hydrocarbon-rich mixture is extracted from geologic reservoirs, processed to separate the more valuable components, and remove the majority of undesired components. The

processed methane-rich gas, commonly known as sales gas, is transported to the consumer through a network of pipelines. In 2008, the EIA estimated the network of natural gas pipelines in the continental U.S. to be approximately 305,000 miles (490,000 kilometers) long, but the recent boom in natural gas production from unconventional sources (e.g., shale or tight gas reservoirs) means that this length will continue to increase [3].

A challenge to the operation of natural gas pipelines is corrosion, which can weaken the integrity of the pipeline and ultimately may render the costly structure useless unless mitigated. Internal corrosion in the oil and gas industry is mostly due to water wetting the steel surface in the presence of acid gases including carbon dioxide (CO_2) and hydrogen sulfide (H_2S). Processed natural gas can contain small concentrations of water, carbon dioxide, hydrogen sulfide, and potentially oxygen that can be corrosive to the steel pipeline transporting the gas. Products formed as a result of corrosion may spall off the steel surface and become entrained in the gas becoming what is commonly known in the oil and gas industry as “black powder” [4].

Black powder is a collective term used to generally describe particles that can be entrained in the gas. Black powder is a problem for pipeline operators as it can erode equipment, induce greater pressure drops, and clog instrumentation [4]. The erosive power of entrained particles can be seen in Figure 1, which shows a power plant turbine blade after exposure to black powder. Black powder particles vary in size and can range from 100 nm up 1 mm [5]. The composition of black powder can also vary and can include corrosion products, salt, dirt, and other materials trapped in the pipeline during construction. The production of black powder is most significant in gas transmissions

pipelines. Transmission pipelines are large capacity pipelines that deliver gas from processing plants to the consumer or distributor. These pipelines are designed to move large quantities of natural gas over long distances so, therefore, have large diameters and high operating pressures.



Figure 1: Turbine blade eroded due to exposure to black powder. Reproduced with permission from NACE International, Houston, TX. All rights reserved. Smart, Paper 11089 presented at CORROSION/2011, Houston, TX. © NACE International 2011 [6].

Although investigations into the impact of black powder have been performed, its formation processes remain poorly understood. The present study investigates black powder formation by examining the effect of CO_2 , H_2S , and O_2 on the corrosion of steel in both water condensing conditions and humid conditions where hygroscopic material assists wetting the steel surface. Research performed to investigate black powder formation is described in this thesis as follows:

- Chapter 2 reviews pertinent literature related to black powder formation and provides a foundation for work described thereafter.
- Chapter 3 describes research objectives and proposes hypotheses regarding black powder formation.
- Chapter 4 discusses the methodologies and experimental equipment used to test black powder formation in simulated sales gas environments.
- Chapter 5 presents and discusses results obtained during experimentation.
- Chapter 6 summarizes black powder research described in the preceding chapters and proposes future work to better understand black powder formation and ideas for the mitigation of black powder in gas transmission pipelines.

CHAPTER 2: BACKGROUND AND LITERATURE REVIEW

Black powder in gas pipelines is a costly problem for which effective mitigation strategies are desired. Previous studies on black powder have tended to focus on its behavior rather than formation, consequently, additional information is required to develop superior mitigation strategies. A review of black powder literature was conducted by Khan and Al-Shehhi [5] that examined black powder composition, formation, entrainment, transport, and filtration. Due to the wide variety of topics covered, the review serves as an excellent resource for engineers in the field with a black powder problem, but the review of formation mechanisms was limited by the lack of available data in the scientific literature. Black powder formation through corrosion processes is reviewed in more detail in this chapter.

2.1 Sales Gas

Compositions will vary, but sales gas is composed primarily of methane (CH_4). Larger hydrocarbon molecules such as ethane (C_2H_6) can be present, but their concentrations are very low. Low concentrations of water (H_2O), nitrogen (N_2), carbon dioxide (CO_2), hydrogen sulfide (H_2S), and sulfur-containing species such as methyl mercaptan (CH_3SH , added as a malodorant) are often present in sales gas, but a ceiling content is generally specified to ensure the processed natural gas meets a gross heating value and minimizes corrosion. Typical sales gas specifications pertinent to black powder are given in Table 1 below [7].

Table 1: Typical sales gas specifications pertinent to black powder formation [7]

Specification	Value
Water Content	4-7 lbm H ₂ O/MMscf
CO ₂ Content	3-4 mol%
N ₂ Content	4-5 mol%
Maximum O ₂ Content	0.01 mol%
H ₂ S Content	0.25-1.0 grain/100 scf
Total Sulfur Content	0.5-20 grain/100 scf
Gross Heating Value	950-1200 Btu/scf
Solids and Free Liquid	Commercially free

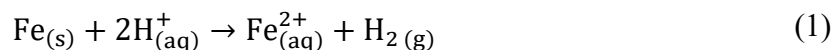
Typical specifications and measured levels of CO₂, H₂S, O₂, and H₂O were published in a black powder study by Sherik, *et al.*, [8] and are shown in Table 2. H₂S, CO₂, and O₂ levels were typically within limits, but the water content was consistently over the 0.112 mg/L (7 lbs/MMscf) limit. The higher than specification water contents may render the pipeline susceptible for liquid water to form and subsequently allow corrosion to occur.

Table 2: Typical H₂S, CO₂, O₂, and H₂O sales gas specifications and measured levels within the Saudi Aramco sales gas network [8].

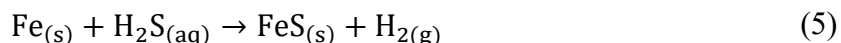
Component	Typical Sales Gas Specifications (maximum limits)	Measured Levels
H ₂ S (ppm)	16	1-15
O ₂ (mol%)	0.02	0.01-0.03
CO ₂ (mol%)	3	<1.62
H ₂ O (mg/L)	0.112	0.12-0.55

2.2 Corrosion of Steel in Oil and Gas Environments

Both CO₂ and H₂S are considered acid gases due to their ability to form hydrogen ions in water *via* dissociation processes. The H⁺ will react with iron at the steel surface in an overall reaction given by Reaction 1. This electrochemical reaction can be broken into an oxidation reaction, Reaction 2, and a reduction reaction, Reaction 3.



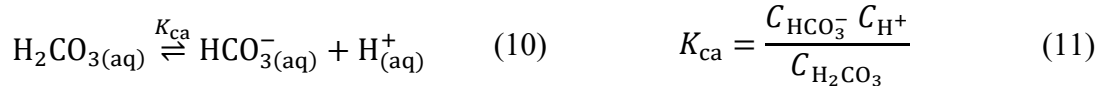
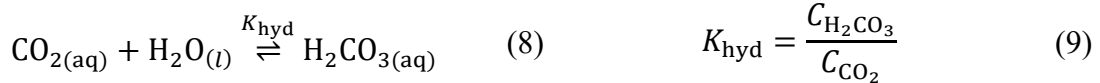
If CO₂ and H₂S are included in the bulk gas, additional electrochemical reactions need consideration. Carbonic acid has been postulated to directly react with the steel by the reduction reaction given in Reaction 4, but this direct reaction mechanism is under dispute in favor of a “buffering” mechanism [9]. Conversely, H₂S is known to directly react with the steel in the overall reaction shown in Reaction 5 [10].



The rate at which the electrochemical reactions encountered in corrosion proceed is dependent upon the charge transfer rate and the concentration of the oxidants at the steel surface. The oxidant concentration at the surface is determined by both mass transfer and the bulk concentration, which is governed by water chemistry. The effect of CO₂ and H₂S on the water chemistry is explored further in the following sections [10].

2.2.1 Water Chemistry

The acidification of water caused by carbon dioxide takes place through several steps. These steps include the dissolution of CO₂ (Reaction 6), the hydration of CO₂ to form carbonic acid (Reaction 8), the first dissociation step of carbonic acid to form bicarbonate ions (Reaction 10), and the dissociation of bicarbonate ions to form carbonate ions (Reaction 12). The equilibrium constants are denoted in the reactions and are also defined as equilibrium expressions [11], [12].



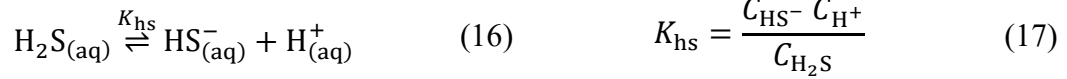
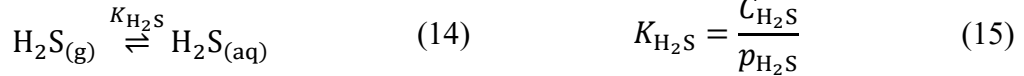
where:

C_i = concentration of species i (molar)

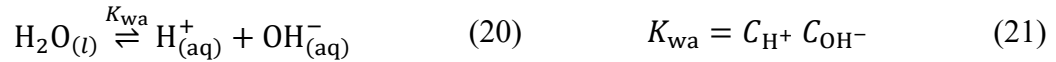
p_i = partial pressure of gas i (bar)

K_i = equilibrium constant of reaction i

With the exception of the lack of a hydration step, the acidification of water due to H₂S is similar to that of CO₂. H₂S does not require hydration to dissociate. To acidify water, H₂S first dissolves (Reaction 14) and then dissociates into bisulfide ions (Reaction 16), which can dissociate further into sulfide ions (Reaction 18). Each dissociation step forms hydrogen ions which can be reduced during the corrosion process [13]–[15].



Additionally, water can dissociate (Reaction 20) [15].



Several correlations to calculate the equilibrium constants defined above are given in Equations 22-29 below [11]–[15]:

$$K_{\text{CO}_2} = \frac{14.5}{1.00258} 10^{-(2.27+5.65 \times 10^{-3} T_F - 8.06 \times 10^{-6} T_F^2 + 0.075 I)} \quad (22)$$

$$K_{\text{hyd}} = 2.58 \times 10^{-3} \quad (23)$$

$$K_{\text{ca}} = 387.6 \times 10^{-(6.341 - 1.594 \times 10^{-3} T_F + 3.52 \times 10^{-6} T_F^2 - 3.07 \times 10^{-5} p - 0.4772 I^{0.5} + 0.11807 I)} \quad (24)$$

$$K_{\text{bi}} = 10^{-(10.61 - 4.97 \times 10^{-3} T_F + 1.331 \times 10^{-5} T_F^2 - 2.624 \times 10^{-5} p - 1.66 I^{0.5} + 3.4661 I)} \quad (25)$$

$$K_{\text{H}_2\text{S}} = 10^{-634.27 + 0.2709 T_K - 1.1132 \times 10^{-4} T_K^2 - 16719 \times T_K^{-1} - 261.9 \log_{10} T_K} \quad (26)$$

$$K_{\text{HS}} = 10^{782.43945 + 0.036126 T_K - 1.6722 \times 10^{-4} T_K^2 - 20565.7315 T_K^{-1} - 142.7417222 \ln T_K} \quad (27)$$

$$K_{\text{bs}} = 10^{-23.93 + 0.030446 T_K - 2.4831 \times 10^{-5} T_K^2} \quad (28)$$

$$K_{\text{wa}} = 10^{-(29.3868 - 0.0737549 T_K + 7.47881 \times 10^{-5} T_K^2)} \quad (29)$$

where:

T_F = Temperature (°F)

T_K = Temperature (K)

p = partial pressure of CO₂ (bar)

I = Ionic strength (molar)

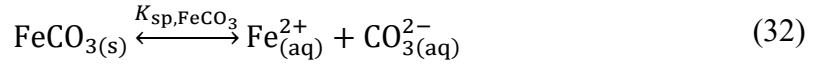
The ionic strength is calculated with Equation 30 where c_i , z_i , and N are the concentration (molar) of species i , the charge of species i , and the total number of species, respectively. Equilibrium is reached when electroneutrality is achieved (Equation 31) [10].

$$I = \frac{1}{2} \sum_{i=1}^N c_i z_i^2 \quad (30)$$

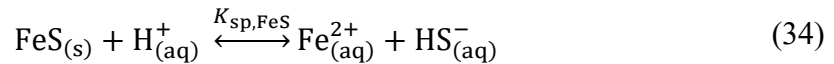
$$\sum_{i=1}^N c_i z_i = 0 \quad (31)$$

2.2.2 Formation of Corrosion Product Layers

If saturation is reached, both iron carbonate and iron sulfide can precipitate. The precipitation reactions for iron carbonate and iron sulfide along with their attributed solubility product expressions are given in Equations 32-35 [8, 9].



$$K_{\text{sp,FeCO}_3} = C_{\text{Fe}^{2+}} C_{\text{CO}_3^{2-}} \quad (33)$$



$$K_{\text{sp,FeS}} = \frac{C_{\text{Fe}^{2+}} C_{\text{HS}^-}}{C_{\text{H}^+}} \quad (35)$$

Considering temperature and ionic strength, the solubility products $K_{\text{sp,FeCO}_3}$ and $K_{\text{sp,FeS}}$ are calculated with empirical correlations, which are given in Equations 34 and 35, respectively [16], [17].

$$K_{\text{sp,FeCO}_3} = 10^{-\left(59.3498 - 0.041377T_K - \frac{2.1963}{T_K} + 24.5724 \log_{10} T_K + 2.518\sqrt{I} - 0.657I\right)} \quad (36)$$

$$K_{sp,FeS} = 10^{\frac{2848.779}{T_K} - 6.347} K_{HS} K_{bs} \quad (37)$$

The solubility products indicate whether precipitation is thermodynamically possible but do not give any indication on how fast precipitation can occur. Precipitation kinetics is dependent upon solution supersaturation, temperature, and the onset of nucleation. If the saturation with respect to a precipitate is greater than 1 then precipitation may occur. The saturation (S) and precipitation (R) rates of iron carbonate and iron sulfide are given by Equations 38-41 [18], [19].

$$S_{FeCO_3} = \frac{C_{Fe^{2+}} C_{CO_3^{2-}}}{K_{sp,FeCO_3}} \quad (38)$$

$$R_{FeCO_3} = e^{28.20 - \frac{64.85}{RT_K}} \left(\frac{S}{V}\right) K_{sp,FeCO_3} (S_{FeCO_3} - 1) \quad (39)$$

$$S_{FeS} = \frac{C_{Fe^{2+}} C_{HS^-}}{K_{sp,FeS} C_{H^+}} \quad (40)$$

$$R_{FeS} = e^{48 - \frac{40,000}{RT_K}} \left(\frac{S}{V}\right) K_{sp,FeS} (S_{FeS} - 1) \quad (41)$$

where:

S_{FeCO_3} = Saturation of iron carbonate

R_{FeCO_3} = Rate of iron carbonate formation (mol/m²/s)

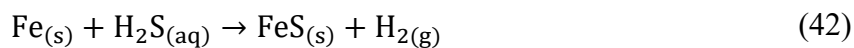
S/V = Surface to volume ratio

R = Gas constant (J/mol/K)

S_{FeS} = Saturation of iron sulfide

R_{FeS} = Rate of iron sulfide formation (mol/m²/s)

While iron carbonate is considered to be solely produced through precipitation, the FeS polymorph mackinawite has been postulated to form through both precipitation and a direct reaction with iron as given by Reaction 42 [20], [21].



Mackinawite, FeS, is typically the first iron sulfide formed in the corrosion of steel in H₂S-containing environments. The formation of mackinawite through a direct reaction with iron has been justified by Sun and Nescic [20] due to the fast formation kinetics, minimal effect of the bulk supersaturation on mackinawite formation, and the similarities between the crystal structures of ferrite and mackinawite [22].

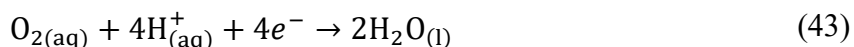
Two layers are typically observed in iron sulfide corrosion product layers: a thin, inner layer and a porous, outer layer. Sun and Nescic [20] proposed a mechanism whereby the thin, inner layer is formed by a reaction of H₂S to iron. The outer layer is then formed by the spallation of this thin inner layer due to internal compressive stresses that arise in the inner mackinawite layer. The mechanism of mackinawite formation was later reexamined by Zheng, *et al.*, [21] who postulated that the inner layer forms through chemisorption and the outer layer is formed by precipitation. The thin inner layer can act as a preferred nucleation site for the growth of FeS.

2.2.3 Effect of O₂ on CO₂ and H₂S Corrosion

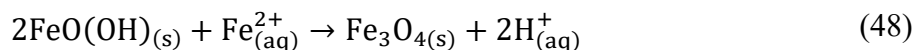
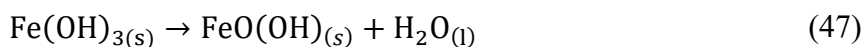
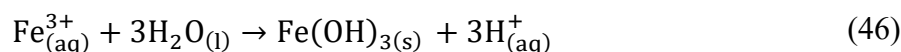
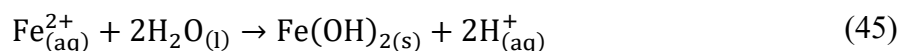
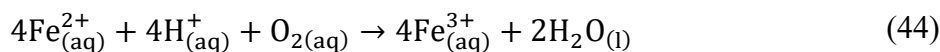
Ingress of oxygen, even at low concentrations, can significantly affect corrosion processes. The presence of oxygen in pipelines is attributed to ingress at low pressure points or dissolved in additives such as methanol [23]. A survey of 44 North American

natural gas transmission companies found that maximum allowable O₂ concentrations were between 0.01 and 0.10 mol% with a typical value of 0.02 mol% [24].

If oxygen is present in acidic environments such as those associated with CO₂ and H₂S then the reduction of oxygen (Reaction 43) may occur [25] given the presence of a species that can give up electrons (e.g., a corroding metal).



The formation of iron oxides and iron oxyhydroxides proceeds through the following reactions:



where FeO(OH) can be in the α , β , or γ form depending on the formation conditions [26].

2.2.4 Crystal Structures of Corrosion Product Species

Corrosion products that form in sales gas conditions may include iron carbonate, iron sulfide, iron oxide, and iron oxyhydroxide. The phases formed as a product of corrosion will ultimately depend on both thermodynamics and kinetics, which are, in turn, determined by pipeline conditions including CO₂ partial pressure, O₂ partial pressure, H₂S partial pressure, and temperature. The names, formulae, unit cell types, and the characteristic/related crystal structure of inorganic phases commonly found in corrosion products formed due to the internal corrosion of pipeline steel are given in Table 3.

Table 3: Common phases found in corrosion products formed in CO₂, H₂S, and O₂ corrosion

Phase	Formula	Crystal Structure	Source
Iron Carbonate			
Siderite	FeCO ₃	Trigonal; Calcite	[27]
Iron Sulfide			
Mackinawite	FeS	Tetragonal; 2D Layer; anti-Lead Oxide	[28]
Greigite	Fe ₃ S ₄	Cubic; Spinel	[29]
Pyrite	FeS ₂	Cubic; Rock Salt	[29]
Pyrrhotite	Fe _{1-x} S (x = 0 to 0.17)	Monoclinic, Hexagonal; Nickel Arsenide	[29]
Troilite	FeS	Hexagonal; Nickel Arsenide	[29]
Cubic FeS	FeS	Cubic; Zinc Blende	[29]
Iron Oxide			
Hematite	α -Fe ₂ O ₃	Hexagonal; Corundum	[26]
Magnetite	Fe ₃ O ₄	Cubic; Spinel	[26]
Wüstite	FeO	Cubic; Rock Salt	[26]
Maghemite	γ -Fe ₂ O ₃	Cubic; Spinel (Fe – deficient)	[26]
Iron Oxyhydroxide			
Goethite	α -FeO(OH)	Orthorhombic; Diaspore	[26]
Akagenite	β -FeO(OH)	Monoclinic; Nickel Arsenide	[26]
Lepidocrocite	γ -FeO(OH)	Orthorhombic; Boehmite 2D layer	[26]

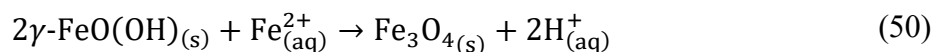
2.3 Black Powder

Sherik, *et al.*, [8] collected black powder samples from Saudi Aramco sour gas and sales gas pipelines for analysis by X-ray diffraction (XRD) and X-ray fluorescence (XRF). The sour gas pipeline black powder samples were predominantly composed of FeS and

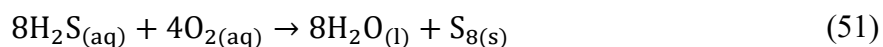
FeS₂ with minor amounts of Fe₃O₄, FeO(OH), and FeCO₃. XRD of black powder samples from the sales gas pipelines detected Fe₃O₄, α-FeO(OH), and γ-FeO(OH) with small amounts of FeCO₃. However, sulfur was detected in all collected samples by XRF, which suggests the black powder may contain an amorphous sulfur-containing species. Elemental sulfur was detected with XRD in some samples, but it is unclear if it was detected in the sour gas black powder or the sales gas black powder.

Yamada, *et al.*, [30] examined the composition of black powder produced in a Japanese sales gas network. The black powder was determined to be predominantly magnetite, but small amounts of hematite, goethite, lepidocrocite, and siderite were also found. Iron sulfide and elemental sulfur was detected in trace amounts in pipelines that historically transported H₂S-containing sales gas. Both mill scale and the corrosion of pipeline steel due to oxygen and water vapor ingress is attributed to be a major source of black powder due to the high quantity of magnetite collected. Ingress of O₂ and H₂O during pipeline construction and maintenance is suggested to be the primary cause of corrosion.

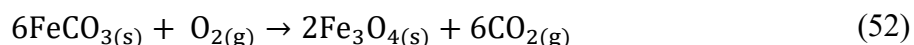
The identification of iron oxide and iron oxyhydroxides as the major components of black powder in sales gas pipelines containing O₂ and liquid water were used by Sherik, *et al.*, and Yamada, *et al.*, to justify the corrosion of steel due to oxygen as the primary source of black powder. However, the presence of lepidocrocite and elemental sulfur suggests the formation of iron oxide and iron oxyhydroxide from an iron sulfide precursor likely occurred. The formation of lepidocrocite in sales gas conditions is largely attributed to the oxidation of mackinawite, which is shown in Reaction 49 [31], [32]. Magnetite can then form through the reaction of lepidocrocite and ferrous ions (Reaction 50) [33].



The oxidation of iron sulfide is not the only pathway to elemental sulfur. Elemental sulfur may be obtained through the oxidation of H_2S as shown in Reaction 51.



The oxidation of iron carbonate may also occur and is reported to follow Reaction 52.



2.4 Water Availability

Measured dew points of water in the sales gas network were reported by Sherik, *et al.*, [8] and are given in Figure 2. The sales gas moisture content consistently exceeded the maximum moisture level of 7 lbs/MMscf (0.112 mg/L) set by sales gas specifications. The dew point temperature of water was generally lower than 10°C, but several dew points exceeded 15°C, which may lead to water condensation depending on the pipeline steel temperature.

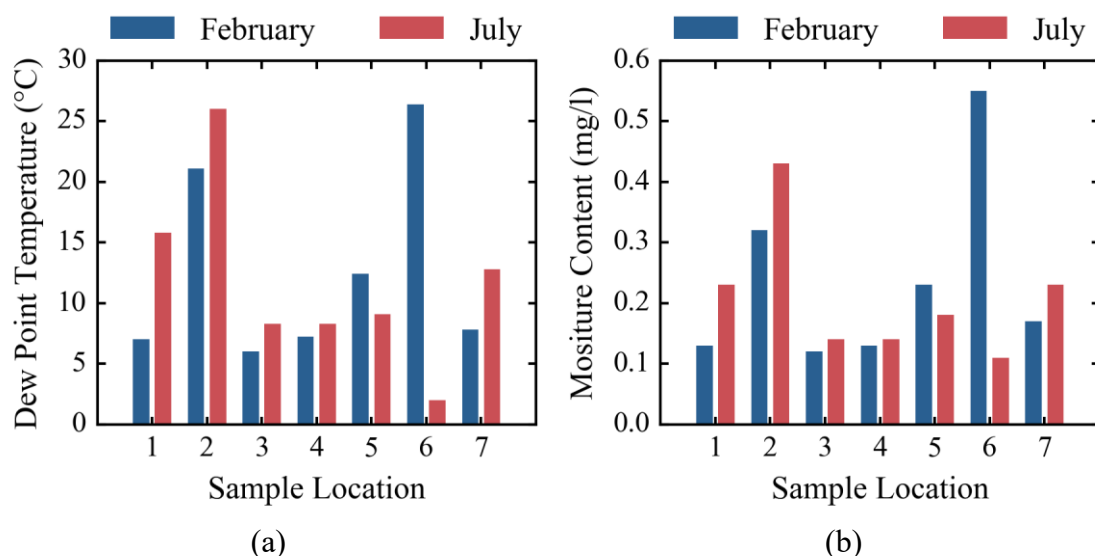


Figure 2: (a) Measured dew point temperatures and (b) corresponding moisture contents of sales gas measured during July and February at sampling locations in the Saudi Aramco sales gas network [8].

Sherik compared the measured water dew points to meteorological data to examine the potential for water condensation on the steel pipeline. As indicated by Figure 3, winter ambient temperatures in Saudi Arabia were often below the water dew point temperatures measured; therefore, water condensation was likely. If the ambient temperature serves as an adequate proxy for the steel temperature, then water condensation is likely to be cyclical where water condensation can be expected to occur during cool time periods, such as overnight, and not occur during warm time periods such as during the day. Cyclical water wetting may affect the corrosion product layer morphology due to fast precipitation during drying. The effect of temperature fluctuations on the corrosion product morphology is

unknown, but corrosion in dewing conditions has been studied in top-of-the-line corrosion studies.

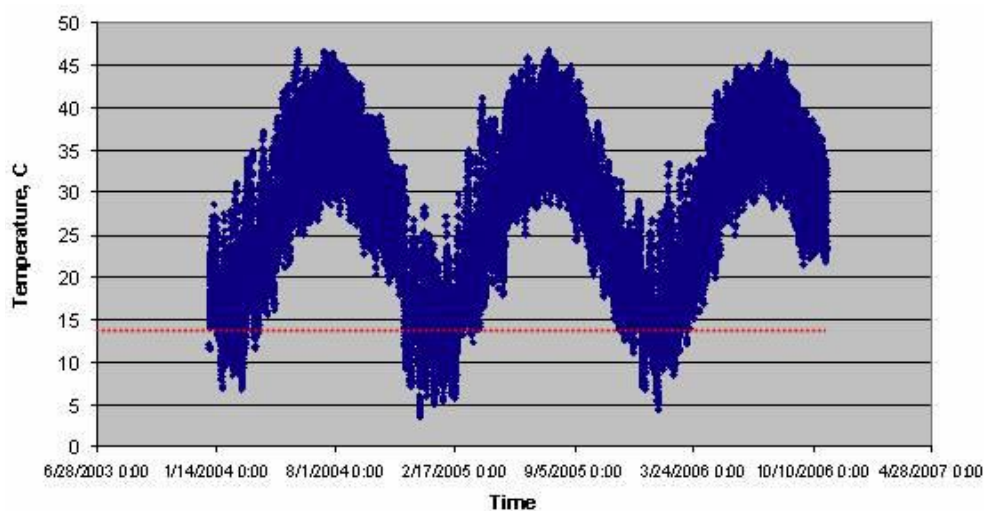


Figure 3: Ambient temperatures in the Eastern Province of Saudi Arabia. Points below the red dotted line indicate times when dew may form in the pipeline. Reproduced with permission from NACE International, Houston, TX. All rights reserved. A.M. Sherik, S.R. Zaidi, E.V. Tuzan, J.P. Perez, Paper 08415 presented at CORROSION/2008, New Orleans, LA. © NACE International 2008 [8].

2.4.1 Top-of-the-Line Corrosion

Prior to processing, natural gas contains condensable species including water, hydrocarbons, and organic acids. If the gas is saturated with water and the steel temperature is cooler than the gas temperature, then the water can condense on the steel and cause corrosion. Corrosion in these conditions can be severe near the top of the pipeline where

nonvolatile corrosion inhibitors cannot reach, therefore, this type of corrosion has been called top-of-the-line corrosion (TLC) [34].

Water condensation plays a critical role in TLC. A high water condensation rate (WCR) would limit the ability of a corrosion product to precipitate due to dilution and thus leave the steel unprotected. Conversely, a low WCR would allow for higher ferrous ion concentrations and faster precipitation rates, potentially generating a protective corrosion product layer [35]. A model for determining the WCR based on heat transfer was developed by Zhang, *et al.* [36].

Studies have been performed that investigated the formation of corrosion products in TLC conditions since corrosion products can offer some protection against corrosion. Yaakob, *et al.*, examined the effect of iron sulfide on localized corrosion in marginally sour conditions similar to sales gas conditions without O₂. Steel specimens mounted in the lid of a glass cell with the polished side facing down were exposed to water-saturated CO₂/H₂S mixtures with H₂S partial pressures of 0, 0.015, 0.03, 0.08, and 0.15 mbar. To force water condensation on the specimens, their surfaces were cooled to below the 40 or 60°C gas temperature. Severe localized corrosion was found at 0.015 and 0.03 mbar H₂S and was attributed to failures within the FeS corrosion product layer. The corrosion product layers obtained at 0.08 and 0.15 mbar H₂S were more protective as no localized attack was observed, but the FeS layers were flaky and appeared to readily detach from the steel surface. Figure 4 shows the corrosion product morphology from the 40°C T_{gas}, 0.15 mbar H₂S partial pressure experiment. Corrosion product spallation appears to have occurred during either test exposure or the isopropanol rinse after specimen extraction, as evidenced

by the visibility of the inner FeS layer seen in the right half of Figure 4 [37]. The role of H₂S on the development of a corrosion product layer susceptible to spallation is still unknown.

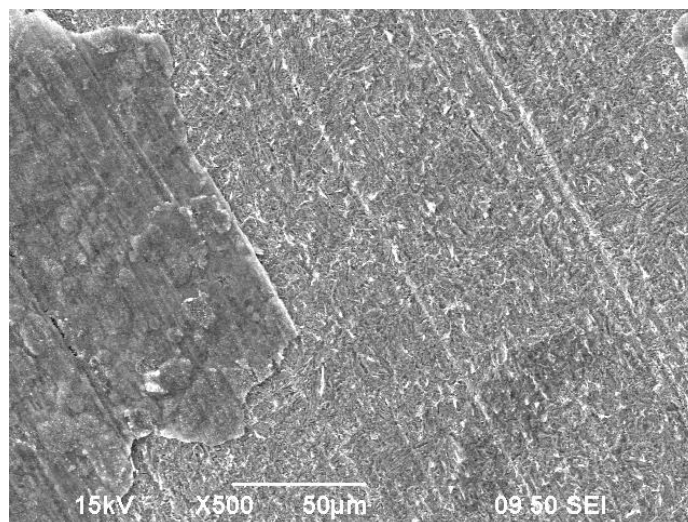


Figure 4: Flaky FeS corrosion product produced in marginally sour TLC conditions. (Test Conditions: Duration: 7 days, p_{H₂S}: 0.15 H₂S, p_{CO₂}: 0.93 bar, Water Condensation Rate: 0.25±0.04 ml/m²/s, T_{gas}: 40°C, T_{steel}: 25°C). Reproduced with permission from NACE International, Houston, TX. All rights reserved. N. Yaakob, F. Farelas, M. Singer, S. Nesic, D. Young, Paper 7695 presented at CORROSION/2016, Vancouver, BC. ©

NACE International 2016 [37]

2.4.2 *Hygroscopic Uptake of Water by Salts*

During the commissioning phase, a pipeline undergoes hydrotesting by flooding with water and subsequent pressurization to check for leaks. Due to volume requirements and water costs, a pipeline operator may elect to use seawater, which can leave a

hygroscopic salt residue on the pipe wall after the seawater is drained. If not properly rinsed, the salt residue can accumulate water from a humid sales gas stream.

The amount of moisture extracted from the surrounding atmosphere by a hygroscopic material is dependent primarily on its affinity toward water, relative humidity (RH), and temperature. Soluble materials with a high affinity toward water can dissolve if the availability of water is sufficiently high through a process called deliquescence. The RH whereby a material deliquesces is known as the deliquescence relative humidity (DRH). Efflorescence is the reverse process of deliquescence, where an electrolyte crystallizes due to drying. The DRH and the efflorescence relative humidity (ERH) are not necessarily the same as hysteresis between the DRH and the ERH exists due to crystallization kinetics [38]. Hygroscopic uptake of water by chloride and perchlorate salts in Martian soil has been hypothesized to be the reason for recurring slope lineae, dark streaks on Martian slopes only present during warmer seasons [39]. The potential for corrosion due to hygroscopic salts is examined below.

2.4.3 *Hygroscopic Corrosion*

Hygroscopic salts and their potential to lead to corrosion have been examined in atmospheric corrosion studies where the deposition of salt aerosols on metals can lead to corrosion in oxic conditions. The corrosive effect of hygroscopic NaCl particles on mild steel in atmospheric environments was investigated by Schindelholz, *et al.* [40]. NaCl was deposited onto mild steel specimens and subjected to air with relative humidities ranging from 1.5% to 90% RH for up to 300 days, demonstrating that water adsorbed on the NaCl particles and the steel can initiate corrosion at relative humidities as low as 33%. The

initiation of corrosion was attributed to water adsorbed to the NaCl crystals and the steel surface with capillary condensation, which accumulates water at the salt/steel interface.

The effect of CO₂ and H₂S on hygroscopic corrosion is even less understood.

Kolts [41] investigated the corrosion of sales gas pipelines due to salt deposits left behind by a seawater hydrotest. Steel samples with and without dried synthetic seawater deposits were exposed to RH-controlled CO₂. Kolts found salts can induce corrosion in the conditions tested but oxygen ingress is suspected to occur which will skew results.

Litke, *et al.*, [42] investigated the corrosion of steel under hygroscopic salts in CO₂/H₂S environments with humidity-controlled autoclaves. In their study, they placed salt dried under vacuum onto UNS G10180 steel coupons and then inserted the specimens into autoclaves with CO₂ and H₂S. The humidity of the autoclaves was controlled with methanol/water or ethylene glycol/water mixtures placed in the bottom of the autoclave before loading the samples. Figure 5 and Figure 6 show optical images of the exposed surface after extraction from a 14 day exposure to a gas with 15 psig H₂S and 57 psig CO₂. General and localized corrosion rates for the NaCl and MgCl₂ deposit tests were measured and are shown in Figure 5 and Figure 6, respectively. Both corrosion and corrosion product formation were found to occur in the conditions tested, however, reservations exist due to the measurement of similar general corrosion rates in the NaCl experiments at 86% and 0.7% RH and the appearance of corrosion product at 0.7% RH in the NaCl experiments. The surface of the NaCl/0.7% RH specimen is expected to look more like the surface of the MgCl₂/0.7% RH specimen with the white crystalline salt still on the surface. Corrosion underneath the NaCl crystals at 0.7% RH should be negligible due to the minute amount

of water in the vapor phase. The unexpected behavior is likely due to the ethylene glycol added for RH control.

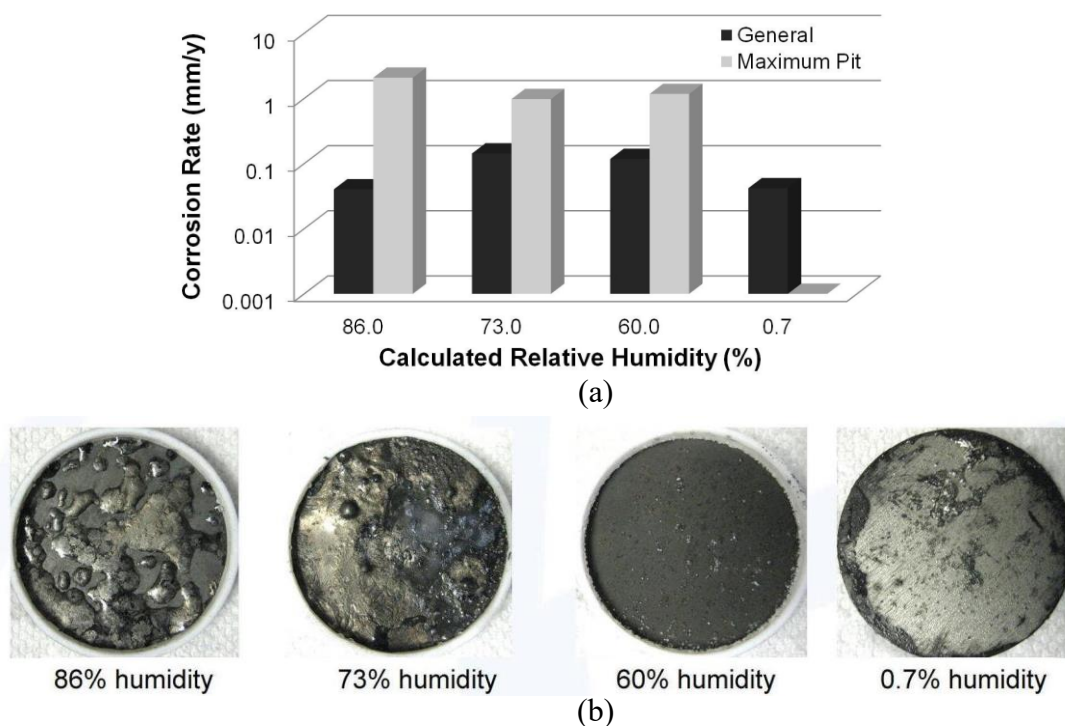


Figure 5: (a) Corrosion rates and (b) optical images taken after extraction of specimens with NaCl deposits exposed to $\text{CO}_2/\text{H}_2\text{S}$ gas mixtures with the indicated relative humidity. Reproduced with permission from NACE International, Houston, TX. All rights reserved. W. Litke, J. Bojes, P. Blais, J. Lerbscher, W. Wamburi, Paper 2339 presented at CORROSION/2013, Orlando, FL. © NACE International 2013. [42]

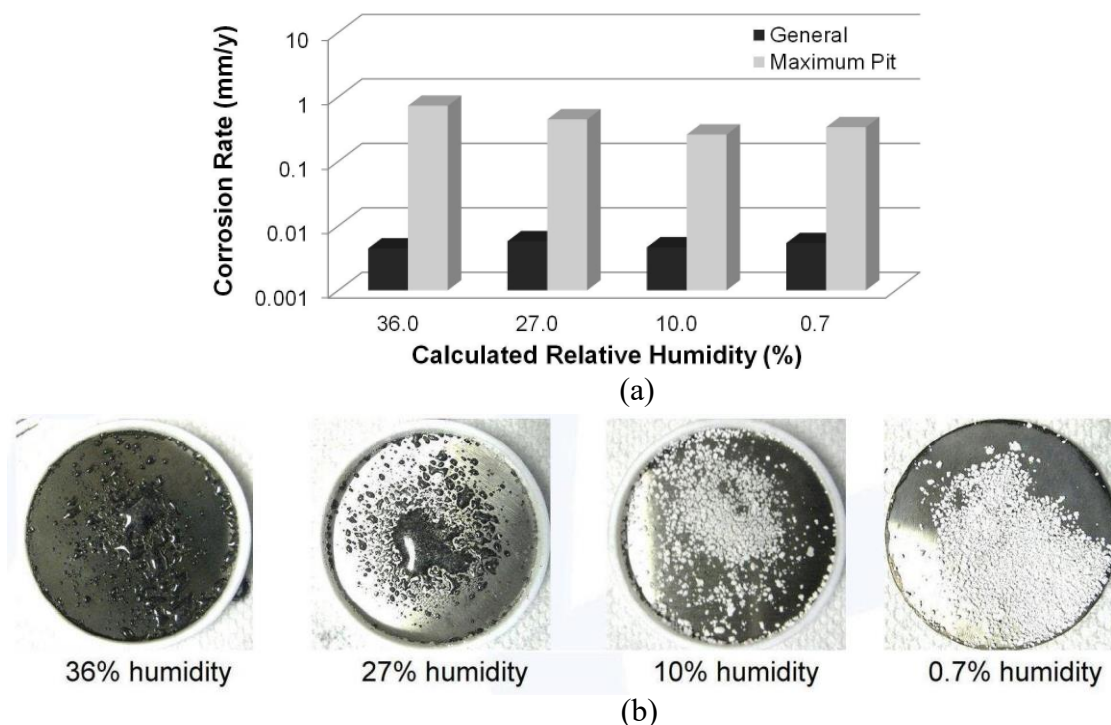


Figure 6: (a) Corrosion rates and (b) optical images taken after extraction of specimens with $MgCl_2$ deposits exposed to CO_2/H_2S gas mixtures with the indicated relative humidity Reproduced with permission from NACE International, Houston, TX. All rights reserved. W. Litke, J. Bojes, P. Blais, J. Lerbscher, W. Wamburi, Paper 2339 presented at CORROSION/2013, Orlando, FL. © NACE International 2013. [42]

Both Kolts and Litke, *et al.*, found corrosion to occur due to salt deposits in humid conditions related to gas production, but it is still unknown if corrosion induced by hygroscopic salts can contribute to black powder production as neither Kolts nor Litke examined the morphology or compositions of the corrosion products formed.

2.5 Gaps in Understanding Black Powder Formation

The literature on black powder formation is missing a vital step: spallation. A corrosion product can grow in a pipeline, but if that corrosion product cannot spall then it cannot become entrained in the gas and thus form black powder. However, to understand how corrosion product spallation leads to black powder, the processes that lead to corrosion product formation in sales gas conditions must be better understood.

Water availability has been identified as the primary unknown for corrosion in sales gas conditions since the concentrations of CO_2 , H_2S , and sometimes O_2 are known to be adequate for significant corrosion to occur. If the water content of the sales gas is high, then water may condense onto the steel surface. However, if the water content is below the thermodynamic dew point temperature, then a hygroscopic material like salt must be present for corrosion to occur. Cyclical temperature fluctuations were also identified as potentially changing the corrosion product morphology. Spalled corrosion products were obtained in dewing conditions with H_2S , but the effect of acid gas concentration and water condensation rates on the production of friable corrosion products is still unknown. While some information on corrosion product formation in dewing conditions is available, little is known about the potential for hygroscopic corrosion in CO_2 and H_2S conditions to produce friable corrosion products.

CHAPTER 3: RESEARCH OBJECTIVES AND HYPOTHESES

3.1 Objective

The primary objective of this work is to examine the formation of corrosion products, associated with black powder when spalled, developed through dewing and hygroscopic processes. The overall goal is to gain a better understanding of the role of water availability and H₂S concentration on the corrosion of sales gas pipelines.

This study is broken into two parts. Firstly, corrosion under dewing conditions is examined where water is forcibly condensed by cooling steel specimens in simulated sales gas conditions. The objective is to examine the corrosion products produced in a worst-case scenario; the effect of cyclic water condensation on corrosion product formation is also examined. Secondly, hygroscopic corrosion is examined where the objective is to determine if salts on the surface of the steel may lead to black powder production in conditions where water would not be expected to condense.

3.2 Hypotheses

Based on the literature review, the following hypotheses were formulated:

1. Pipeline conditions define what thermodynamically stable corrosion products will form on the steel surface although kinetically favored compounds will also be encountered.
2. The formation of corrosion products follows a cyclical pattern that correlates with the wet/dry cycle caused by external temperature fluctuations.
3. The cyclic behavior of water condensation and evaporation in sales gas pipelines prevents corrosion from reaching steady-state resulting in the formation of a

kinetically favored, and potentially friable, corrosion product susceptible to spallation and entrainment in the bulk gas.

4. Corrosion products will form on the steel surface in non-water saturated sales gas pipelines if a hygroscopic material is present on the steel surface.

3.3 Motivation

The Abu Dhabi based natural gas company Gasco is reporting black powder formation in their sales gas pipelines. Filtration and pigging are currently employed to minimize the impact to downstream operations, but are costly. A joint research partnership between the Abu Dhabi Petroleum Institute and the Ohio University Institute for Corrosion and Multiphase Technology has been tasked with examining the role of corrosion products on black powder formation in the Gasco pipelines as well as to examine potential methods of black powder mitigation.

CHAPTER 4: METHODOLOGY AND EXPERIMENTAL DESIGN

4.1 Overview

Corrosion of steel in sales gas conditions was examined by exposing steel specimens to CO_2 , $\text{CO}_2/\text{H}_2\text{S}$, or CO_2/O_2 mixtures in dewing or hygroscopic conditions. Under dewing conditions, water condensation was forced by cooling the steel specimens to a temperature lower than the gas temperature in a water-saturated environment. In hygroscopic conditions, NaCl was deposited onto steel specimens that were then placed in a relative humidity-controlled environment that allows deliquescence of the deposited NaCl or maintains a solid salt layer on the steel. Upon specimen extraction, corrosion product morphology was examined with scanning electron microscopy, and corrosion product composition was obtained with energy dispersive X-ray spectroscopy, Raman spectroscopy, and X-ray diffraction. Localized corrosion was characterized by surface profilometry.

4.2 Test Conditions

Experimental conditions were designed to simulate a GASCO sales gas environment known to produce black powder. Pipeline conditions used to determine experimental parameters are shown in Table 4. Oxygen and water contents were not measured. The 40 inch (1 m) GASCO pipeline transported the gas at a flow rate of 550 MMscfd at an operating pressure of 40-42 bar and an operating temperature of 33-50°C. From the specified gas concentration and the highest operating pressure, the partial pressures of CO_2 and H_2S were calculated to be approximately 0.55 bar and 0.3 mbar, respectively.

The experimental gas composition was primarily based on the partial pressure of H₂S measured in the pipeline. The experimental H₂S partial pressures were 0, 0.1, 0.3, and 1.0 mbar to examine corrosion in simulated GASCO conditions, and the effect of increased and decreased H₂S contents. The H₂S was diluted with CO₂ for a CO₂ partial pressure of 0.96 to 0.98 bar. Corrosion at 0.1 – 1 mbar H₂S is known to be H₂S dominant, so dilution over the GASCO conditions should not affect results. Tests with O₂ were conducted at 10 mbar O₂, the O₂ partial pressure expected if the O₂ content was approximately 0.02 mol%.

Table 4: Sales gas composition from which experimental parameters are derived

Component	Units of Measurement	Content
Methane	mol %	93.60
Ethane	mol %	3.25
Propane	mol %	0.58
i-Butane	mol %	0.10
n-Butane	mol %	0.16
i-Pentane	mol %	0.03
n-Pentane	mol %	0.02
Hexane+ (C ₆ and higher)	mol %	0.01
Carbon Dioxide	mol %	1.31
Nitrogen	mol %	0.84
Hydrogen Sulfide	ppm	7
Carbonyl Sulfide	ppm	3
Mercaptans	ppm	5

The steel used for all experiments is API 5L X65 mild steel, a grade of steel typically used for gas transmission pipelines. The steel composition is listed in Table 5. The steel is a low carbon steel with a ferritic-pearlitic microstructure. The microstructure is shown in Figure 7, which was determined after etching with a 2% Nital solution (HNO₃

in $\text{CH}_3\text{CH}_2\text{OH}$). Cementite (Fe_3C) and ferrite are found in the white and dark regions, respectively.

Table 5: Composition of API 5L X65 steel used for testing (wt.%)

C	Al	As	Co	Cu	Mn	Mo	Nb	Ni	P
0.05	0.033	0.015	0.012	0.14	1.21	0.16	0.03	0.38	0.004
S	Sb	Si	Sn	Ti	V	Zn	Fe		
<0.001	0.035	0.25	0.012	0.01	0.04	0.004	Balance		

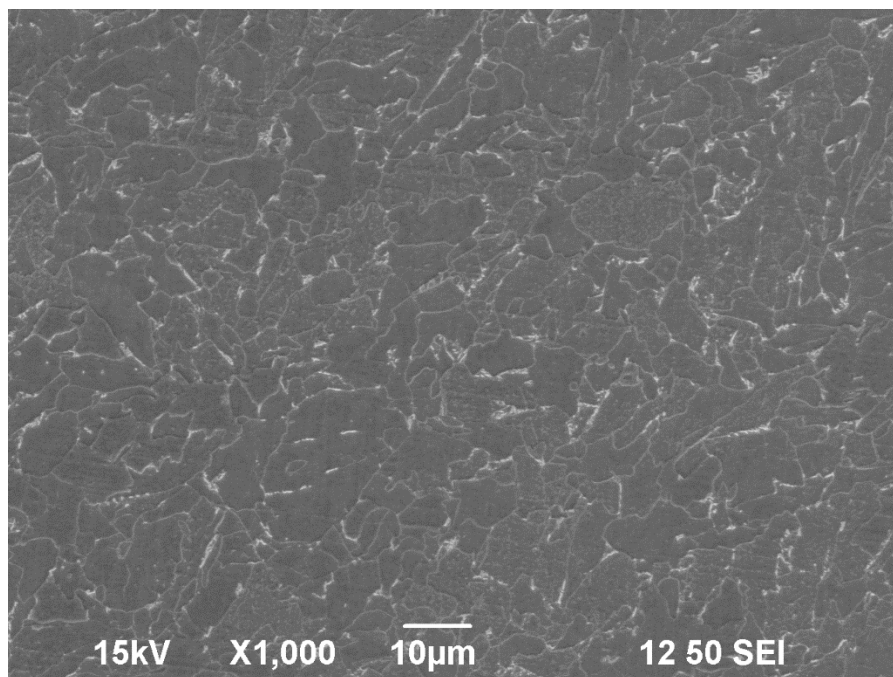


Figure 7: Microstructure of the X65 steel specimens. Ferrite and cementite are found in the dark and white locations, respectively.

4.3 Black Powder Formation in Dewing Conditions

Dewing conditions were examined by exposing specimens to water-saturated CO₂, CO₂/H₂S or CO₂/O₂ mixtures. Water condensation was stimulated onto the steel specimens by cooling their surfaces to 15°C or 25°C for high or low water condensation rates (WCR), respectively. The water-saturated gas was generated by bubbling CO₂/H₂S mixtures through deionized (DI) water heated at a temperature to maintain the gas temperature at 30°C. A 30°C gas temperature was selected by rounding down the 33°C GASCO sales gas operating temperature; the temperature most likely to condense water. The apparatus and procedures for testing in dewing conditions are based largely on those used by Yaakob, *et al.*, [37] to test marginally sour TLC conditions. Modifications, described below, were made to better control the steel temperature.

4.3.1 Dewing Corrosion Equipment

A glass cell setup, as shown in Figure 8, was used for testing black powder formation in water-condensing conditions. Gas, metered by a rotameter at the desired CO₂, H₂S, and O₂ concentrations, was bubbled through 1 liter of heated deionized (DI) water located in the bottom of the glass cell to heat and saturate the gas with water. The temperature of the water, which is controlled by the hotplate, is set such that the gas above the solution is held at the desired temperature of 30°C.

Two specimens were included in each test: a 1.25-inch-diameter × 0.5-inch-thick (31.7 mm × 12.7 mm) cylindrical specimen for surface and corrosion rate analysis, and a 0.5×0.5×0.08 inch³ (12.7×12.7×2 mm³) specimen for XRD compositional analyses. The cylindrical specimens were inserted directly into PEEK specimen holders designed to

provide a gas-tight seal to the lid while exposing a specimen surface for temperature control. The smaller XRD specimens were suspended from the lid with a specially designed holder, shown in Figure 10, where the steel specimens were held by a magnet within an aluminum body, which aids heat transfer to the Peltier thermoelectric cooler. The steel specimens were coated with Xylan on surfaces in contact with the holder to prevent galvanic effects. Additional design parameters can be found in Appendix A.

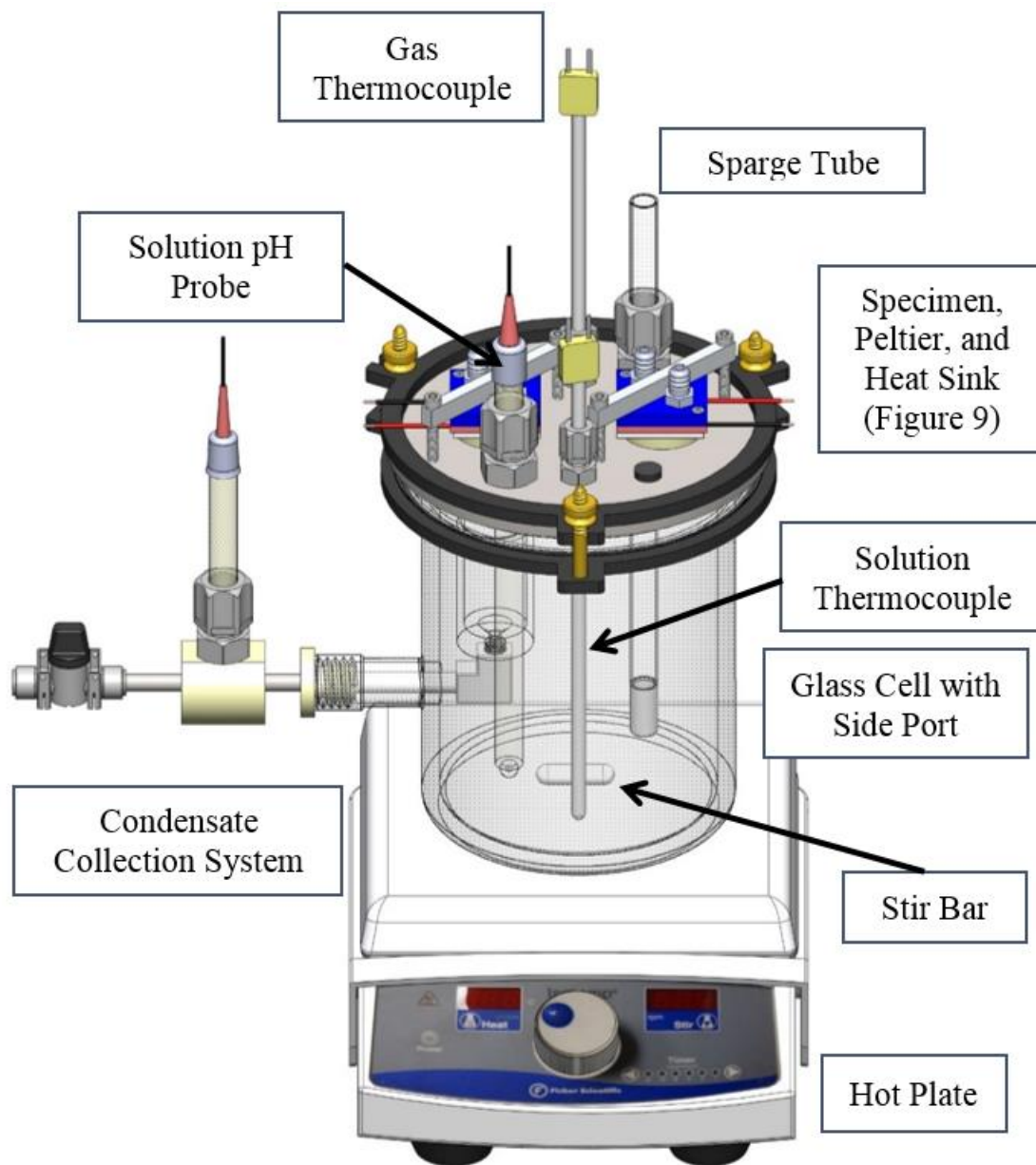


Figure 8: Dewing corrosion glass cell. Image courtesy of Cody Shafer.

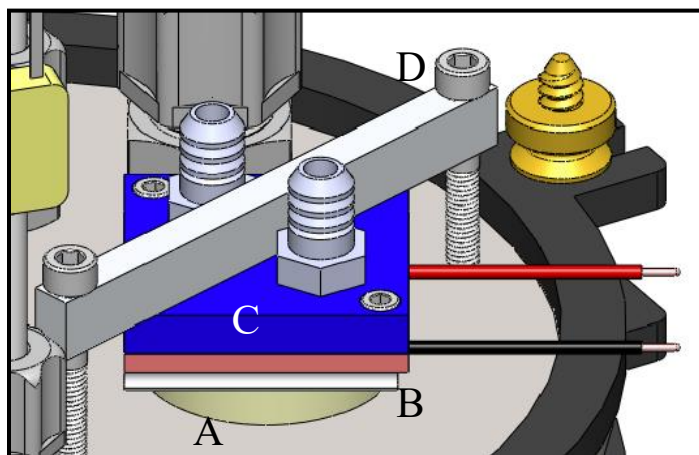


Figure 9: Specimen holding and control stack including (A) specimen holder, (B) Peltier, (C) Water cooled heat sink, and (D) Anchor bar and bolts. Image courtesy of Cody Shafer.

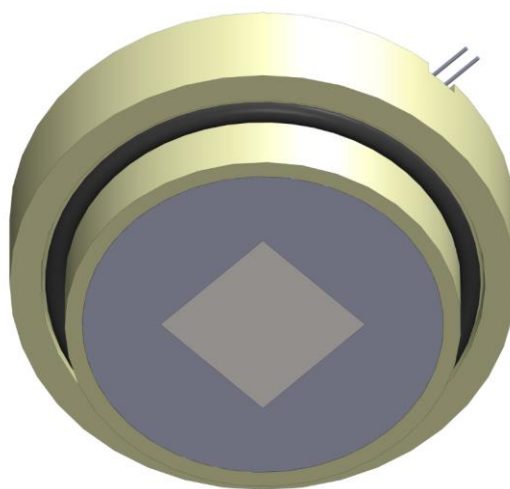


Figure 10: XRD specimen holder. Image courtesy of Cody Shafer.

Specimen temperature was controlled using a specially designed Peltier control system. The temperature is controlled by measuring the temperature with a thermistor mounted to the side of the cylindrical specimens or within the aluminum body of the XRD

specimen holder, computing the output with a PID (proportional-integral-derivative) feedback control loop, and supplying the computed power to a thermoelectric cooler in contact with the specimen. The thermoelectric cooler, more commonly known as a Peltier after the French physicist Jean Charles Athanase Peltier, acts as a heat pump when electrical power is applied. By controlling the amount of power supplied to the Peltier, the amount of heat transferred can be controlled. Power to the Peltiers is supplied by an external AC to DC power supply controlled with pulse width modulation. During operation, a significant amount of heat is generated, so a water-cooled heatsink is placed over the Peltier to prevent it from overheating. Temperature control was primarily done with a TC-48-20 Peltier controller by TE Technology®, but very similar results were obtained using a controller developed by the author of this thesis based on an Arduino® microcontroller.

To examine the effect of cyclic temperature fluctuations, the temperature of the steel specimen must be periodically changed. To control the temperature changes with a Peltier, the polarity of the Peltier must be switched. Changing the polarity of the Peltier changes the direction heat is pumped and, therefore, switches the hot and cold sides of the Peltier. The TC-48-20 Peltier controller cannot change the polarity internally, so a double-pole-double-throw mechanical relay was connected between the controller and the relay. MOSFETs in an H-bridge configuration were used to control both the power and the polarity in the Arduino controller. Additional information regarding the controllers can be found in Appendix A.

4.3.2 *Dewing Corrosion Experimental Procedures*

The glass cell shown in Figure 8 was cleaned then 1 liter of deionized water introduced. The glass cell was then placed on the hot plate and the DI water heated to 35°C to maintain the gas temperature at setpoint. The glass cell was purged with CO₂ for at least 3 hours by sparging the CO₂ through the DI water.

Prior to insertion, the specimens were coated with Xylan®, a fluoropolymer, to prevent the specimens from corroding on undesired surfaces. Following routine procedures, the specimens were then ground with silicon carbide abrasive papers to a 600 grit finish with water as the coolant. The water was rinsed from the surface with isopropanol immediately after grinding to prevent unwanted corrosion. The specimens were cleaned in isopropanol in an ultrasonic bath, dried with cool air, and then the initial mass was recorded. Specimens were stored in nitrogen until insertion, which was ordinarily less than an hour after polishing.

The specimens were inserted into the specially designed holders outlined above and mounted to the glass cell lid. The Peltiers and heatsinks were placed over the specimens, and the resultant stack fastened to the lid. The thermistors and Peltiers were connected to the controllers, and specimen temperature control was started. The glass cell was allowed to purge for an additional 30 minutes with CO₂ before H₂S was then added into the system. The H₂S concentration was set by mixing a CO₂ and a CO₂/H₂S stream metered by a rotameter upstream of the glass cell. The H₂S concentration was measured with colorimetric gas detector tubes (GASTEC 4HM) and adjusted as necessary. Gas was continuously purged through the glass cell throughout the experiments. Effluent gas

containing H₂S was passed through a sodium hydroxide solution and finally an activated carbon scrubber. Test conditions were monitored and adjusted as needed to maintain experimental parameters.

After the allotted exposure time, the specimens were removed and immediately rinsed with isopropanol to remove water and prevent unwanted oxidation. The rinse was performed by targeting the top of the specimen with a stream of isopropanol from a squirt bottle and allowing the isopropanol to fall over the rest of the specimen. The wall shear stress of the isopropanol rinse was calculated to be about 1 Pa, roughly the same wall shear stress in the GASCO pipeline. Whether or not corrosion product was found in the waste isopropanol was recorded. The specimens were dried under nitrogen, optical images were taken, and the specimen with corrosion product was weighed. The specimens were then stored in a desiccator under nitrogen awaiting further analysis.

4.4 Black Powder Formation in Hygroscopic Conditions

The effect of salts on the corrosion of steel in unsaturated conditions was examined by depositing salts onto steel specimens and exposing the specimens to relative humidity-controlled CO₂, CO₂/H₂S and CO₂/O₂ mixtures. The three relative humidities tested were 75%, 58%, and 33% controlled through the use of saturated aqueous solutions of NaCl, NaBr, and MgCl₂, respectively.

4.4.1 Hygroscopic Corrosion Equipment and Procedures

Hygroscopic corrosion tests were performed in a glass cell with the specimens located on a platform above the saturated salt solutions in the bottom of the glass cell, as shown in Figure 11. The apparatus consisted of a glass cell, TeflonTM lid, lid clamp, gas

inlet, gas outlet, specimen platform, and thermocouple. A large hole was made in the lid for fast specimen insertion and extraction. The large hole was sealed with a rubber stopper, which was clamped down, if necessary, to ensure a gas-tight seal.

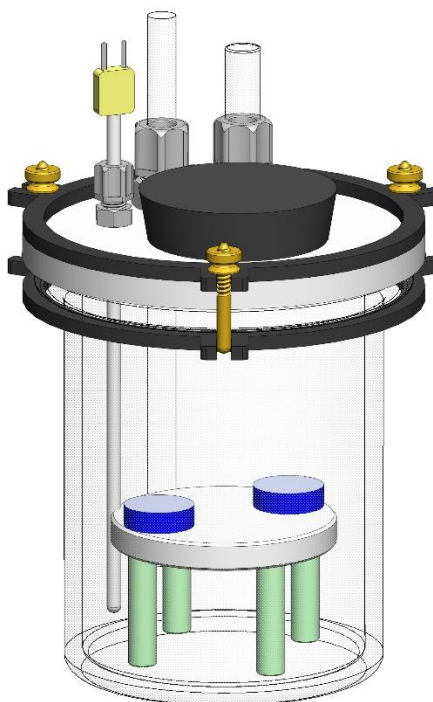


Figure 11: Hygroscopic corrosion glass cell. Image courtesy of Cody Shafer.

Prior to testing, the glass cell, lid and stage are thoroughly cleaned with DI water and isopropanol then dried. In the bottom of the glass cell, 100 ml of DI water was mixed with salt at 125% of the solubility limit in water at 25°C. The stage is then placed into the glass cell and the lid is fastened. The glass cell is purged with N₂ for a minimum of 4 hours to remove oxygen.

X65 steel specimens, the same geometry as those used in dewing conditions, were coated with Xylan on all surfaces where corrosion is undesired. The steel surface was ground with carbide abrasive paper and then polished to a mirror finish by polishing with a 0.25 μm diamond suspension. The specimens were then thoroughly rinsed with DI water and ultrasonically cleaned in isopropanol. Residual isopropanol was evaporated with cool air, and the specimen mass was recorded. The specimens were stored in N_2 until salt was deposited onto the surface or the clean specimen was inserted into the glass cell.

Salt layers were generated by drying a NaCl/DI water solution placed on the steel specimens with N_2 . A 3.5 wt.% NaCl solution was prepared prior to experimentation and used for all experiments; this is a similar salinity to seawater. The salt solution was purged with N_2 , and 250 μl of solution was deposited onto the steel surface with a pipette. The specimen was immediately placed in a N_2 environment, and the water was then spread over the entire surface by tilting the specimens. The salt solution was dried by passing dry N_2 over the wetted steel surface. Once the salt crystallized, the specimen mass with salt was measured, photographed, and then placed in the N_2 -purged glass cell on the platform salt-side up.

The glass cell was allowed to purge with N_2 for another 30 minutes before replacement with the test gas, which was continuously sparged into the system throughout each experiment. The dry test gas entered the glass cell through a tube with the outlet approximately 1 cm above the saturated salt solution. The gas was not bubbled through the salt solution to prevent aerosol formation, which can contaminate the steel surface; this phenomenon was observed in preliminary experiments with saturated MgCl_2 . A small gas

flow rate was maintained throughout the experiment to prevent a decrease in the gas RH. In sweet conditions, a hygrometer (GE Panametrics Moisture Monitor Series 35) was placed downstream of the glass cell to verify the relative humidity, but the hygrometer could not be used in H₂S testing due to chemical incompatibility. Specimen extraction was performed in the same manner as outlined in the dewing corrosion procedures.

4.5 Analytical Methods

Scanning electron microscopy (SEM) and optical microscopy were performed to examine the corrosion product morphology. SEM was performed with a JEOL JSM-6390LV. SEM sampling locations were selected to be representative of the specimen surface at large. Hygroscopic corrosion specimens were sputter-coated with palladium to minimize charging in the SEM. Cross-sectional SEM was performed after first mounting the specimen in epoxy to stabilize the corrosion product and cutting the specimen normal to the steel surface with a diamond-tipped saw blade. The cross-section was polished to a mirror finish through the use of consecutively finer grit silicon carbide abrasive paper and diamond suspensions. The cross-sectioned surface was sputter-coated with palladium to minimize charging.

Corrosion product/phase composition was determined locally with energy dispersive X-ray spectroscopy (EDS), Raman spectroscopy, and, more generally, by X-ray diffraction (XRD). EDS was performed with an EDAX Genesis attachment on the SEM. Raman spectroscopy was conducted with a Bruker Senterra with a 785 nm wavelength laser. XRD was performed on a Rigaku Ultima IV with a CuK α source over 10-70° 2 θ at a scan rate of 1° per minute. The corrosion product was removed in accordance with ASTM

G1-03 [43], and the corrosion rate and corrosion product mass was calculated by comparing the after removal mass to the initial mass and the after extraction mass, respectively. A detailed description of calculation methodologies can be found in Appendix B. Localized corrosion was examined by optical surface profilometry using an Alicona InfiniteFocus microscope.

4.6 Safety

The primary risk during the work conducted for this thesis is exposure to hydrogen sulfide through inhalation. H₂S atmospheres above 100 ppm are considered immediately dangerous to life and health. To protect against H₂S inhalation, experiments with H₂S concentrations above 0.1 mbar (100 ppm) H₂S were conducted in a segregated laboratory at the Ohio University Institute for Corrosion and Multiphase Technology, which has a safety system designed for H₂S experimentation.

The safety system contained multiple levels of defense. The first level is, of course, maintaining a well-sealed glass cell. If the gas inlet flow rate did not match the gas outlet flow rate, then H₂S was not added into the system. The second level was the vent hood in which the glass cell was placed. Any leakage of H₂S from the glass cell would be largely contained by the vent hood and sent to an activated carbon scrubber. Then, if necessary, the effluent gas is passed through a combustion system and released. The third level of defense was personal protective equipment (PPE). PPE worn included both an H₂S badge sensor and a self-contained breather apparatus (SCBA). The H₂S badge was worn during any entry into the H₂S room, regardless of whether or not experiments were being conducted. The badges have two audible and tactile alarms with the low alarm at 10 ppm

and a high alarm at 15 ppm. The badges were checked daily with a 25 ppm H₂S/air mixture to ensure they functioned properly. The SCBA was worn during any entry in the H₂S room while an H₂S experiment was conducted. Air was supplied to the SCBA wearer from cylinders located outside the H₂S room through hoses to prevent H₂S inhalation in the event of a release. Lastly, in case all previous safety layers failed, the buddy system was employed where trained personnel were stationed outside the H₂S room in visual contact with the person inside and ready to enter the laboratory at a moment's notice in the event of incapacitation. H₂S experiments below the 100 ppm H₂S threshold were conducted in a vent hood outside the H₂S laboratory. A badge was still worn when working in the vent hood in case of an accidental gas release.

The other primary safety concern is hydrochloric acid. Concentrated hydrochloric acid is a primary component of the solution, commonly known as Clarke solution, used to remove corrosion product. Any work with hydrochloric acid was done in a vent hood to minimize exposure to HCl fumes. Nitrile gloves were also worn to prevent skin contact.

CHAPTER 5: RESULTS AND DISCUSSION

5.1 Dewing Corrosion

If pipeline conditions are favorable, water may condense on the steel wall and allow CO₂, H₂S, and O₂ to corrode the steel and develop corrosion products, which may spall and develop black powder. Experiments were performed to investigate the formation of corrosion products in dewing sales gas conditions. The results of the experiments are reported and discussed below.

5.1.1 *Effect of H₂S Partial Pressure on Dewing Corrosion*

To examine the effect of H₂S on the corrosion of pipeline steel in water condensing conditions, experiments were conducted at varying H₂S partial pressures. H₂S partial pressures tested were 0, 0.1, 0.3, and 1 mbar with calculated water condensation rates (WCR) of 0.015 and 0.05 ml/m²/s. Experimental conditions are summarized in the test matrix shown in Table 6.

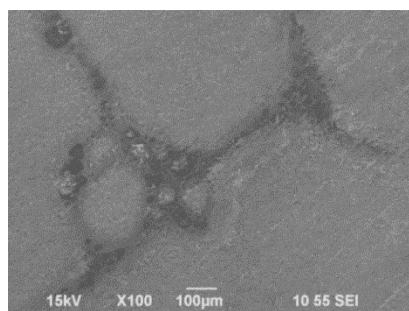
Table 6: Test matrix for studying the effect of H₂S partial pressure on dewing corrosion.

Parameter	Value
Test Material	API 5L X65
Total Pressure (bar)	1
H₂S Partial Pressure (mbar)	0, 0.1, 0.3, 1
O₂ Partial Pressure (mbar)	0
CO₂ Partial Pressure (bar)	0.96
N₂ + Ar Partial Pressure (bar)	0
Test Duration (days)	3
Water Condensation Rate (ml/m²/s)	0.015, 0.05
Steel Temperature (°C)	25, 15
Gas Temperature (°C)	30

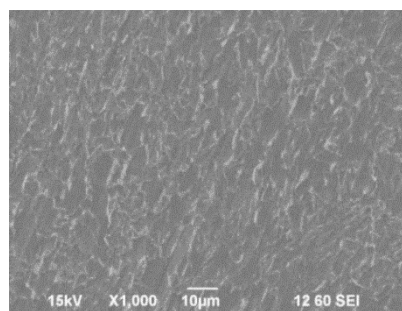
After extraction from the glass cell, the specimens were analyzed using SEM. Micrographs of the corrosion product on the steel surface after the extraction of specimens are shown in Figure 12. In CO₂ conditions, minimal corrosion product other than residual iron carbide was present. Some iron carbonate was present at the low WCR, whereas iron carbide was only present at the high WCR. At 0.1 mbar H₂S, a friable corrosion product was present at both WCRs, but buckling was present in regions presumed to be the edges of water droplets at the low WCR. At higher H₂S partial pressures, FeS spallation was much more pronounced. A higher degree of corrosion product layer buckling was observed at 0.3 mbar H₂S than at 0.1 mbar, but the buckles were confined to specific regions. Buckling was also present at the high WCR at 0.3 mbar H₂S. At 1.0 mbar H₂S, severe buckling was observed over the specimen surface at the low WCR. At the high WCR,

buckling still occurred, but was not nearly as severe. Buckle-driven spallation is examined further in a later section.

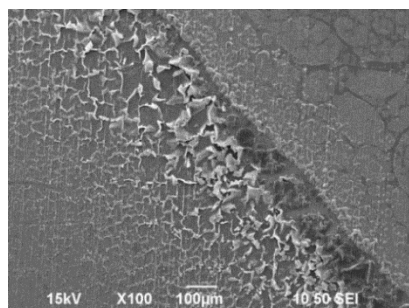
Diffraction patterns of specimens recovered from the H₂S experiments examining the effect of pH₂S are shown in Figure 13. At the low WCR, XRD did not pick up any corrosion product on the specimens analyzed from the CO₂ experiment, but mackinawite (FeS) was detected in tests with H₂S. Increasing the H₂S partial pressure saw an increase in mackinawite peak intensity, but the relative peak intensities did not match the mackinawite XRD reference data [28] indicating preferred orientation of the mackinawite layer on the steel substrate. This has been postulated to be due to a growth mechanism favoring parallel [100] and [001] iron and mackinawite planes, respectively, at the steel surface. At the high WCR, mackinawite was detected at 0.3 and 1.0 mbar H₂S, but not at 0.1 mbar.



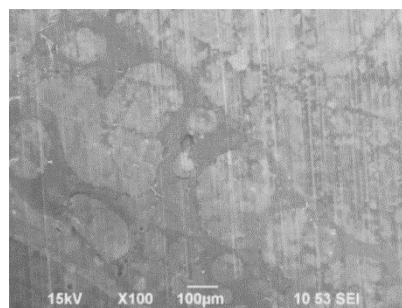
0 mbar – Low WCR



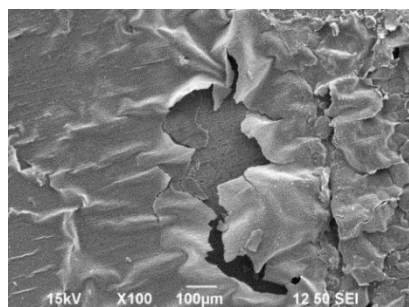
0 mbar – High WCR



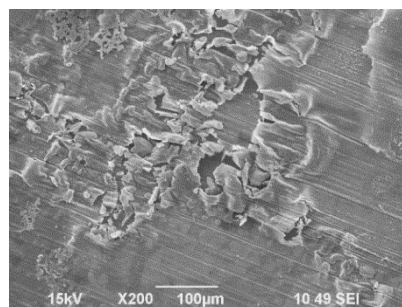
0.1 mbar – Low WCR



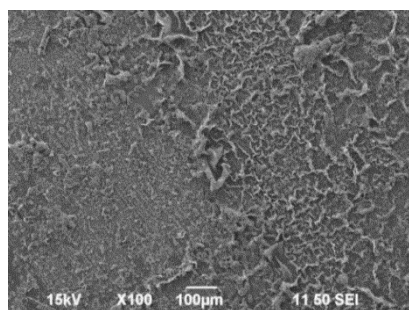
0.1 mbar – High WCR



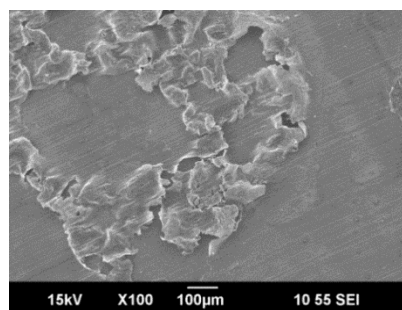
0.3 mbar – Low WCR



0.3 mbar – High WCR



1.0 mbar – Low WCR



1.0 mbar – High WCR

Figure 12: Effect of H_2S partial pressure and water condensation rate on corrosion product morphology.

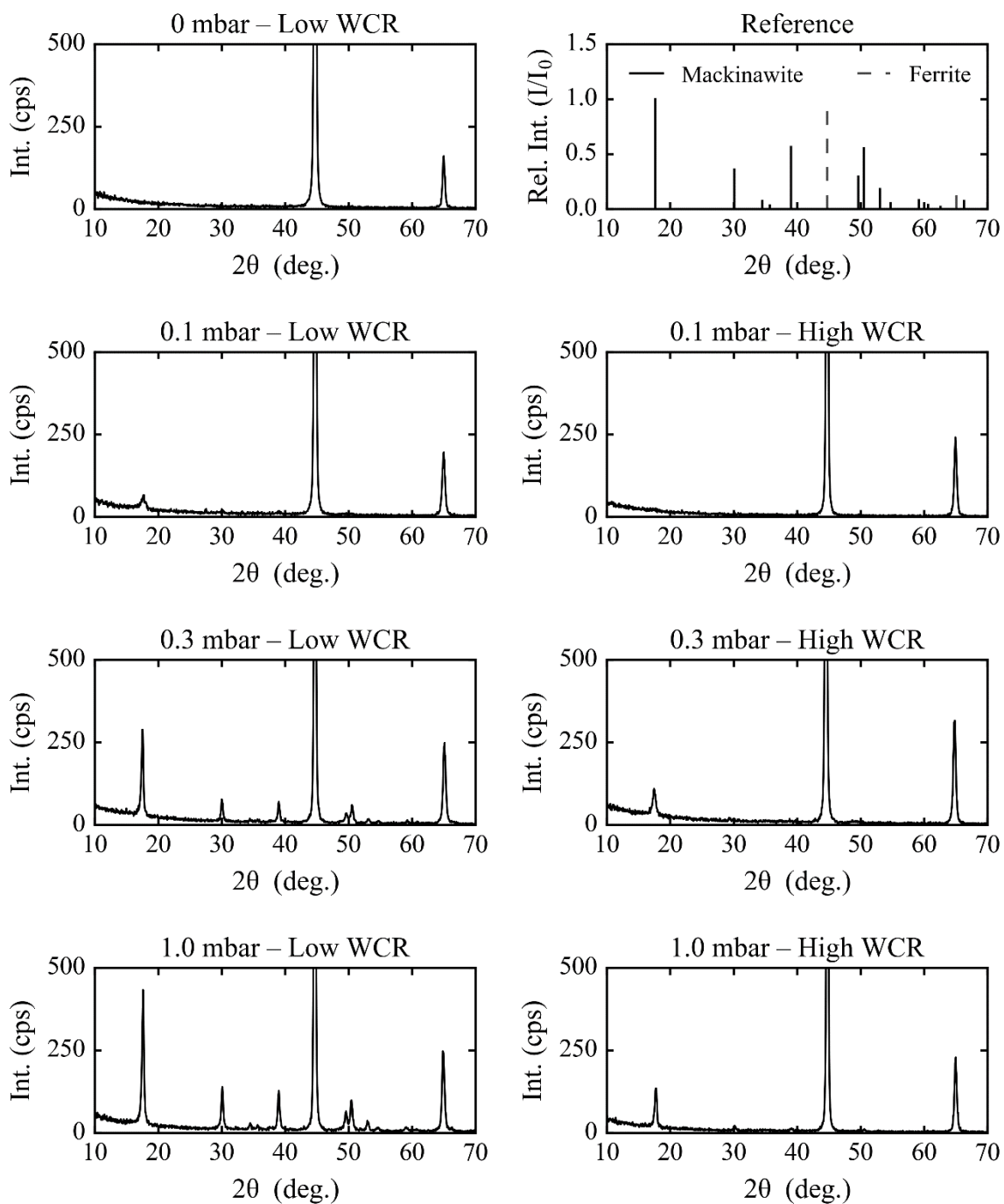


Figure 13: XRD data showing the effect of H_2S partial pressure and WCR on corrosion product composition

The effect of H₂S concentration on corrosion rate is shown in Figure 14. For both WCRs the addition of 0.1 and 0.3 mbar H₂S generally decreased the corrosion rate due to the corrosion product offering more protection. However, increasing the H₂S partial pressure to 1.0 mbar saw an uptick in the corrosion rate, particularly for the low WCR. The dramatic increase in corrosion rate at 1.0 mbar H₂S and low WCR is presumed to be due to the much higher degree of spallation observed at 1.0 mbar H₂S than at 0.3 and 0.1 mbar H₂S, since a spalling layer cannot offer as much protection to the steel as a more stable layer. The spallation of a corrosion product would expose the steel surface to further attack. The smaller uptick in corrosion rate observed in the 1.0 mbar and high WCR experiment relative to its low WCR counterpart is likely due to the lesser degree of corrosion product spallation.

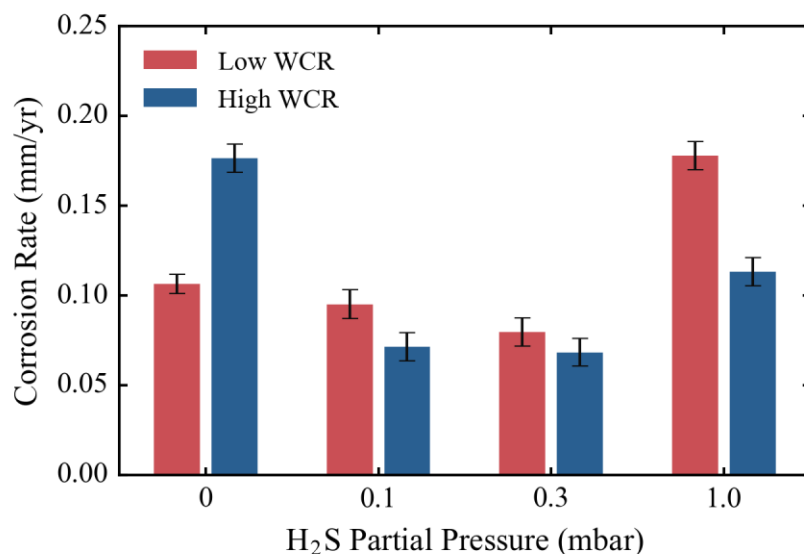


Figure 14: Effect of H₂S partial pressure and water condensation rate on corrosion rate.

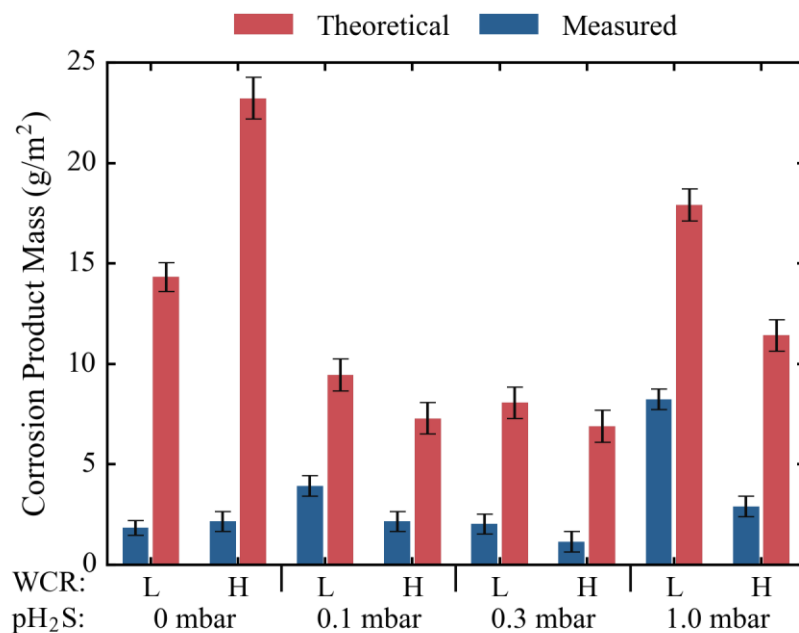


Figure 15: Effect of H₂S partial pressure and water condensation rate (L = low, H = high) on the measured and theoretical corrosion product masses.

The measured corrosion product mass and theoretical corrosion product mass are shown in Figure 15. The measured corrosion product mass is the mass of corrosion product removed with the inhibited hydrochloric acid (Clarke solution) in the procedure described by ASTM G1. The theoretical corrosion product mass is determined by calculating the maximum amount of corrosion product possible derived from iron lost due to corrosion. The theoretical corrosion product mass calculation assumes all iron lost due to corrosion, not in the form of Fe₃C, is converted to FeCO₃ under sweet conditions and FeS under sour conditions. Knowledge about the theoretical corrosion product mass is useful as a comparison against the measured corrosion product mass as it gives some insight into the amount of iron that was lost in removed condensed water or spalled corrosion product. As

evidenced by the large difference in the measured and theoretical corrosion product mass, most of the iron available for corrosion product formation on the steel surface was lost. The difference in the theoretical and measured corrosion product masses generally decreased with increasing H_2S concentration, but this is expected since corrosion product layers are easier to produce in sour systems than sweet systems at the temperatures tested.

The maximum black powder production rate shown in Figure 16 is calculated by extrapolating the theoretical corrosion product mass averaged by the experimental duration to a hypothetical 100 km length of a 42 inch (106.7 cm) ID pipeline. The maximum black powder production rates varied from 900 to 2000 kg/day for a 100 km, 42-inch ID pipeline. These numbers are high, but they represent a worst-case scenario where the entire hypothetical pipeline is experiencing water condensation.

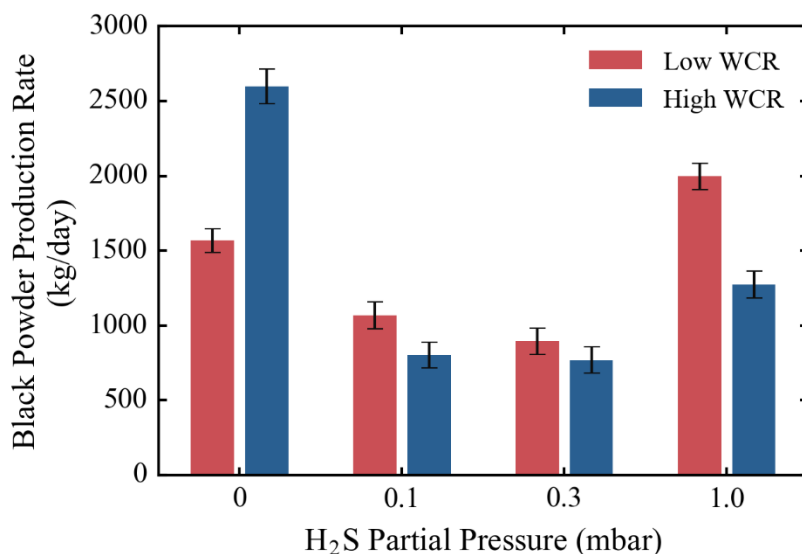


Figure 16: Effect of H_2S partial pressure on maximum possible black powder production rate in a 100 km, 42 inch ID pipeline.

5.1.2 Effect of Time on Sour Dewing Corrosion

The effect of time was examined by exposing steel specimens to 0.3 mbar H₂S and 0.96 bar CO₂ in an O₂-free environment for up to 10 days at the low WCR. Experimental parameters are shown in the test matrix shown in Table 7.

Table 7: Test matrix for analyzing the effect of time on sour dewing systems

Parameter	Value
Test Material	API 5L X65
Total Pressure (bar)	1
H₂S Partial Pressure (mbar)	0.3
O₂ Partial Pressure (mbar)	0
CO₂ Partial Pressure (bar)	0.96
N₂ + Ar Partial Pressure (bar)	0
Test Duration (days)	0.25, 1, 3, 7, 10
Water Condensation Rate (ml/m²/s)	0.015
Steel Temperature (°C)	25
Gas Temperature (°C)	30

The effect of time on the corrosion product layer morphology is shown in Figure 17. After 6 hours, the only visible corrosion product was confined to the structures shown. Flakes were already beginning to form, but no buckling was observed. FeS layer buckling was evident after 1 day where the buckled corrosion product was evident only surrounding the flakey structures seen after 6 hours. The severity of buckling intensified with time developing large buckled regions after 7 days. Similar sized features were not observed after 10 days as they likely had been removed from the surface due to spallation.

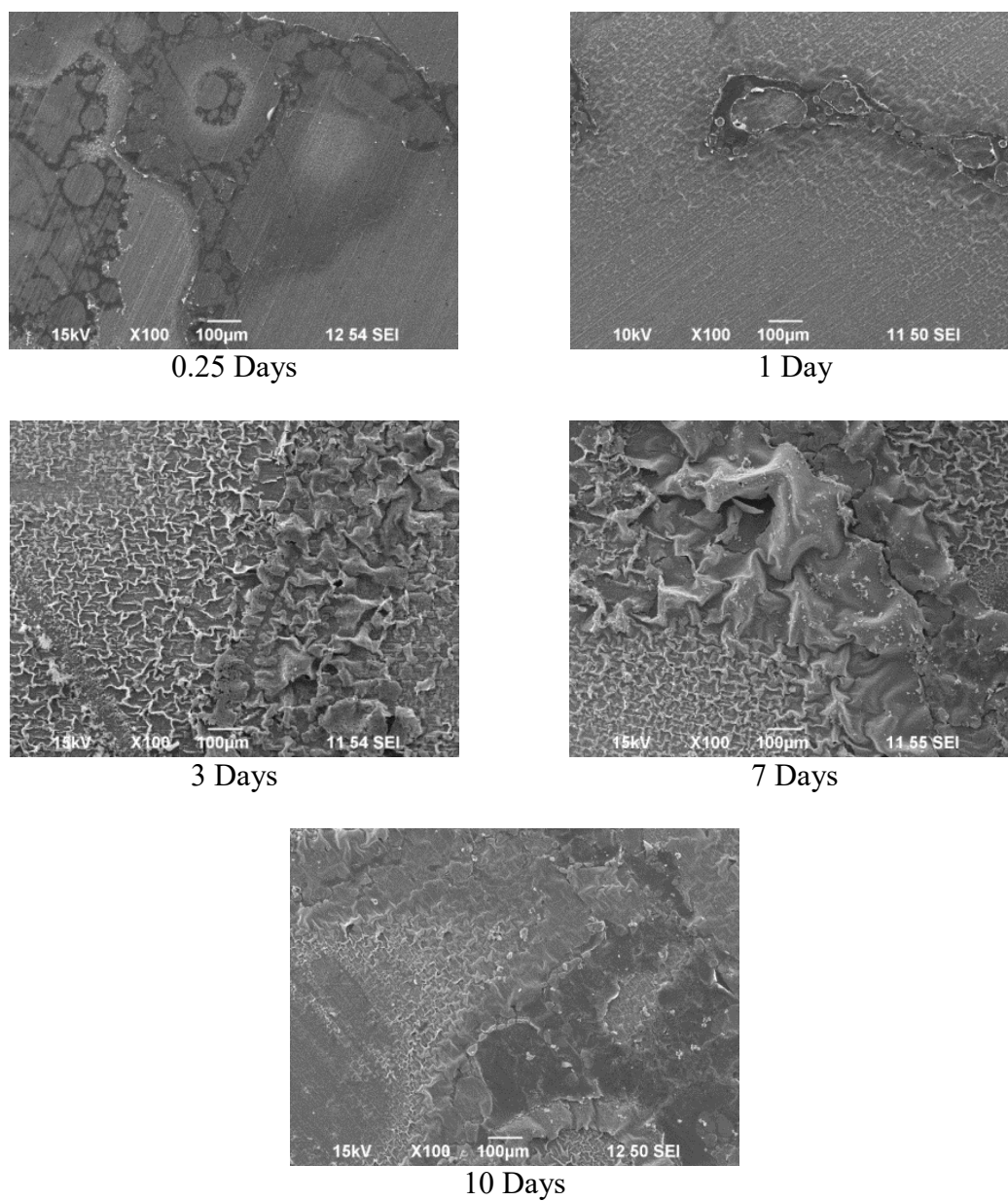


Figure 17: Effect of Time on Corrosion Product Morphology (0.3 mbar H₂S, 0.96 bar CO₂, 0 mbar O₂, 0.015 ml/m²/s WCR, 25 T_{steel}, 30°C T_{gas})

The effect of time on the corrosion product composition is shown in Figure 18. No change in phase identity associated with corrosion product was observed, however,

absolute peak intensities generally increased as the corrosion product developed. No XRD measurements were performed on the specimen retrieved after 6 hours.

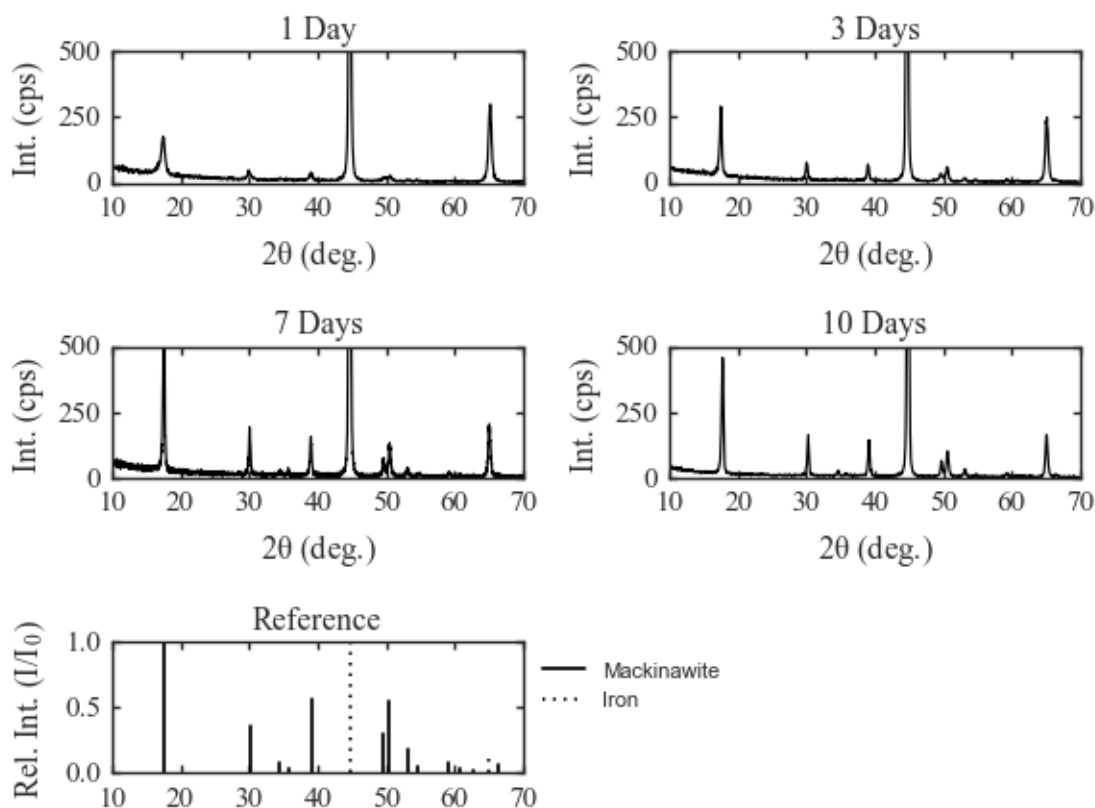


Figure 18: Effect of time on corrosion product composition

Time dependency relating to corrosion rate is shown in Figure 19. The corrosion rate decreased with time from 0.28 mm/yr to a steady corrosion rate of 0.10 mm/yr after corrosion product, which can offer some protection, had time to develop on the steel surface. The error in the measurement decreased significantly over time since mass measurement uncertainties had less impact on the error-propagated result as time increased.

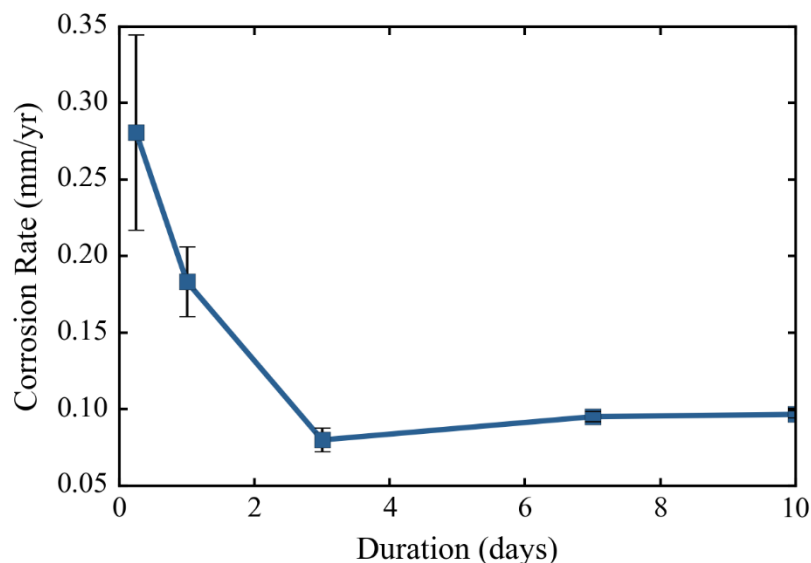


Figure 19: Effect of time on corrosion rate at 0.3 mbar pH₂S and low WCR.

As shown in Figure 20, the measured corrosion product mass on the steel surface is approaching a steady value near 10 g/m² while the theoretical corrosion product mass becomes approximately linear with time. This combined with the changes in corrosion product morphology over time indicate the corrosion product formation rate and spallation rate are approaching equilibrium and may ultimately lead to a black powder production rate of *ca.* 1000 kg/day for a 100 km, 42 in. ID pipeline. Note, the errors in the measured and theoretical corrosion product mass measurements were relatively constant since they are based solely on gravimetric measurements and did not consider time, whereas the maximum possible black powder production rate is based on the corrosion rate, which had time to negate some of the effects of mass measurement error propagation.

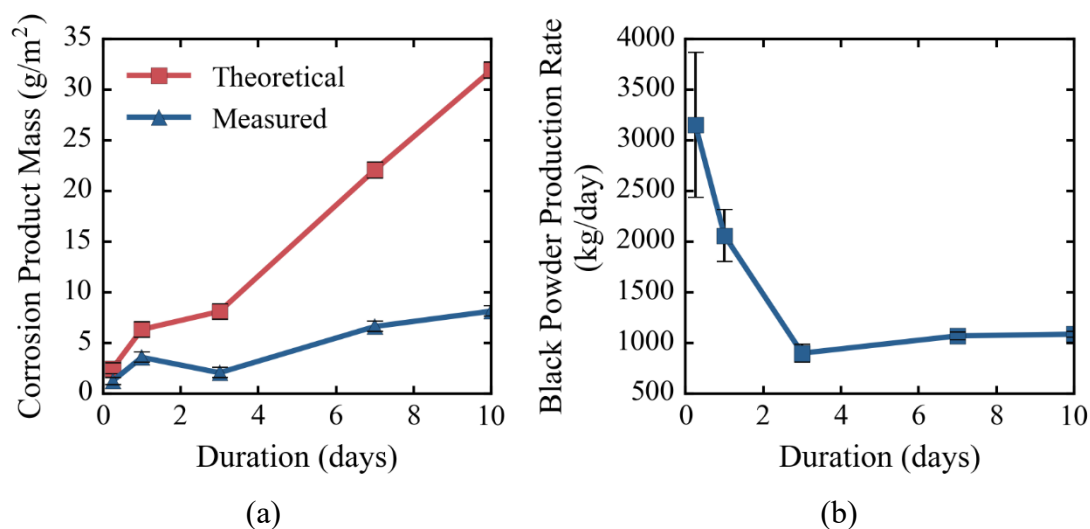


Figure 20: Effect of time on (a) corrosion product mass and (b) maximum possible black powder production rate in a 100 km long, 42 in. ID pipeline at 0.3 mbar pH₂S and low WCR.

5.1.3 FeS Layer Buckling

The increased degree of buckling with increasing H₂S partial pressure and time in the FeS layers is related to the accumulation of compressive stress accompanying FeS layer growth. Spontaneous buckling and layer delamination occurs to release stored energy within the intrinsically stressed FeS layer.

Stress accumulation may be caused through a variety of pathways. In the Sun-Nesic model [20] of iron sulfide layer formation, stress accumulation, which leads to cracking and spallation, is postulated to be due to volume differences between the ferrite and the mackinawite. The ratio of the scale volume to the substrate volume, more commonly known as the Pilling-Bedworth ratio (PBR) [44], for FeS relative to ferrite is about 2.6. Since the PBR is greater than 1, compressive stress within the layer is expected to

accumulate and lead to layer failure. However, the PBR is not especially useful for layers grown through outward cation diffusion, which is the case for most sulfides. Iron cations may diffuse faster than the much larger sulfide anions. Layers predominantly grown *via* outward cation diffusion can grow outward from the scale surface and, therefore, are not volume limited as required to apply the PBR [45].

Sun and Nestic suggest epitaxial stresses, which arise due to unit cell size differences may lead to stress accumulation [20]. However, the adherence of the sulfide to the metal is expected to be fairly weak due to void formation as the steel substrate corrodes, which may limit epitaxial stresses [38]. A perhaps more plausible method of stress accumulation may be due to crystal growth at cracks, pores, and grain boundaries. Crystal growth due to the addition of ferrous and sulfide ions to an already formed crystal may lead to crystals pushing against one another therefore compressively stressing the layer. Crystal growth at grain boundaries and cracks has been used to explain the buckling of chromium oxide scales and oxide scales on Fe-Cr-Al alloys [45]–[48].

In all H₂S experiments, black particles were present in collected fluid after the isopropanol rinse of extracted specimens. The wall shear stress imposed by the isopropanol was estimated to be approximately 1 Pa based on the flow of a falling laminar film [49]. This shear stress is similar to the wall shear stress in the GASCO pipeline. It is unlikely this small shear stress would cause damage to a corrosion product layer experiencing little to no intrinsic stress, so it is proposed that black powder formation due to H₂S is predominantly caused by intrinsic stresses within the layer generated by layer growth rather

than the extrinsic stresses caused by fluid flow. Further study is needed to better quantify the accumulation of stress as the layer grows to better predict spallation.

5.1.4 Effect of O₂ on Sweet Dewing Corrosion

The effect of oxygen was examined by exposing steel specimens at the low WCR of 0.015 ml/m²/s to a CO₂/air mixture with a 10 mbar O₂ partial pressure. Test conditions are shown in Table 8.

Table 8: Test matrix for the investigation of the effect of O₂ on sweet dewing corrosion

Parameter	Value
Test Material	API 5L X65
Total Pressure (bar)	1
H₂S Partial Pressure (mbar)	0
O₂ Partial Pressure (mbar)	0, 10
CO₂ Partial Pressure (bar)	0.96, 0.92
N₂ + Ar Partial Pressure (bar)	0, 0.04
Test Duration (days)	3
Water Condensation Rate (ml/m²/s)	0.015
Steel Temperature (°C)	25
Gas Temperature (°C)	30

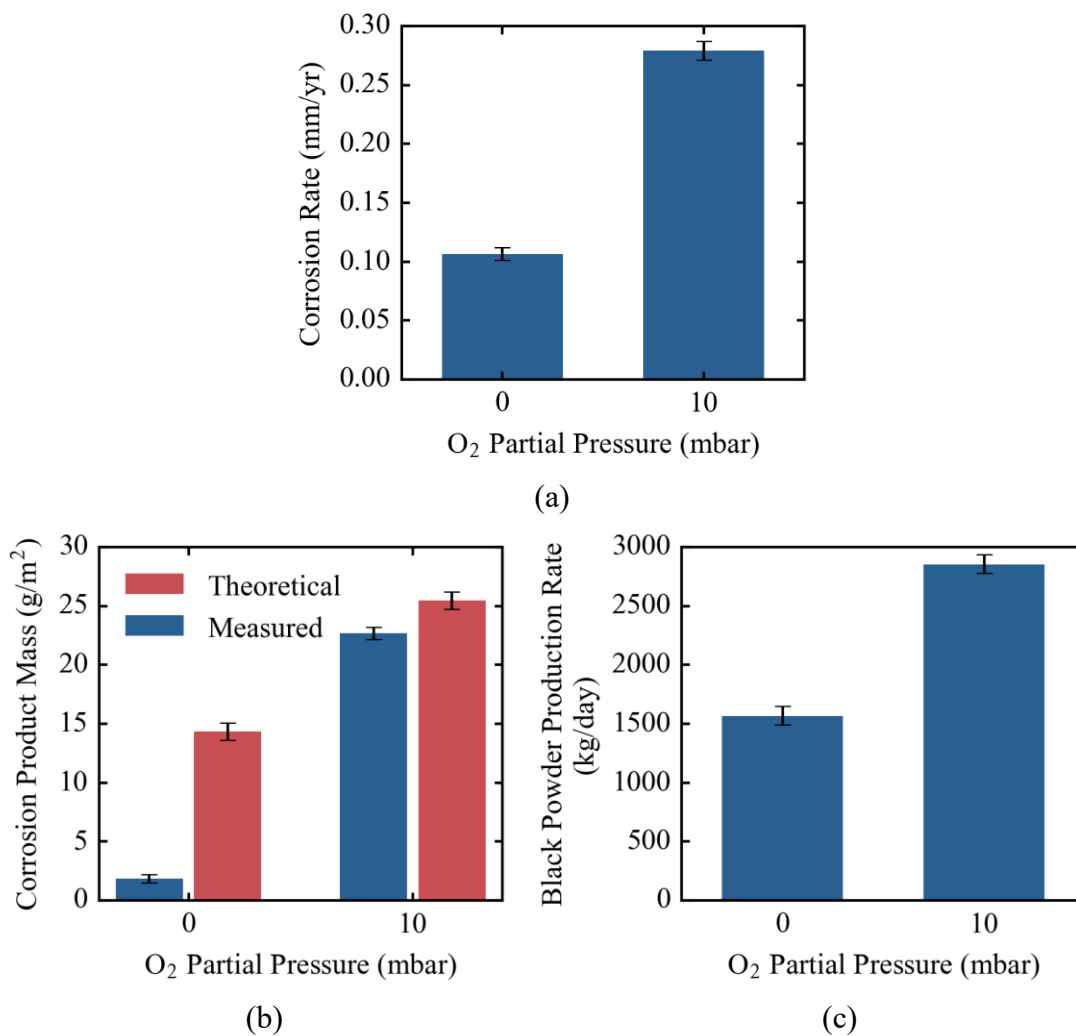


Figure 21: Effect of O₂ on (a) corrosion rate, (b) measured and theoretical corrosion product mass, and (c) maximum possible black powder production rate in a 100 km, 42 in. ID pipeline.

The addition of oxygen to a CO₂ environment saw, as expected, a dramatic increase in corrosion rate and corrosion product mass, as shown in Figure 21(a) and Figure 21(b). The measured corrosion product mass was much closer to the theoretical corrosion product

mass than the CO₂-only experiment indicating the water chemistry was more favorable for precipitation.

The dramatic increase in the corrosion rate and corrosion product mass resulted in development of a bilayered corrosion product, as shown in the SEM cross-section in Figure 22(a). The inner layer shown in Figure 22(b) was well adhered to the steel, but the outer layer, Figure 22(c), was more loosely bound. Red flakes of corrosion product were observed in the collected isopropanol after rinsing, which suggests black powder components would readily detach.

The origin of the outer layer is unclear. The outer layer is presumed to have grown on the gas/liquid interface since a flat surface is present on the outer layer, whereas the inner layer is more rough. It is postulated that the precipitation of iron carbonate in the bulk occurred away from the steel surface whereupon it collected at the gas/water interface due to gravity.

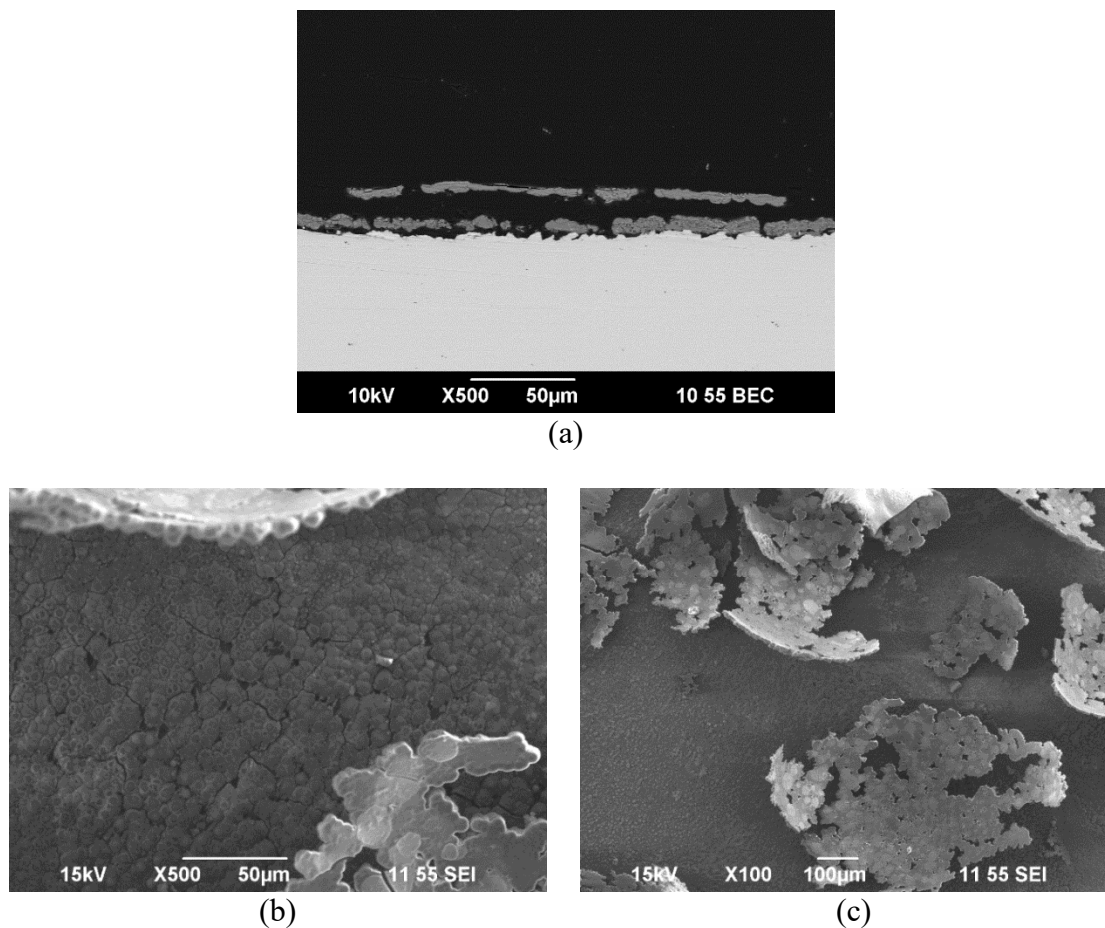


Figure 22: Surface analysis of corrosion products formed after a 3 day exposure to a 10 mbar O_2 – 0.92 bar CO_2 atmosphere at the low WCR.

Seemingly contradictory results were obtained from corrosion product composition analysis with XRD and Raman spectroscopy as shown in Figure 23. Siderite ($FeCO_3$) was detected with XRD, but hematite (Fe_2O_3) was detected by Raman spectroscopy. It is postulated that an amorphous or nanocrystalline hematite layer was present on the corrosion product surface, which cannot be detected by XRD but is detected by Raman spectroscopy. Indeed, the high XRD baseline is also indicative of the presence of an

amorphous corrosion product. As Raman is more surface specific, the iron carbonate beneath the iron oxide was undetected.

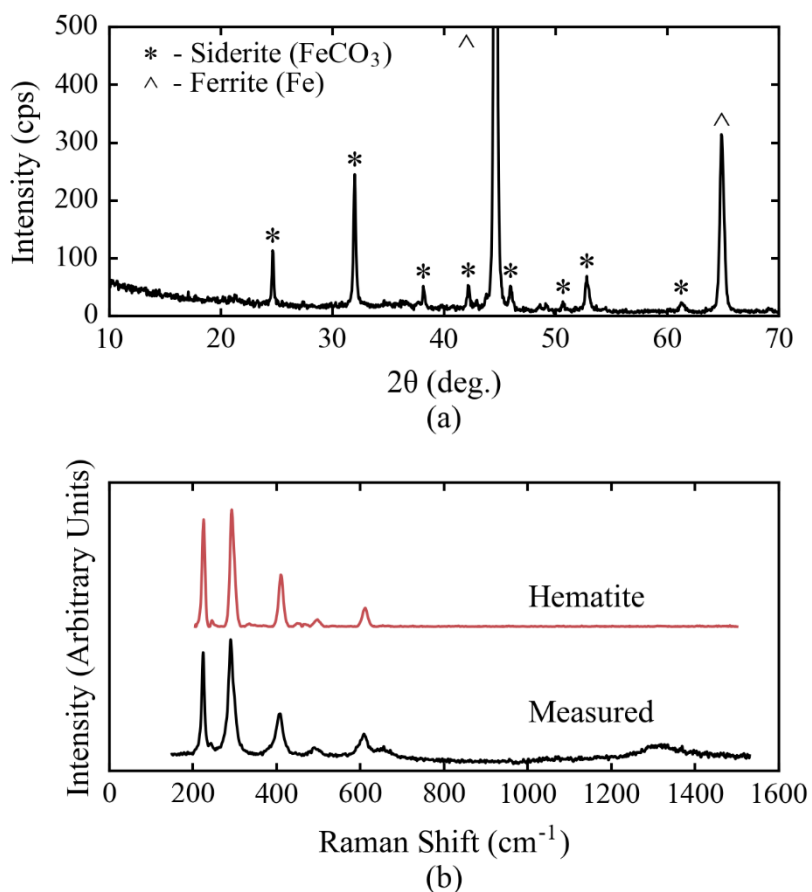


Figure 23: (a) XRD and (b) Raman spectroscopy compositional analysis of corrosion product formed after a 3-day exposure to a 10 mbar O_2 – 0.92 bar CO_2 atmosphere at the low WCR. The red hematite spectrum is added as a reference [50].

Under pure CO_2 environments, corrosion products were minimal and consisted primarily of iron carbide. However, the predominance of iron carbonate over iron oxyhydroxides and iron oxides even in the presence of dissolved O_2 suggests black powder

formation may still be possible under pure CO₂ conditions if conditions are favorable for precipitation to occur into a morphology, such as the bilayered morphology seen above, capable of producing detached to marginally attached particles of corrosion products.

5.1.5 Effect of Cyclic Water Condensation

Pipeline conditions are not static. Temperatures are expected to change throughout the year and even throughout the day due to meteorological conditions. To examine the effect of temperature fluctuations on the corrosion product, the temperature of the specimens was changed every 12 hours between 25°C and 40°C. These temperature changes are supposed to mimic temperature changes that occur due to the day/night cycle. Experimental conditions are summarized in the test matrix in Table 9.

Table 9: Test matrix for the investigation of the effect of cyclic water condensation

Parameter	Value
Test Material	API 5L X65
Total Pressure (bar)	1
H₂S Partial Pressure (mbar)	0.3
O₂ Partial Pressure (mbar)	0
CO₂ Partial Pressure (bar)	0.96
N₂ + Ar Partial Pressure (bar)	0
Test Duration (days)	3, 7
Water Condensation Rate (ml/m²/s)	0.015, 0
Steel Temperature (°C)	25, 40
Gas Temperature (°C)	30
Temperature Cycle Period (days)	1 (change every 12 hours)

SEM surface analysis was performed after each experiment to examine the effect of temperature cycling on the corrosion product morphology. The surfaces of specimens that experienced cyclic water condensation are compared to their constant WCR counterparts in Figure 24. Overall, FeS spalling was more apparent in the constant WCR experiments than the cycling experiments. The less sheet-like characteristics of the cycled corrosion product layers, as compared to the layers formed under constant water condensation rates, is likely a result of high FeS precipitation rates as water was quickly removed from the steel surface. It is postulated that precipitated corrosion product would have settled on layers similar to those observed from the constant WCR experiments, thereby reinforcing the structural integrity of the layer making spalling less pronounced.

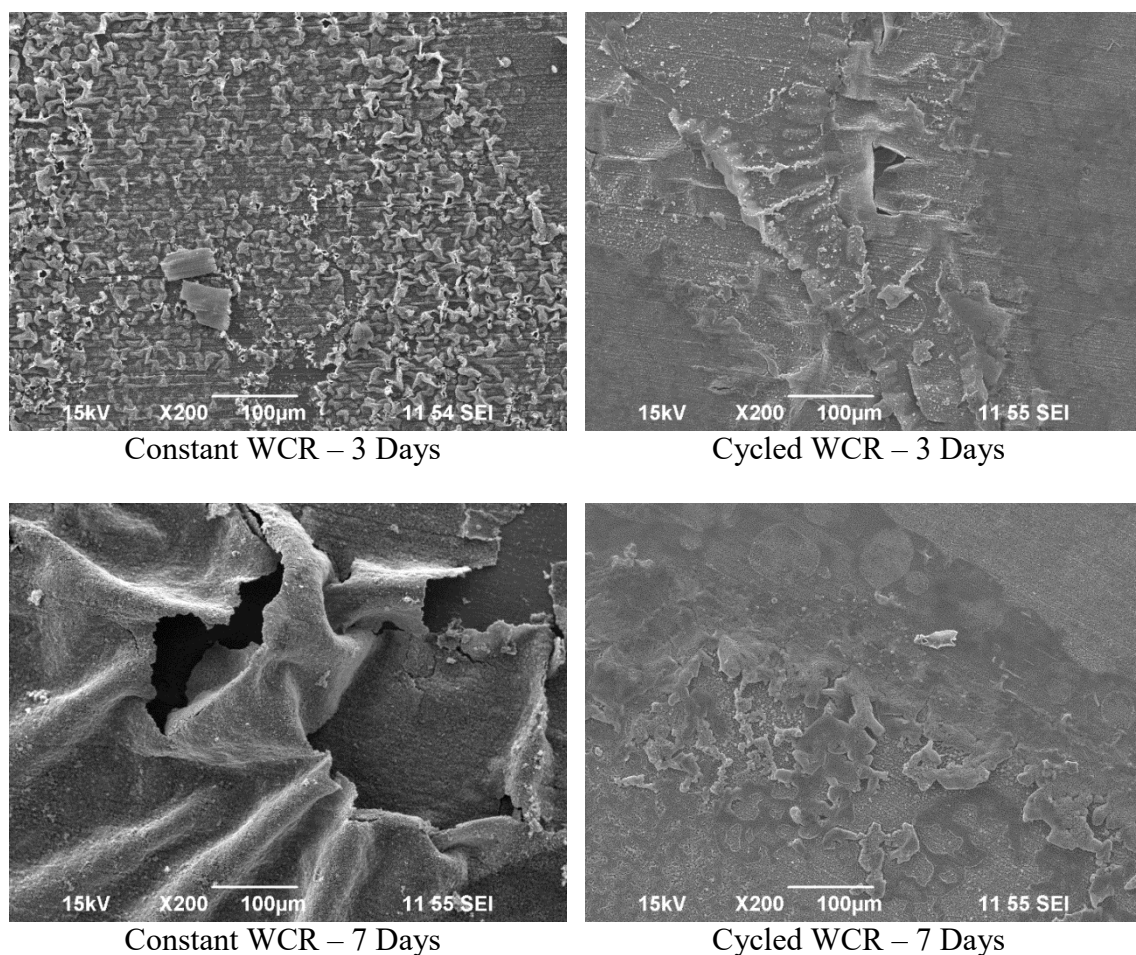


Figure 24: Effect of cyclic water condensation on corrosion product morphology.

The effect of cyclic water condensation on the corrosion product composition determined by X-ray diffraction is shown in Figure 25. Mackinawite was the primary corrosion product detected, but siderite was also detected in the corrosion product developed after 7 days under cycling conditions. Peak broadening is apparent in the temperature cycled experiments. It is postulated that the fast precipitation rates caused by the drying process results in growth of small mackinawite crystals or induces lattice strain

as the ions coalesce in thermodynamically unfavorable locations thus inducing peak broadening.

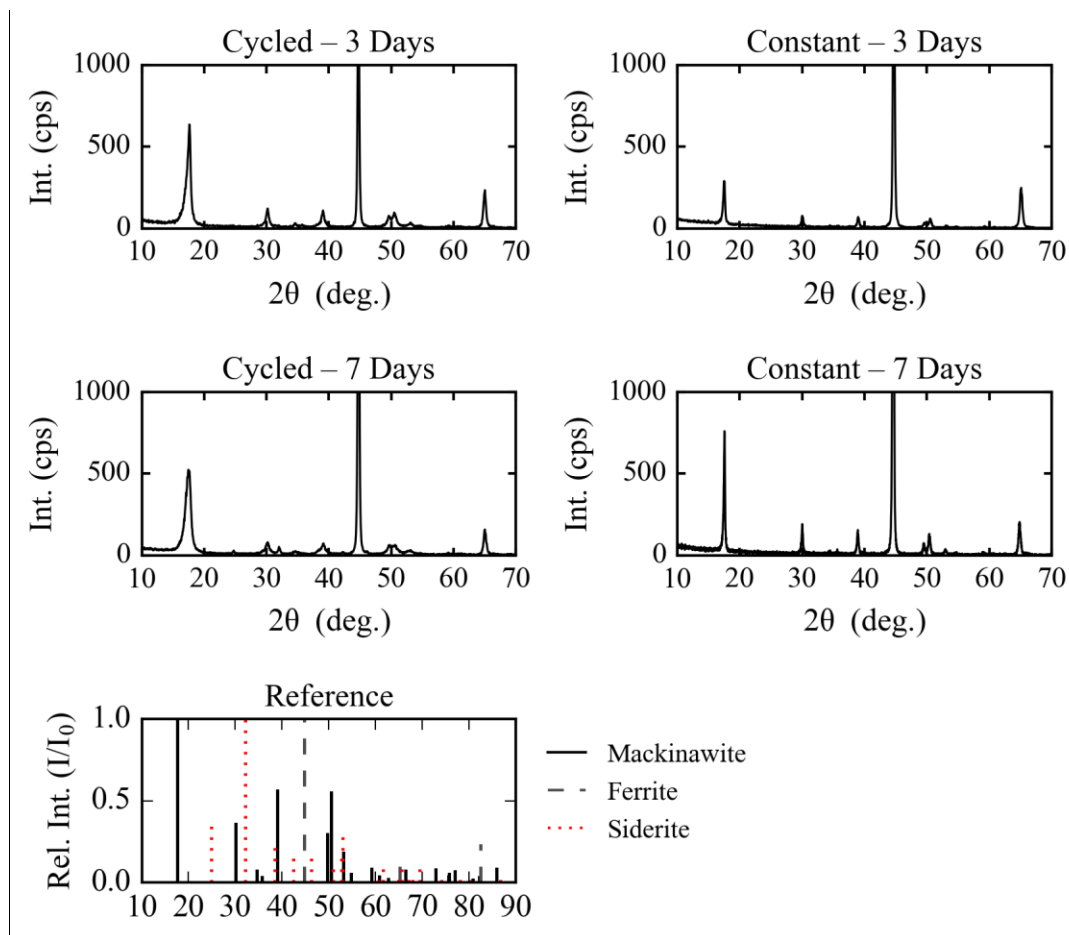


Figure 25: Effect of cyclic water condensation on the corrosion product composition.

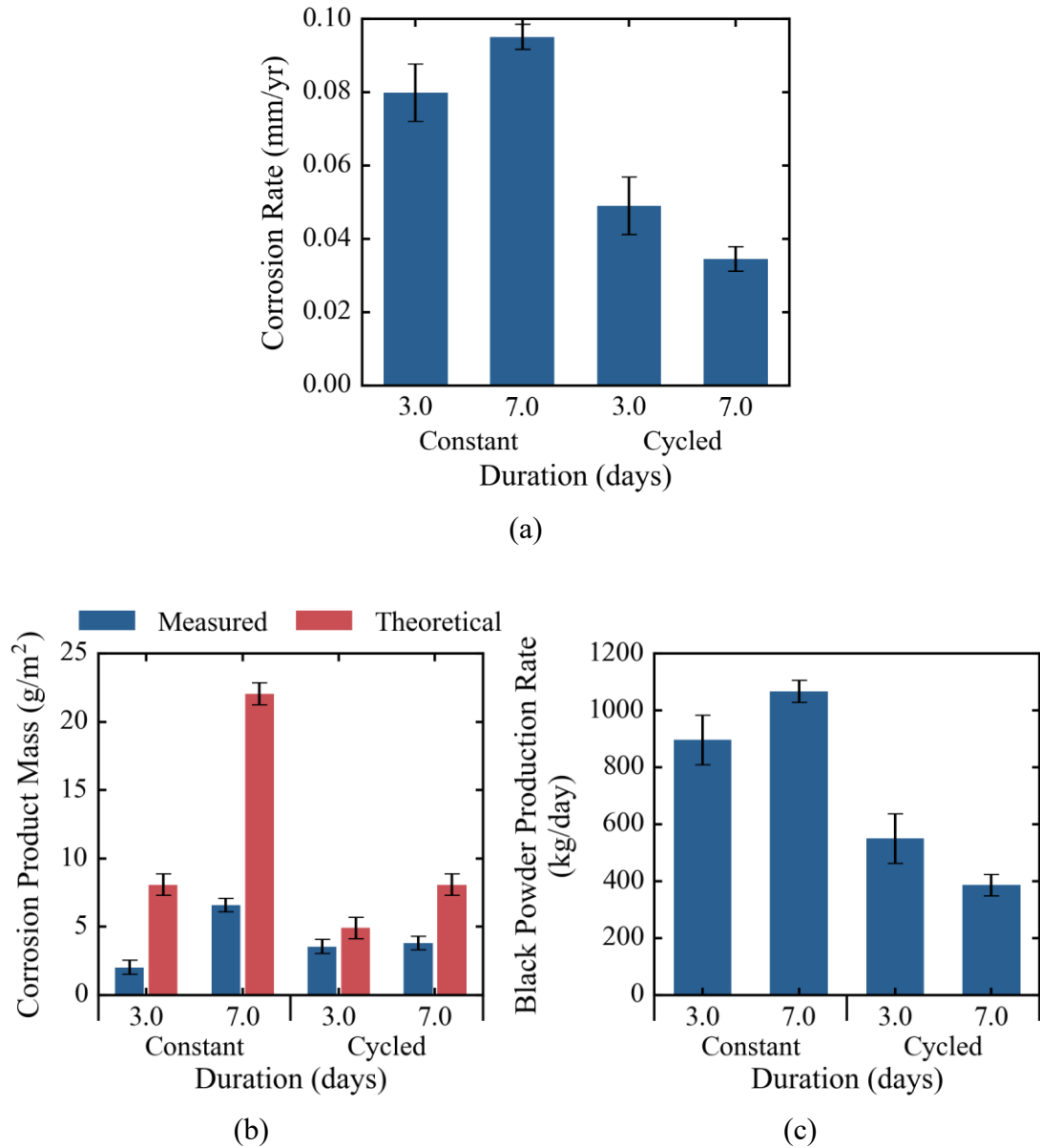


Figure 26: Effect of temperature cycling on (a) corrosion rate, (b) measure and theoretical corrosion product mass, and (c) maximum possible black powder production rate in a 100 km, 42 in. ID pipeline.

The effect of temperature cycling on corrosion rate, corrosion product mass, and maximum possible black powder production rate is illustrated in Figure 26. As would be expected for the case of a steel surface water wetted for about half the experimental duration, the corrosion rates of the cycled specimens were less than those from the constant WCR conditions. However, while the corrosion rate from the 3 day-cycled experiment was about half of its constant WCR counterpart, the corrosion rate from the 7 day – cycled experiment was $36 \pm 4 \%$ of the 7 day – constant WCR corrosion rate suggesting that the solid corrosion product produced during the drying phase is more protective than the buckled layers produced under constant water condensation rates.

5.1.6 Black Powder Formation in Dewing Conditions

Corrosion products susceptible to black powder formation were produced in conditions favorable to corrosion product precipitation and iron sulfide film forming conditions. The precipitated corrosion product formed in oxic conditions consisted of two layers. The outer layer is the more likely layer to detach and form black powder as the inner layer is attached to the steel with no evidence of inner layer delamination. The outer layer appeared only loosely held to the steel surface with portions projected away from the surface, which would make the layer more susceptible to removal by a flowing gas stream. The bilayered morphology is postulated to only occur at the top of the pipeline (*i.e.*, 12 o'clock position) where iron carbonate, which nucleated away from the steel surface, can collect at the gas/liquid interface. Away from the top of the line, gravity will likely draw precipitated products back to the steel surface to merge with the inner layer.

Spalling corrosion product films were ubiquitous in H₂S-containing conditions under constant water condensation rates. These thin films were likely a results of the direct reaction of H₂S to the steel, which forms a framework for iron sulfide precipitation as per Zheng's model of sour corrosion [21]. The spallation of these thin films occurs as intrinsic stresses, which accumulate during layer growth, then relax during the buckling process. A gas pipeline experiencing water condensation would likely have to contend with this method of black powder formation over the entire pipe wall as there is no bilayered morphology. It appears the only requirement to form these types of layers is a water-wetted surface and the presence of H₂S.

Corrosion products formed under dewing conditions include siderite, mackinawite, and hematite. Of the three, mackinawite is metastable and its transformation to more thermodynamically favored corrosion products is likely hindered at the temperatures in which the experiments were conducted.

Spallation was not as pronounced under temperature cycling condition where it appears corrosion product formed through precipitation served to structurally reinforce the iron sulfide layer. No major change in corrosion product composition was obtained due to temperature cycling.

To mitigate the formation of black powder due to dew formation within the pipeline, proper gas dehydration is absolutely necessary. Dehydrating the gas to below 100% RH, however, may not be completely effective. The potential for corrosion below 100% RH is investigated in the following section.

5.2 Hygroscopic Corrosion

The presence of hygroscopic material such as a salt is hypothesized to sustain corrosion in water unsaturated conditions, which can lead to black powder formation. The possibility of hygroscopic salts sustaining corrosion at a relative humidity (RH) below 100% was investigated by depositing NaCl on polished steel specimens and exposing the specimens to differing H₂S partial pressures and relative humidities. The test matrix that guided hygroscopic corrosion experimentation is shown in Table 10, below.

Table 10: Hygroscopic corrosion test matrix

Parameter	Value
Test Material	API 5L X65
Total Pressure (bar)	1
H₂S Partial Pressure (mbar)	0, 0.1, 0.3, 1.0
O₂ Partial Pressure (mbar)	0
CO₂ Partial Pressure (bar)	0.97
N₂ + Ar Partial Pressure (bar)	0
Test Duration (days)	3
Relative Humidity (%)	33, 58, 75
Saturated Salt Solution	MgCl ₂ , NaBr, NaCl
Temperature (°C)	25
Salt Layer	NaCl

5.2.1 Salt Layer Generation

Surface microscopy of the salt layer, generated by drying a 3.5 wt% NaCl/deionized water solution onto a steel surface polished to a mirror finish, is shown in Figure 27. The

solution was purged with N_2 prior to deposition, and drying was performed by passing dry N_2 over the steel specimen and allowing the water to evaporate, slowly.

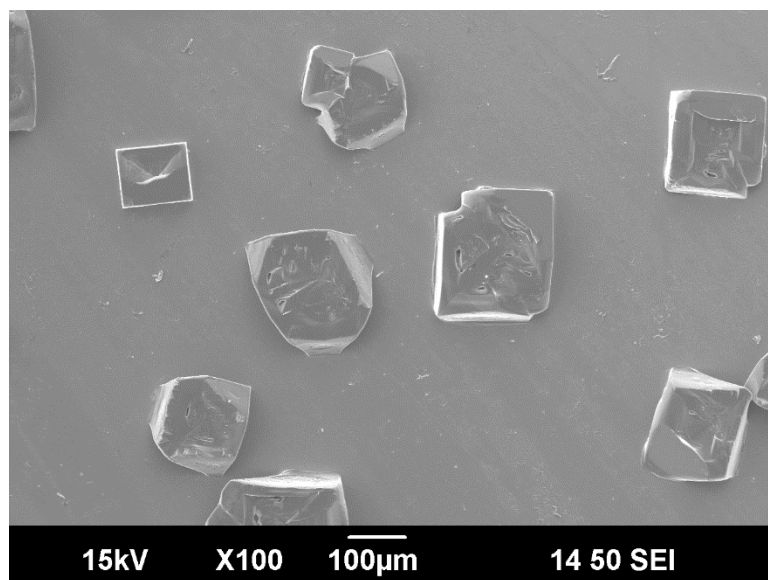


Figure 27: SEM analysis of the NaCl layer formed before specimen insertion into test environment. The specimen was coated with palladium to minimize electron beam charging.

As seen in Figure 27, the salt was predominantly grouped into roughly cubic structures approximately 100 μm in width. A slight salt residue is apparent on the steel surface between the large salt crystals.

The salt layer generation method produced some pitting on the outside of the border of crystals, as shown in Figure 28. The micrographs shown in Figure 28 were taken after the rinsing the salt layer shown in Figure 27 with N_2 -purged DI water. The methodology employed during salt generation, sputter coating, SEM, and salt removal of the salt layer

in the micrographs is the same as during experimentation, therefore the attack morphology would propagate to the experiments, whose results are shown in subsequent sections. Attack beyond that shown in Figure 28 is a result of exposure to the atmosphere dictated by the hygroscopic corrosion experiments. No change in steel mass was measured as a result of salt layer deposition and removal.

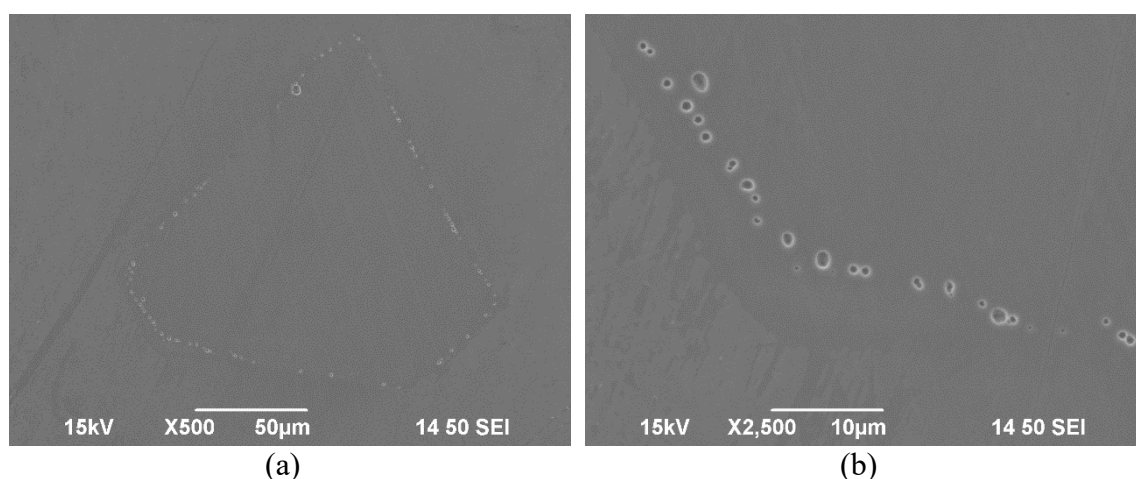


Figure 28: Slight localized corrosion on the outside boundary of a salt crystal formed by drying NaCl.

5.2.2 *Hygroscopic Corrosion in Sweet Environments*

Surface microscopy of specimens exposed to CO₂ atmospheres under deliquescing conditions (75% RH) is shown in Figure 29. The occurrence of deliquescence is evident at 75% due to the small size of the cubic salt crystals relative to those seen in Figure 27. Distinct regions were found under deliquescing conditions, which are the darker and the lighter regions seen in Figure 29(a) and better detailed in the enlarged micrograph in Figure 29(b). More corrosion product is found in the darker shaded regions, whereas coverage was

sparser in the circular region where islands of corrosion product were obtained amidst a material structurally consistent with iron carbide. EDS analysis of a similar region shown in Figure 30 indicates the corrosion product is compositionally consistent with iron carbonate, which was also more generally detected by XRD, as shown in Figure 31.

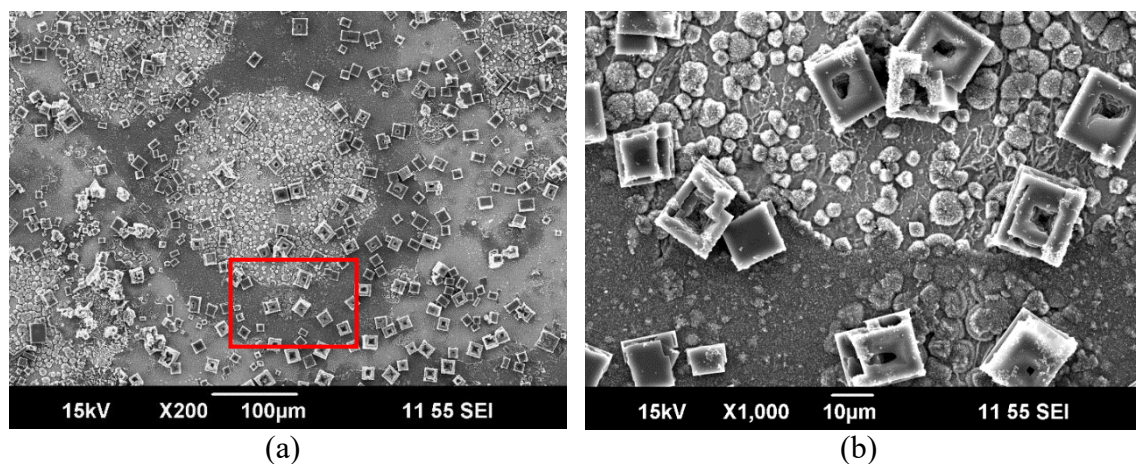


Figure 29: (a) Surface microscopy after a 3 day exposures to CO₂ atmosphere at 75% RH.

The region outlined in red is enlarged in (b).

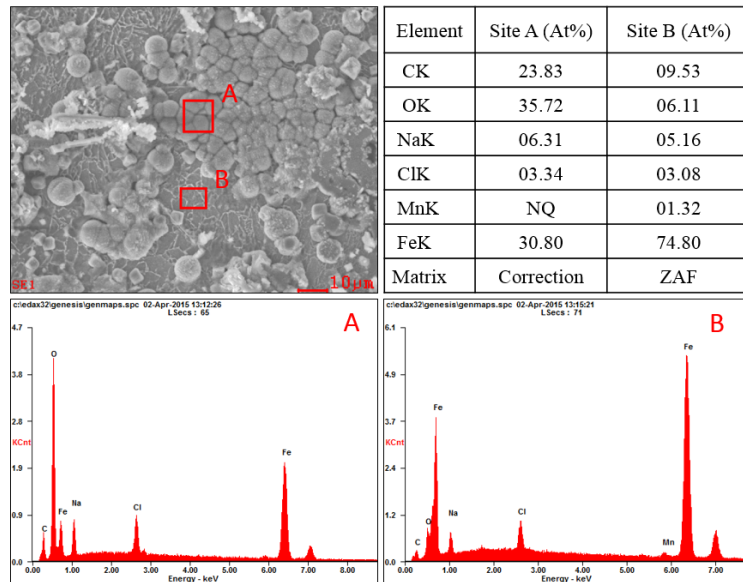


Figure 30: EDS of corrosion product after a 3 day exposure to a CO₂ environment at 75% RH. NQ: Not Quantified.

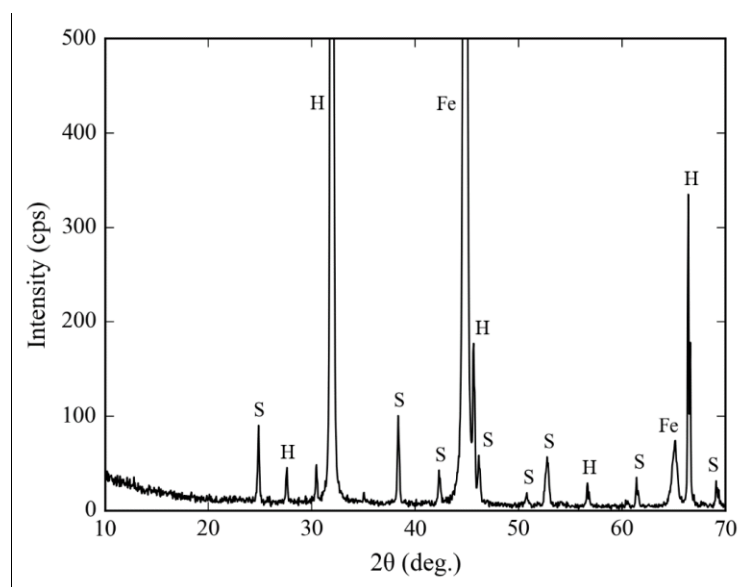


Figure 31: XRD corrosion product composition analysis of specimens recovered after a 3 day exposure to CO₂ at 75% RH. Peak labels are S: siderite (FeCO₃), H: halite (NaCl), and Fe: ferrite (Fe).

The reason for the non-uniform corrosion product is unclear but is attributed to the presence of a large salt crystal that once covered the circular area. The circular shape compared to the typical cubic shape is due to the rounding of the NaCl crystal edges during deliquescence, a phenomenon witnessed by Wise, *et al.*, [51] with environmental transmission electron microscopy.

Significant corrosion took place beneath the salt crystal as evident by the approximately 1 μm difference between regions beneath salt crystals and the surrounding regions in the surface profilometry shown in Figure 32. Deeper localized corrosion was also observed typically beneath the smaller crystals than the larger crystals.

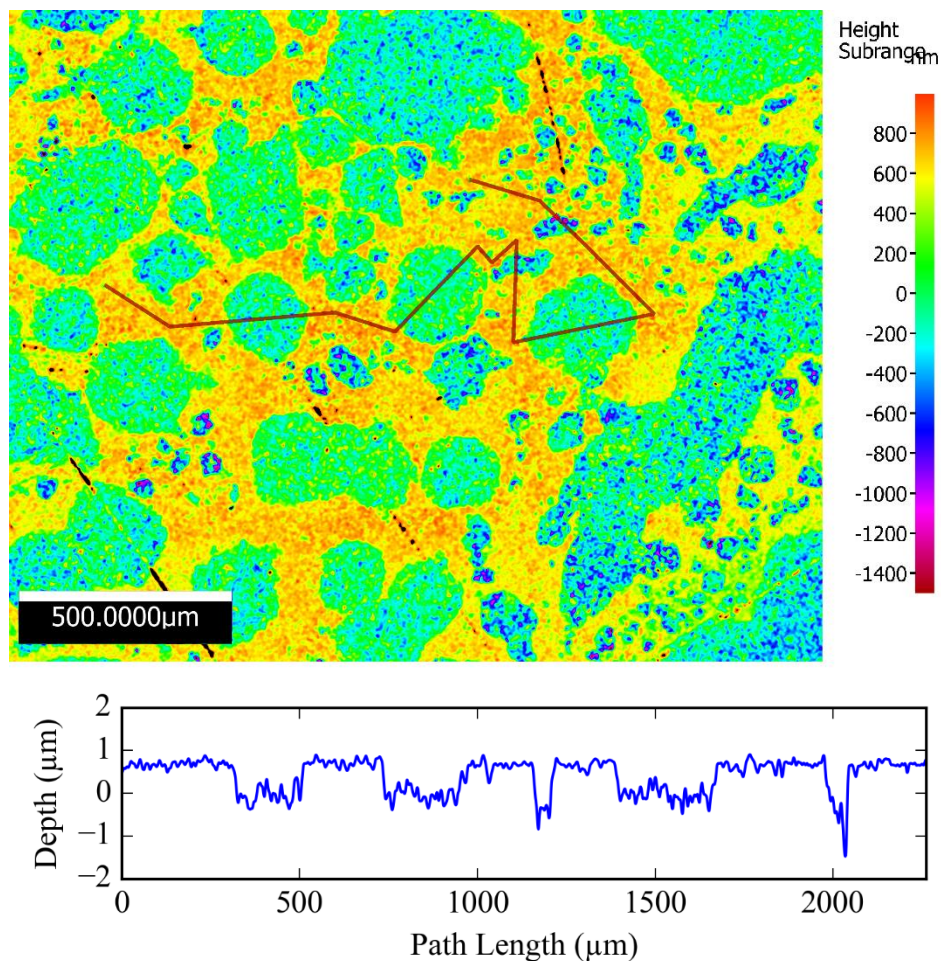


Figure 32: Surface profilometry of specimen recovered after a 3 day exposure to CO_2 at 75% RH. Scale bar units are in nm.

Corrosion product was not directly observable by SEM after a 3-day exposure to CO_2 at 58% and 33% RH, as shown in Figure 33. The large NaCl crystals were still present at 58% and 33% RH indicating deliquescence did not occur, however, a ring surrounding the salt crystal is apparent at 58% RH. Also, no corrosion product was detected by XRD beneath the DRH of NaCl in CO_2 conditions.

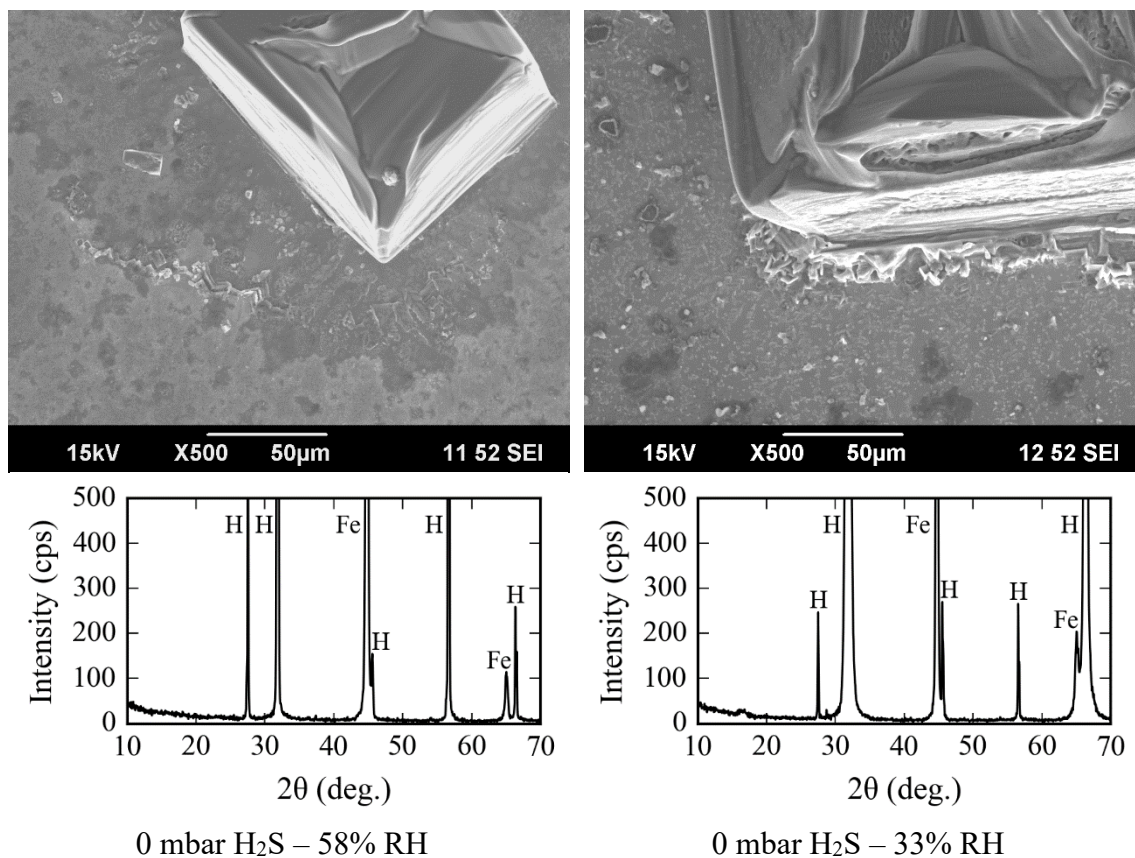


Figure 33: Surface microscopy and XRD compositional analysis after a 3 day exposure to CO₂ at 58 and 33% RH.

The effect of relative humidity on the general corrosion rate due to hygroscopic corrosion in CO₂ atmospheres is shown in Figure 34(a). As expected, the corrosion rate increased with the availability of water in the atmosphere; however, the corrosion rates were all very small. The corrosion rate at 33% RH cannot be distinguished from no corrosion due to its small value and gravimetric measurement uncertainty. The small corrosion rates are partially owed to the nonuniform coverage of the salt layer making

hygroscopic corrosion an inherently localized system. Despite these reservations, a general corrosion rate is still useful for comparison purposes, so the value is still provided.

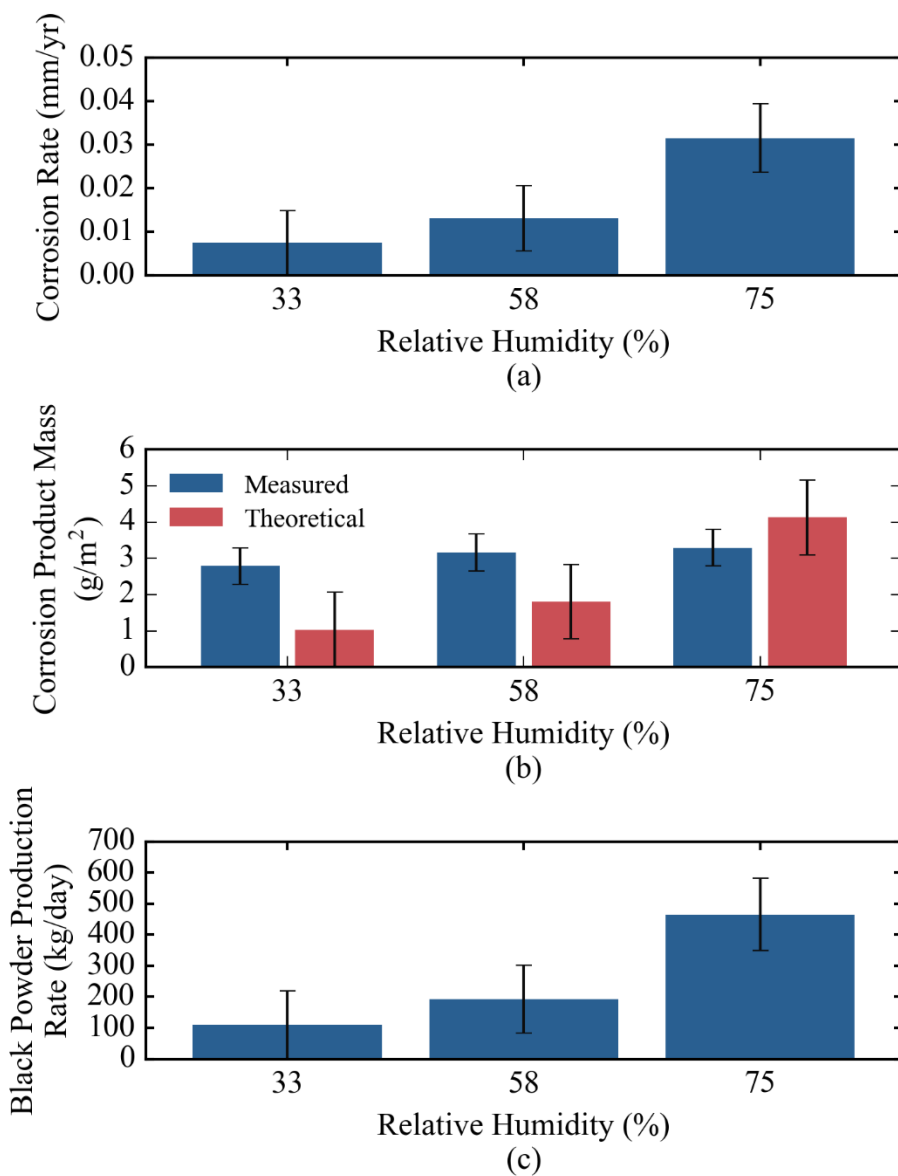


Figure 34: Effect of relative humidity on (a) general corrosion rate, (b) measured and theoretical corrosion product mass, and (c) maximum possible black powder production rate in a 100 km, 42 in. ID pipeline under hygroscopic CO₂ conditions.

The effect of relative humidity on the corrosion product mass and black powder production rate is shown in Figure 34(b) and Figure 34(c), respectively. Below the DRH, the measured corrosion product mass was higher than the theoretical corrosion product mass. This is believed to be due to the presence of NaCl in the corrosion product that could not be rinsed off before the corrosion product was removed.

5.2.3 *Hygroscopic Corrosion in Sour Environments*

The morphology of corrosion products obtained in deliquescing conditions is shown in Figure 35. Flakey corrosion products potentially susceptible to spallation were only obtained at 0.3 and 1.0 mbar H₂S where the corrosion product appeared to create a shell around the location once occupied by a salt crystal. Corrosion product formation atop of the salt crystal is postulated to be due to ferrous ion diffusion through the water layer surrounding the deliquescing salt crystal. FeS precipitation then occurred with sulfides already present. The shell of corrosion product would then be all that remains once the salt crystal fully deliquesces. No evidence of a friable corrosion product was found at 0.1 mbar H₂S.

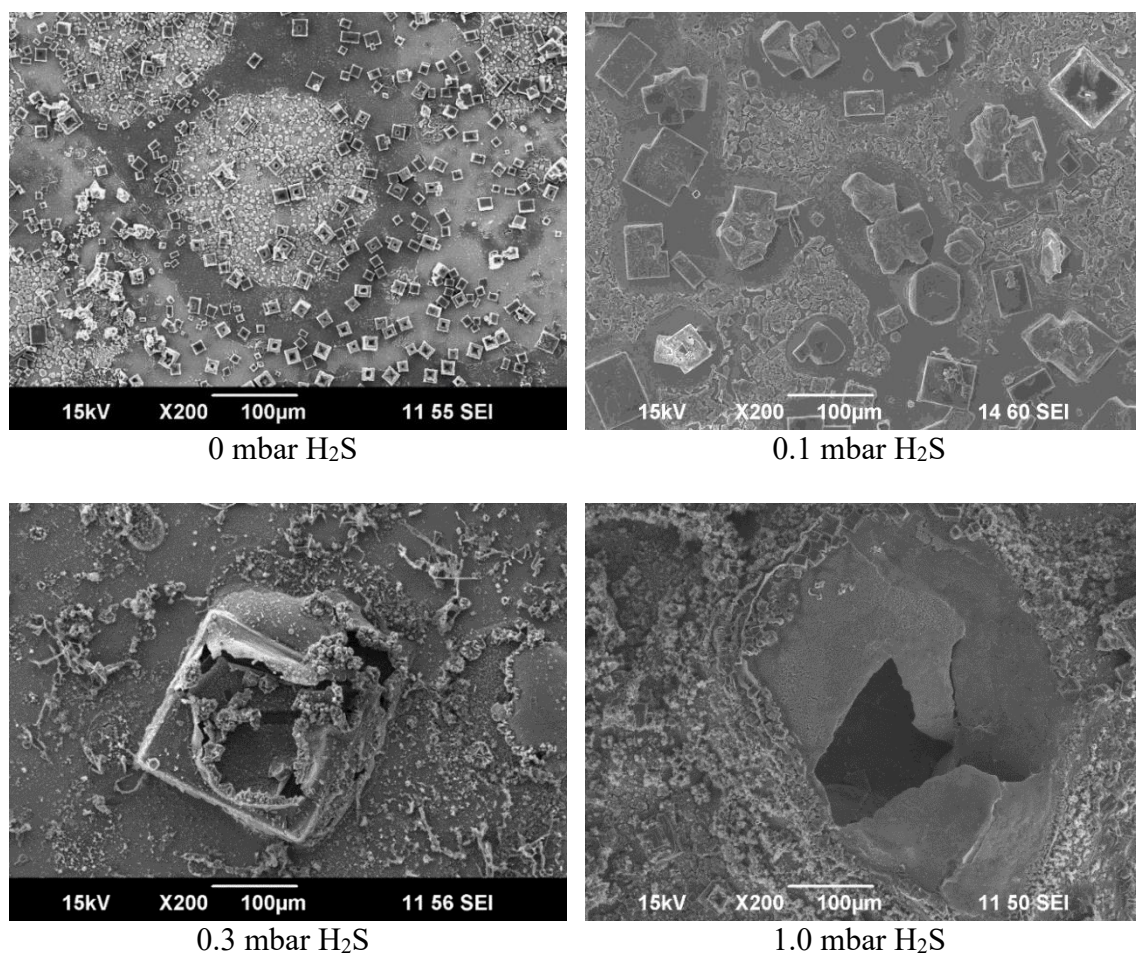


Figure 35: Effect of H₂S partial pressure on corrosion product morphology in deliquescing conditions (75% RH, 0.97 bar CO₂).

The effect of H₂S partial pressure on the composition of corrosion products formed under deliquescing conditions is shown in Figure 36. With the increase of H₂S partial pressure to 0.1 mbar, mackinawite was the dominant phase, however the [001] peak at 17.6° 2θ was quite broad. At 0.3 mbar and 1.0 mbar H₂S, both siderite and mackinawite were present with an additional unknown phase(s). The baseline of the diffraction patterns

collected at 0.3 and 1.0 mbar H₂S were high indicating the presence of amorphous or nanocrystalline material.

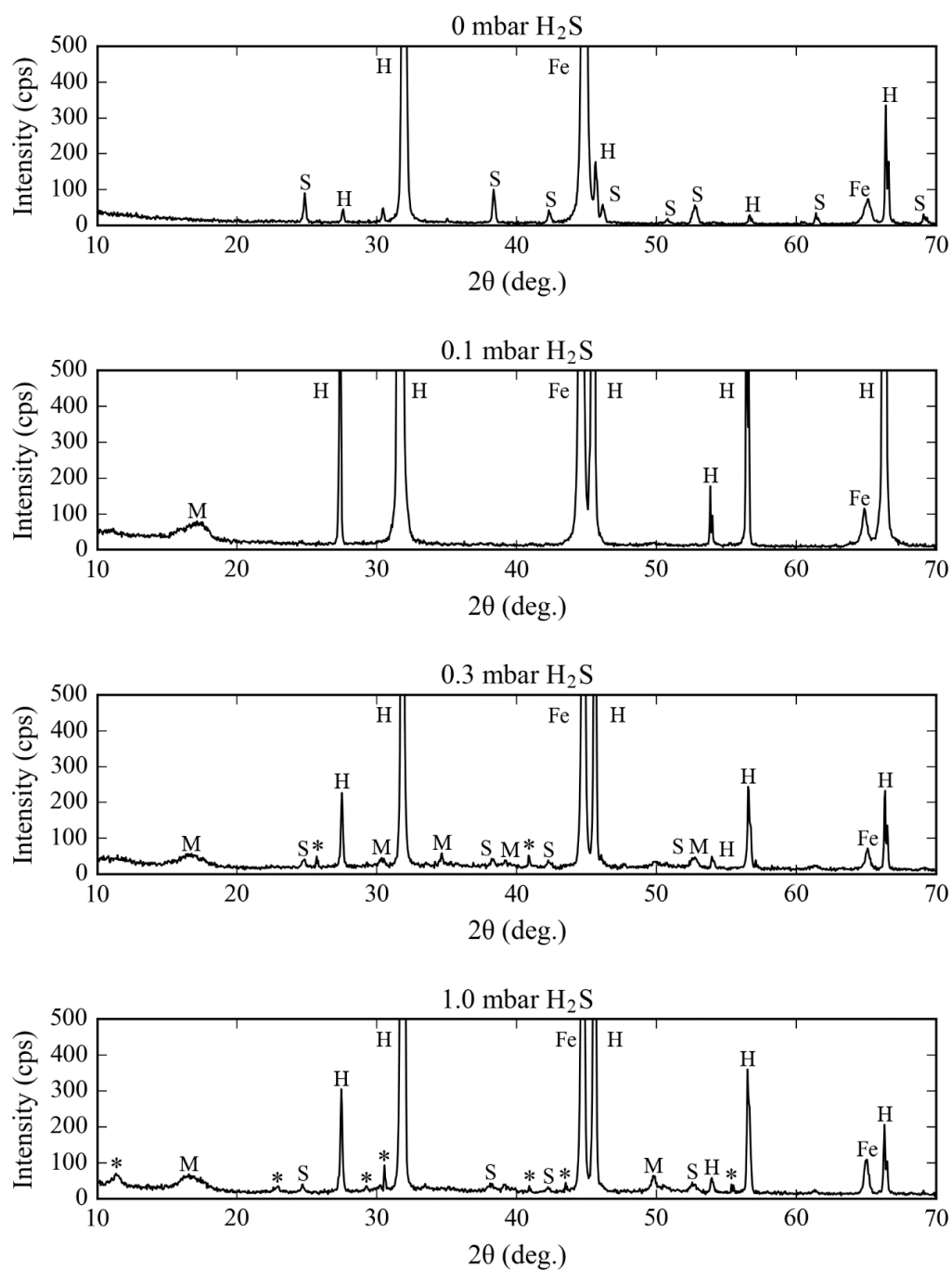


Figure 36: Effect of H_2S partial pressure on corrosion product composition. Phases are M: mackinawite, S: siderite, H: halite, and Fe: ferrite. Peaks labeled with an asterisk (*) correspond to unknown phases.

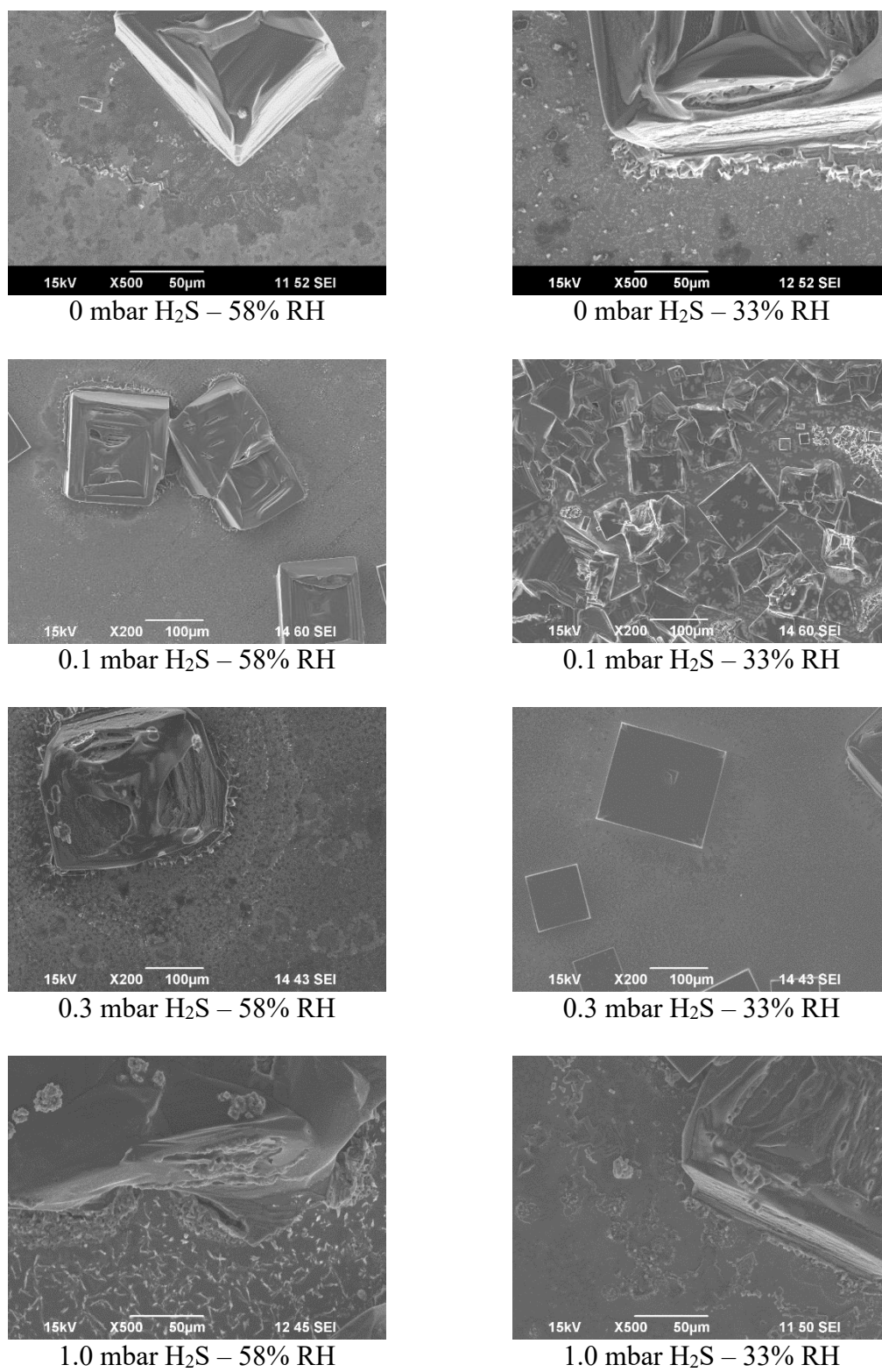


Figure 37: Effect of H_2S partial pressure on surface morphology at 58 and 33% RH.

The effect of H₂S partial pressure at relative humidities below the DRH on surface morphology is examined in Figure 37. Little to no corrosion is observable in the micrographs, however XRD detected the presence of mackinawite at 0.3 and 1.0 mbar H₂S at 58% RH as shown in Figure 38. As was the case in their 75% RH analogous experiments, the mackinawite peaks were very broad. No corrosion product was detected by XRD at 33% RH regardless of H₂S partial pressure.

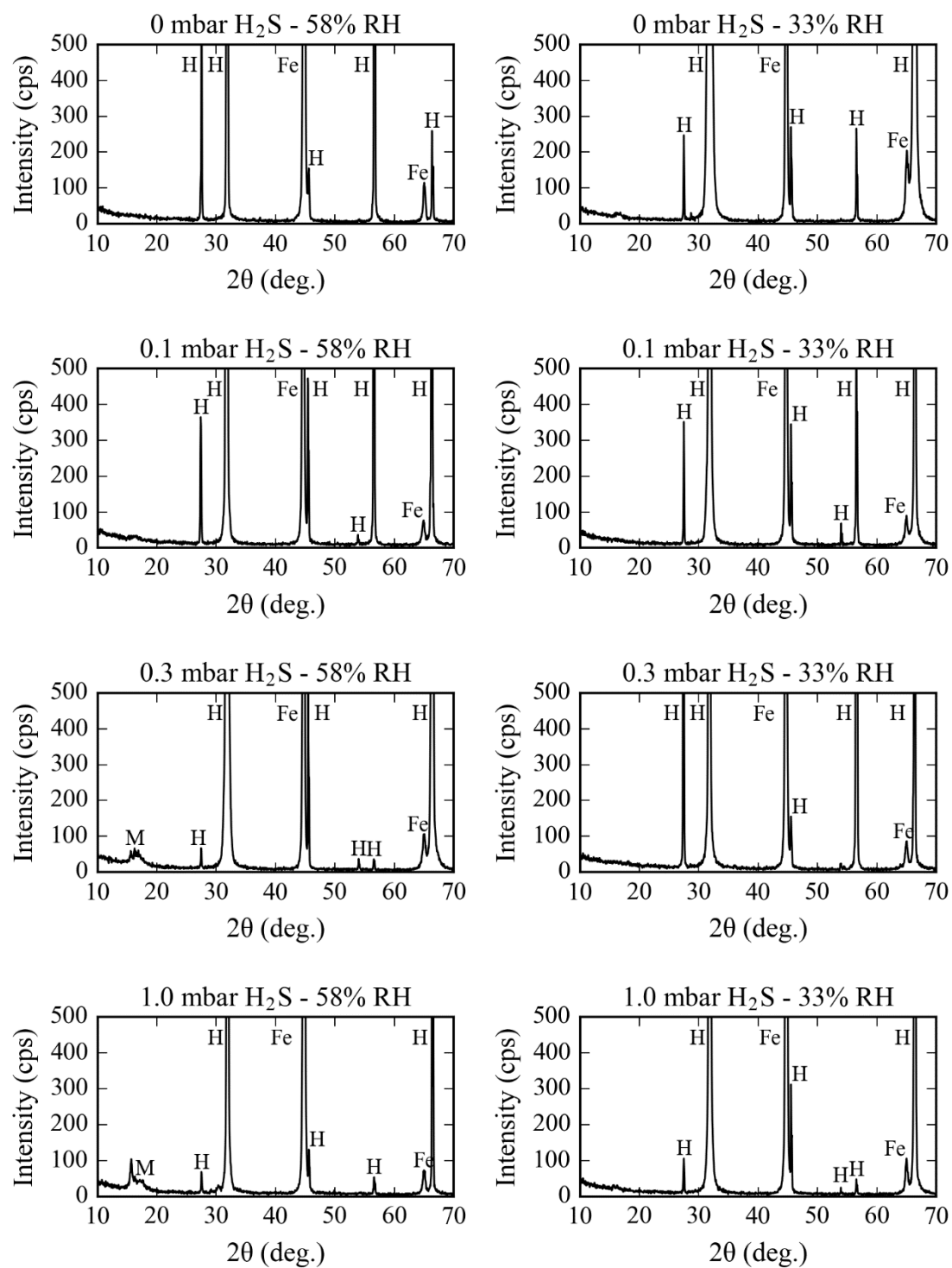


Figure 38: Effect of H_2S partial pressure on corrosion product composition. Phases are

M: mackinawite, H: halite, and Fe: ferrite.

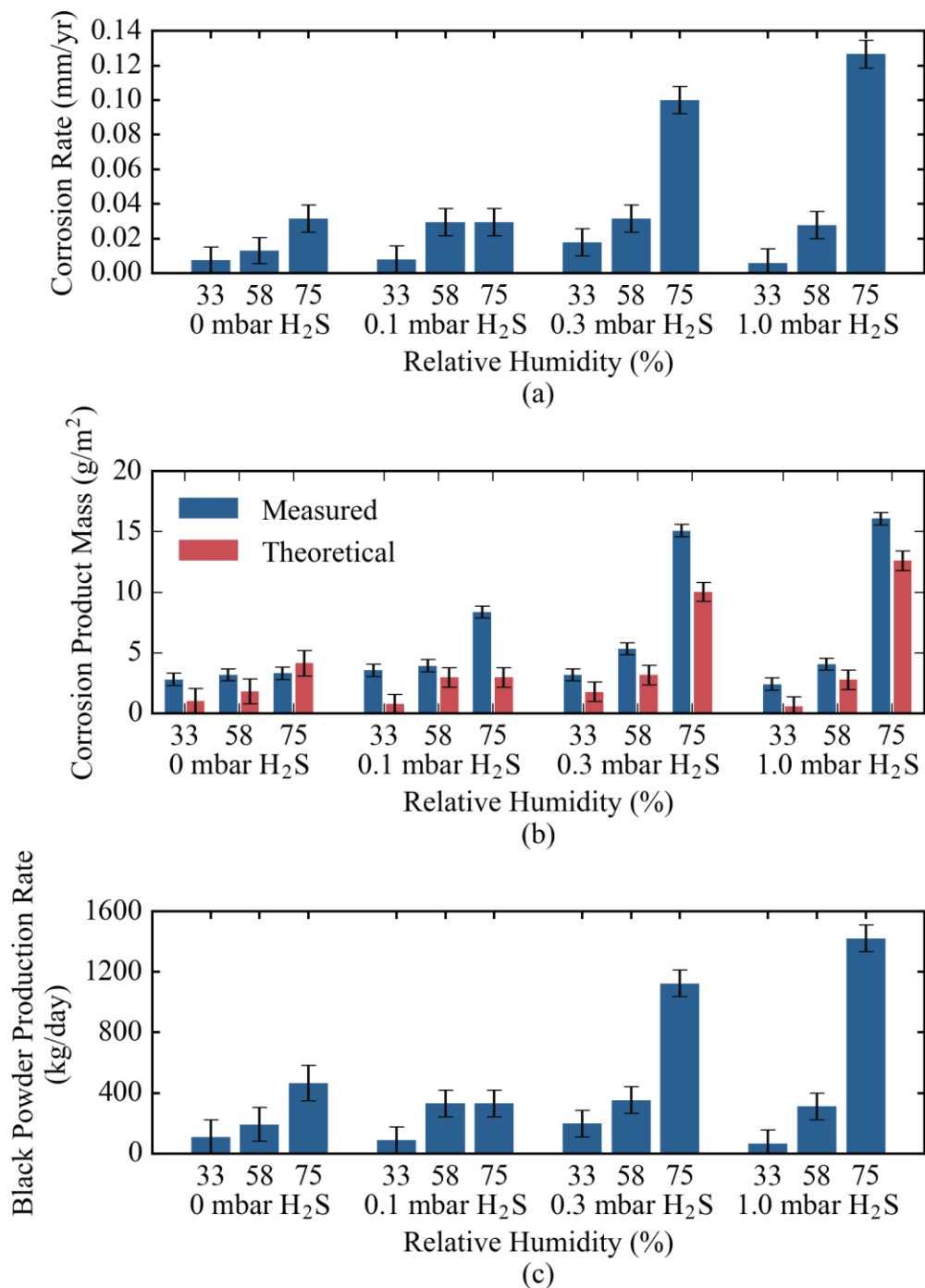


Figure 39: Effect of H₂S partial pressure on (a) general corrosion rate, (b) measured and theoretical corrosion product mass, and (c) maximum possible black powder production rate in a 100 km, 42 in. ID pipeline under hygroscopic conditions.

The effect of H₂S partial pressure on the general corrosion rate, corrosion product mass, and maximum possible black powder production rate is shown in Figure 39. At 0.3 and 1.0 mbar H₂S, the corrosion rates were close to those seen in dewing conditions, however, the corrosion rates saw a large drop as the RH fell below the deliquescence relative humidity (DRH) of NaCl (75% RH). Corrosion was measurable at 0.3 mbar H₂S and 33% RH, but the corrosion rates at 0, 0.1 and 1.0 mbar and 33% RH measured could not be distinguished from a corrosion rate of zero due to measurement uncertainties. The measured corrosion product mass was consistently higher than the theoretical mass, but this is likely due to the presence of NaCl in the measured corrosion product that was not quantified.

5.2.4 Corrosion Below the Deliquescence Relative Humidity

Based on the results above, it is apparent that corrosion occurred below the DRH, but corrosion products were most readily observed if deliquescence occurred. Schindelholz, *et al.*, [40] examined the effect of relative humidity on the corrosion of steel beneath NaCl particles in oxic environments. Corrosion below the DRH was attributed by Schindelholz, *et al.*, to adsorbed water on both the salt and the steel, deliquescence-efflorescence hysteresis, and changing chemistries due to corrosion.

The initiation of corrosion due to the hygroscopic salt particles was attributed to the presence of adsorbed water on both the salt and the steel surface and capillary condensation at the gas/salt/metal interface. Both the salt and the steel surface can adsorb water. NaCl has been shown to produce adsorbed water layers with properties similar to bulk water at a relative humidity of 40-50% [52]. Similarly, water adsorption on iron was

found to lead to a potentially corrosive water layer at about 50% RH [53]. The occurrence of corrosion at 33% RH in the oxic environments tested was attributed to the interaction of the two water layers on the salt and the steel through capillary condensation at the confined salt/steel interface [40].

Once initiated, the sustainment of corrosion is expected to be due to deliquescence-efflorescence hysteresis and the changing electrolyte chemistries as corrosion occurs. Deliquescence-efflorescence hysteresis is a depression in the efflorescence relative humidity relative to the deliquescence relative humidity and is typically caused by crystallization kinetics. In short, the driving force for crystallization at the DRH is frequently insufficient for nucleation and crystal growth, therefore a lower RH for efflorescence is necessary. However, the presence of corrosion products and metal surfaces can limit the effect of deliquescence-efflorescence hysteresis as heterogeneities may serve as nucleation sites [40], [54].

In the limited water available for corrosion to occur, a small amount of corrosion can significantly impact the water chemistry. The addition of ferrous ions to water can depress the effective DRH allowing corrosion to occur at even lower RH values than those necessary to initiate corrosion. The formation of other deliquescing phases such as $\text{FeCl}_2 \cdot 4\text{H}_2\text{O}$, which has a DRH of approximately 55% [55], may indeed allow for additional water accumulation. The presence of $\text{FeCl}_2 \cdot 4\text{H}_2\text{O}$ is reported to allow active corrosion of archaeological iron artifacts down to 20% RH and induce the “weeping” of the artifacts, whereby a highly acidic solution with high Fe^{2+} and Cl^- concentrations is formed as a result of exposure to a humid atmosphere [56], [57]. The formation of

additional species leading to locally decreased RH values is potentially important for black powder production through hygroscopic corrosion processes as pipeline conditions are not static. Corrosion beneath a salt crystal present on the steel surface may initiate while gas conditions are relatively humid, but the change in chemistry and deliquescence-efflorescence hysteresis could sustain deliquesced water even if bulk gas RH is decreased.

5.2.5 *Black Powder Formation through Hygroscopic Corrosion Processes*

For black powder to form *via* corrosion at RH values below 100%, the species on the surface must assist in the accumulation of moisture. NaCl deposits on the steel surface were found to lead to corrosion and corrosion product formation at relative humidities as low as 33%, however, corrosion products that can potentially lead to black powder were only found after 3 days if the salt was able to deliquesce.

From an engineering standpoint, the formation of friable corrosion products at deliquescence makes black powder prediction computationally simpler. Rather than trying to predict the corrosion due to adsorbed water layers on salt particles of variable size, one can assume full deliquescence is needed thereby allowing the thermodynamics of salt deliquescence in the particular system to be the deciding factor in the prediction of black powder formation. However, this still requires some knowledge of the composition of materials present on the steel surface. A sea salt residue will have a different DRH than a pure NaCl residue. Luckily, the thermodynamics of salt deliquescence is relatively well established due to its importance in atmospheric processes and food sciences.

The experiments discussed above do not necessarily negate the potential for black powder to form without the presence of a hygroscopic salt. Other materials such as glycols

or corrosion products may assist in the wetting of the steel surface and sustaining corrosion. Water accumulation leading to black powder may be facilitated by a corrosion product present upon a steel surface. A porous corrosion product may lead to water accumulation through capillary condensation. A liquid can spontaneously form in a nanoscopic pore at RH values much less than 100% due to increased intermolecular interactions within the confined space [38].

Glycols, especially triethylene glycol (TEG), are commonly used to dry natural gas to specification. Glycol carryover from gas processing plants can lead to corrosion and possibly black powder production through co-condensation of glycol and water and/or through the hygroscopic uptake of water by glycol. Deposited TEG/H₂O mixtures of >95% TEG in a 0.4 mbar H₂S/CO₂ (1 bar total pressure) atmosphere were found to sustain corrosion rates of 0.6 – 30 µm/year [58]. For reference, a 1 µm/yr general corrosion rate over a 100 km, 42 in. ID pipeline would yield a maximum possible black powder production rate of approximately 10 kg/day. Mixtures of TEG with black powder and other residual components will result in a black sludge, which requires pigging for it to be removed [59]. If this sludge is present within the pipeline or glycol carryover is suspected, then a thorough cleaning with methanol or another solvent is recommended before inhibitor application.

5.3 Experiment Repeatability

Great care was taken to ensure consistency in laboratory practices so that repeatable results were obtained, but the results herein are generally from one experiment per set of conditions. The complexity of each experiment, and particularly the encountered

difficulties with H₂S environments, limited the number of experiments that could be conducted for corrosion rate and corrosion product mass measurements. However, the features observed in the above microscopy were consistent with those seen in experiments with inconclusive gravimetric measurements though otherwise fine. SEM images from those tests and additional locations in the specimens shown above are shown in Appendix C.

CHAPTER 6: CONCLUSIONS AND FUTURE WORK

6.1 Summary of Results

Under dewing conditions, the two corrosion product morphologies were identified which can lead to black powder production. The first is formed due to corrosion product precipitation into a dual-layered morphology. The second is a result of the formation of mackinawite films that buckle and spall due to compressive stress generation due to layer growth.

Potential was found for black powder to form through hygroscopic corrosion if deliquescence occurs. Without deliquescence the corrosion product was minimal due to a decreased opportunity for corrosion to occur.

6.2 Hypotheses Revisited

The hypotheses formulated at the start of this study are revisited here in light of the results shown above.

- Pipeline conditions define what thermodynamically stable corrosion products will form on the steel surface although kinetically favored compounds will also be encountered.

The composition of the corrosion product did indeed change with the differing conditions tested. Mackinawite was the predominant phase detected under sour conditions, iron carbonate was found under sweet conditions, and a mix of iron carbonate and hematite was found under oxic conditions. Also, a mixture of thermodynamically-favored species and kinetically-favored species was also obtained. Mackinawite is a kinetically favored phase as compared to the more thermodynamically favored pyrite. The preference for

mackinawite is likely due to the temperatures being too low for meaningful phase transformation during the timeframe of an experiment.

With regards to black powder formation, the corrosion product composition seemed to have some effect on the propensity of the layer to spall. Buckling was readily observed in sour conditions, and loose layers were found in the oxic environments. However, corrosion products which form through a precipitation-only mechanism did not seem to be so readily removed compared to mackinawite, which forms through a combination of a direct reaction with the steel and precipitation. Precipitation directly onto the steel surface appeared to have developed a much more adherent corrosion product layer than the mackinawite formed under H₂S conditions.

- The formation of corrosion products follows a cyclical pattern that correlates with the wet/dry cycle caused by external temperature fluctuations.
- The cyclic behavior of water condensation and evaporation in sales gas pipelines prevents corrosion from reaching steady-state resulting in the formation of a kinetically favored, and potentially friable, corrosion product susceptible to spallation and entrainment in the bulk gas.

Corrosion and subsequent corrosion product formation did indeed seem to have correlated with the wet/dry cycle based on the 50% reduction in corrosion rate after 3 days in a temperature cycled condition compared to the 3 days, constant WCR experiment, but the cyclic water condensation seemed to have an opposite effect than hypothesized on the development of friable corrosion product layers. Less buckling was observed in the cycled

conditions than the constant temperature due to corrosion product precipitation upon dehydration reinforcing preexisting corrosion product layers.

- Corrosion products will form on the steel surface in non-water saturated sales gas pipelines if a hygroscopic material is present on the steel surface.

The development of corrosion products did indeed occur under non-water saturated conditions due to the presence of hygroscopic salts on the steel surface. Corrosion products were more prominent, however, when the deliquescence occurred.

6.3 Comments on Black Powder Mitigation

Black powder mitigation efforts should emphasize proper gas dehydration as the primary means of black powder mitigation. However, periodic upsets may allow water to condense despite best efforts in dehydration. As a means of insurance against black powder formation if liquid water was to condense, the use of corrosion inhibitors, particularly volatile corrosion inhibitors (VCIs), should minimize the effects of corrosion and therefore limit the production of resulting black powder. Finding an appropriate VCI to mitigate corrosion should become a priority for future black powder research.

6.4 Future Work

Suggested research topics to extend this work are as follows:

- Characterization of the mechanical properties of corrosion products formed under dewing conditions.
- Determining the role of iron sulfide growth mechanisms (*i.e.*, epitaxial growth, precipitation) on stress generation and layer failure.
- Black powder mitigation through volatile corrosion inhibitors

- Model development for the prediction of black powder formation.

REFERENCES

- [1] “International Energy Outlook 2016,” U.S. Energy Information Administration, Washington, D.C., 2016.
- [2] U.S. Energy Information Administration, *How much carbon dioxide is produced per kilowatt-hour when generating electricity with fossil fuels?* [Online]. Available: <http://www.eia.gov/tools/faqs/faq.cfm?id=74&t=11>. [Accessed: 13-Nov-2016].
- [3] Energy Information Administration, *About U.S. Natural Gas Pipelines - Transporting Natural Gas* [Online]. Available: https://www.eia.gov/pub/oil_gas/natural_gas/analysis_publications/ngpipeline/index.html. [Accessed: 02-Jun-2016].
- [4] R. Baldwin, “Black Powder in the Gas Industry - Sources, Characteristics and Treatment,” Mechanical and Fluids Engineering Division Southwest Research Institute, San Antonio, TA 97-4, 1997.
- [5] T. S. Khan and M. S. Al-Shehhi, “Review of black powder in gas pipelines – An industrial perspective,” *J. Nat. Gas Sci. Eng.*, vol. 25, pp. 66–76, Jul. 2015.
- [6] J. Smart, “Black Powder Movement in Gas Pipelines,” in *CORROSION/2011*, Houston, TX: NACE International, 2011, Paper No. 11089.
- [7] S. Mokhatab, W. A. Poe, and G. Zatzman, *Handbook of natural gas transmission and processing*, Second edition. Amsterdam: Gulf Professional Publishing, 2012.
- [8] A. M. Sherik, S. R. Zaidi, E. V. Tuzan, and J. P. Perez, “Black powder in gas transmission systems,” in *CORROSION/2008*, Houston, TX, 2008, Paper No. 08415.
- [9] T. Tran, B. Brown, and S. Netic, “Corrosion of Mild Steel in an Aqueous CO₂ Environment—Basic Electrochemical Mechanisms Revisited,” in *CORROSION/2015*, Houston, TX, 2015, Paper No. 5671.
- [10] M. Nordsveen, S. Netic, R. Nyborg, and A. Stangeland, “A Mechanistic Model for Carbon Dioxide Corrosion of Mild Steel in the Presence of Protective Iron Carbonate Films—Part 1: Theory and Verification,” *Corrosion*, vol. 59, no. 5, pp. 443–456, 2003.
- [11] J. Oddo and M. Tomson, “Simplified Calculation of CaCO₃ Saturation at High temperatures and Pressures in Brine Solutions,” *J. Pet. Technol.*, vol. 34, no. 7, pp. 1583–1590, 1982.

- [12] D. A. Palmer and R. Van Eldik, "The chemistry of metal carbonate and carbon dioxide complexes," *Chem. Rev.*, vol. 83, no. 6, pp. 651–731, 1983.
- [13] O. M. Suleimenov and R. E. Krupp, "Solubility of Hydrogen Sulfide in Pure Water and in NaCl Solutions, from 20 to 320°C and at Saturation Pressures," *Geochim. Cosmochim. Acta*, vol. 58, no. 11, pp. 2433–2444, 1994.
- [14] O. M. Suleimenov and T. . Seward, "A Spectrophotometric study of hydrogen sulphide ionisation in aqueous solutions to 350°C," *Geochim. Cosmochim. Acta*, vol. 61, no. 24, pp. 5187–5198, 1997.
- [15] Y. Kharaka, W. Gunter, P. Aggarwal, E. Perkins, and J. Dedraal, "SOLMINEQ.88: A Computer Program for Geochemical Modeling of Water-Rock Interactions," U.S. Geological Survey, Alberta Research Council, Menlo Park, CA, 88–4227, 1988.
- [16] W. Sun, S. Nešić, and R. C. Woollam, "The effect of temperature and ionic strength on iron carbonate (FeCO₃) solubility limit," *Corros. Sci.*, vol. 51, no. 6, pp. 1273–1276, Jun. 2009.
- [17] L. G. Benning, R. T. Wilkin, and H. . Barnes, "Reaction pathways in the Fe–S system below 100°C," *Chem. Geol.*, vol. 167, no. 1–2, pp. 25–51, Jun. 2000.
- [18] W. Sun and S. Nešić, "Kinetics of Corrosion Layer Formation: Part 1—Iron Carbonate Layers in Carbon Dioxide Corrosion," *CORROSION*, vol. 64, no. 4, pp. 334–346, Apr. 2008.
- [19] S. Nesic, Y. Zheng, B. Brown, and J. Ning, "Advancement in Predictive Modeling of Mild Steel Corrosion in CO₂ and H₂S Containing Environments," in *CORROSION/2015*, Houston, TX, 2015, Paper No. 6146.
- [20] W. Sun and S. Nešić, "A mechanistic model of uniform hydrogen sulfide/carbon dioxide corrosion of mild steel," *Corrosion*, vol. 65, no. 5, pp. 291–307, 2009.
- [21] Y. Zheng, J. Ning, B. Brown, D. Young, and S. Nesic, "Mechanistic Study of the Effect of Iron Sulfide Layers on Hydrogen Sulfide Corrosion of Carbon Steel," in *CORROSION/2015*, Houston, TX, 2015, Paper No. 5933.
- [22] D. W. Shoesmith, P. Taylor, M. G. Bailey, and D. G. Owen, "The Formation of Ferrous Monosulfide Polymorphs during the Corrosion of Iron by Aqueous Hydrogen Sulfide at 21°C," *J. Electrochem. Soc.*, vol. 127, no. 5, pp. 1007–1015, May 1980.
- [23] J. Boivin and S. Oliphant, "Sulfur Corrosion Due to Oxygen Ingress," in *CORROSION/2011*, Houston, TX, 2011, Paper No. 11120.

- [24] A. Sherik, "Black Powder in Gas Transmission Pipelines," in *Oil and Gas Pipelines*, R. W. Revie, Ed. John Wiley & Sons, Inc., 2015, pp. 423–436.
- [25] M. G. Fontana, *Corrosion Engineering*, 3rd ed. New York, NY: McGraw-Hill Education, 1986.
- [26] R. M. Cornell and U. Schwertmann, *The iron oxides: structure, properties, reactions, occurrences, and uses*, 2nd ed. Weinheim: Wiley-VCH, 2003.
- [27] B. Lavina *et al.*, "Structure of siderite FeCO₃ to 56 GPa and hysteresis of its spin-pairing transition," *Phys. Rev. B*, vol. 82, no. 6, Aug. 2010.
- [28] A. R. Lennie, S. A. T. Redfern, P. F. Schofield, and D. J. Vaughan, "Synthesis and Rietveld crystal structure refinement of mackinawite, tetragonal FeS," *Mineral. Mag.*, vol. 59, no. 397, pp. 677–684, 1995.
- [29] D. Rickard and G. W. Luther, "Chemistry of Iron Sulfides," *Chem. Rev.*, vol. 107, no. 2, pp. 514–562, Feb. 2007.
- [30] J. Yamada, H. Kaneta, and K. Nakayama, "Analysis of Black Powder in Natural Gas Pipelines," in *CORROSION/2011*, Houston, TX, 2011, Paper No. 11088.
- [31] J.-A. Bourdoiseau, M. Jeannin, R. Sabot, C. Rémazeilles, and P. Refait, "Characterisation of mackinawite by Raman spectroscopy: Effects of crystallisation, drying and oxidation," *Corros. Sci.*, vol. 50, no. 11, pp. 3247–3255, Nov. 2008.
- [32] B. Craig, "Corrosion Product Analysis - A Road Map to Corrosion in Oil and Gas Production," *Mater. Perform.*, vol. 41, no. 8, pp. 56–58, 2002.
- [33] Y. Tamaura, K. Ito, and T. Katsura, "Transformation of γ -FeO(OH) to Fe₃O₄ by adsorption of iron(II) ion on γ -FeO(OH)," *J. Chem. Soc. Dalton Trans.*, no. 2, pp. 189–194, Jan. 1983.
- [34] N. Yaakob, "Top of the Line Corrosion in CO₂/H₂S Environments," Ph.D. dissertation, Dept. Chem. Eng., Ohio Univ., Athens, OH, 2015.
- [35] S. Olsen and A. Dugstad, "Corrosion Under Dewing Conditions," in *CORROSION/1991*, Cincinnati, OH, 1991, Paper No. 472.
- [36] Z. Zhang, D. Hinkson, M. Singer, H. Wang, and S. Nešić, "A mechanistic model of top-of-the-line corrosion," *Corrosion*, vol. 63, no. 11, pp. 1051–1062, 2007.

- [37] N. Yaakob, F. Farelas, M. Singer, S. Nestic, and D. Young, "Localized Top of the Line Corrosion in Marginally Sour Environments," in CORROSION/2016, Houston, TX, 2016, Paper No. 7695.
- [38] E. Schindelholz and R. G. Kelly, "Wetting phenomena and time of wetness in atmospheric corrosion: a review," *Corros. Rev.*, vol. 30, no. 5–6, Jan. 2012.
- [39] L. Ojha *et al.*, "Spectral evidence for hydrated salts in recurring slope lineae on Mars," *Nat. Geosci.*, vol. 8, no. 11, pp. 829–832, Sep. 2015.
- [40] E. Schindelholz, B. E. Risteen, and R. G. Kelly, "Effect of Relative Humidity on Corrosion of Steel under Sea Salt Aerosol Proxies I. NaCl," *J. Electrochem. Soc.*, vol. 161, no. 10, pp. C450–C459, 2014.
- [41] J. Kolts, "Design for Internal Corrosion Resistance of Sales Gas Pipelines," presented at EUROCORR, Nice, France, 2004.
- [42] W. Litke, J. Bojes, P. Blais, J. Lerbscher, and W. Wamburi, "Aggressive Corrosion Associated with Salt Deposits in Low Water Content Sour Gas Pipelines," in CORROSION/2013, Houston, TX, 2013, Paper No. 2339.
- [43] "Standard Practice for Preparing, Cleaning and Evaluating Corrosion Test Specimens," ASTM Standard G1-03, 2011.
- [44] R. E. Bedworth and N. B. Pilling, "The Oxidation of Metals at High Temperatures," *J. Inst. Met.*, vol. 29, no. 3, pp. 529–582, 1923.
- [45] N. Birks, G. H. Meier, and F. S. Pettit, *Introduction to the High Temperature Oxidation of Metals, Second Edition*, 2nd ed. Cambridge University Press, 2006.
- [46] K. P. Lillerud and P. Kofstad, "On High Temperature Oxidation of Chromium I. Oxidation of Annealed, Thermally Etched Chromium at 800°–1100°C," *J. Electrochem. Soc.*, vol. 127, no. 11, pp. 2397–2410, Nov. 1980.
- [47] P. Kofstad and K. P. Lillerud, "On High Temperature Oxidation of Chromium II. Properties of and the Oxidation Mechanism of Chromium," *J. Electrochem. Soc.*, vol. 127, no. 11, pp. 2410–2419, Nov. 1980.
- [48] F. A. Golightly, F. H. Stott, and G. C. Wood, "The Relationship Between Oxide Grain Morphology and Growth Mechanisms for Fe-Cr-Al and Fe-Cr-Al-Y Alloys," *J. Electrochem. Soc.*, vol. 126, no. 6, pp. 1035–1042, Jun. 1979.
- [49] R. B. Bird, W. E. Stewart, and E. N. Lightfoot, *Transport phenomena*, Rev. 2. ed. New York: Wiley, 2007.

- [50] RRUFF, "Hematite X050102." [Online]. Available: https://rruff-2.geo.arizona.edu/m/rruff_id/desc/X050102. [Accessed: 26-Nov-2016].
- [51] M. E. Wise, S. T. Martin, L. M. Russell, and P. R. Buseck, "Water Uptake by NaCl Particles Prior to Deliquescence and the Phase Rule," *Aerosol Sci. Technol.*, vol. 42, no. 4, pp. 281–294, Mar. 2008.
- [52] M. C. Foster and G. E. Ewing, "Adsorption of water on the NaCl(001) surface. II. An infrared study at ambient temperatures," *J. Chem. Phys.*, vol. 112, no. 15, pp. 6817–6826, 2000.
- [53] S. Lee and R. W. Staehle, "Adsorption of Water on Copper, Nickel, and Iron," *CORROSION*, vol. 53, no. 1, pp. 33–42, Jan. 1997.
- [54] E. Schindelholz, L. Tsui, and R. G. Kelly, "Hygroscopic Particle Behavior Studied by Interdigitated Array Microelectrode Impedance Sensors," *J. Phys. Chem. A*, vol. 118, no. 1, pp. 167–177, Jan. 2014.
- [55] G. M. Richardson and R. S. Malthus, "Salts for static control of humidity at relatively low levels," *J. Appl. Chem.*, vol. 5, no. 10, pp. 557–567, Oct. 1955.
- [56] S. Turgoose, "Post-Excavation Changes in Iron Antiquities," *Stud. Conserv.*, vol. 27, no. 3, pp. 97–101, 1982.
- [57] L. S. Selwyn, P. I. Sirois, and V. Argyropoulos, "The corrosion of excavated archaeological iron with details on weeping and akaganéite," *Stud. Conserv.*, vol. 44, no. 4, pp. 217–232, Jan. 1999.
- [58] A. Dugstad and H. Sirnes, "Experimental Study of Black Powder in field TEG solutions," in *CORROSION/2011*, Houston, TX, 2011, Paper No. 11083.
- [59] A. M. Sherik, A. Rasheed, and A. Jabran, "Effect Of Sales Gas Pipelines Black Powder Sludge on the Corrosion of Carbon Steel," in *CORROSION/2011*, Houston, TX, 2011, Paper No. 11087.
- [60] E. O. Lebigot, *Uncertainties: a Python package for calculations with uncertainties*. Available: <https://pythonhosted.org/uncertainties/>

APPENDIX A: PELTIER TEMPERATURE CONTROLLER DESIGN

Specimen Temperature Controller Design

Dewing corrosion specimen temperature was performed with a specially designed control system. The system was built around a TC-48-20 PID (Proportional, Integral, Derivative) Peltier controller by TE Technology®. Key features of the controller include heating and cooling control modes, 2 thermistor inputs, a pulse-width modulated output, 2 temperature alarms, and a computer interface through serial RS-232 communications. The two alarms included in the controller monitor their respective thermistor input and activate if the temperature exceeds a user-defined value. If an alarm is triggered, then a transistor activates and allows electrical current to pass to ground completing a circuit. The alarms were designed for controlling fans or other loads. For instance, if a high temperature is measured on the Peltier heatsink by the secondary thermistor, then a fan on the heat sink will be activated allowing for better heat transfer.

A general schematic of the Peltier controller used for experimentation is shown in Figure 40. Specimen temperature is measured with the primary thermistor (10 k Ω at 25°C) held in contact with the specimen. The thermistor bulb is mounted through a hole in the PEEK specimen holder and held in place with hot glue. The hot glue acts as both support for the thermistor and as thermal insulation isolating the sensor from external influences. The PID controller computes the pulse-width modulation (PWM) duty cycle required to maintain the temperature setpoint which modulates the 12 VDC power supply voltage to supply the required power to the Peltier.

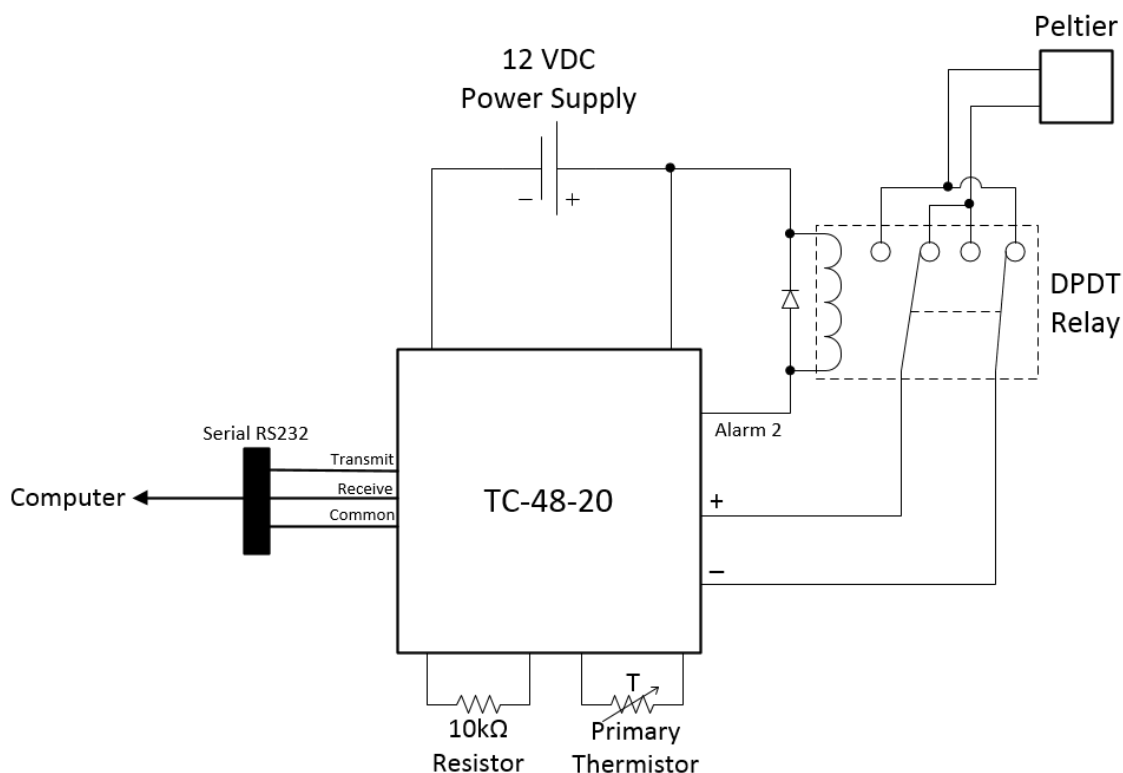


Figure 40: Peltier controller schematic.

A limitation of the TC-48-20 Peltier controller is that the positive and negative Peltier terminals are fixed preventing the polarity change required for temperature cycling experiments. To overcome this limitation, a double-pole-double-throw (DPDT) relay was installed between the controller and the Peltier in the configuration shown in Figure 40, above. Break-before-make contacts are required in the relay to prevent short circuits. A diode was placed in a reverse bias orientation to minimize the effects of voltage spikes due to a collapsing magnetic field in the relay's inductor. The relay is activated by triggering the secondary alarm which allows current to pass through the relay inductor thereby activating the relay. Since measurements are required to activate the alarm, the secondary

thermistor was replaced with a $10\text{k}\Omega$ resistor to measure a constant 25°C secondary temperature. By changing the secondary alarm temperature to above or below 25°C , then the alarm can be deactivated or activated, respectively.

Since the Peltier controller was to be used in an H_2S laboratory, the controller was housed in a sealed steel box which isolates the controller and potential sparks within the box from a potentially flammable environment. Panel mount connectors were installed in the box door to provide a connection from the controller to the Peltier, primary thermistor, and the computer kept outside the H_2S laboratory. The serial RS-232 connection and software included with the controller allowed for specimen temperature monitoring and temperature cycling without the need to enter the H_2S laboratory.

A secondary Peltier controller was developed based upon an Arduino Uno microcontroller. As the microcontroller cannot supply the electrical power to the Peltier, a MOSFET H-bridge motor driver (Pololu High-Power Motor Driver 18-25) was installed between the Peltier and the power supply for power modulation and Peltier polarity control. The Arduino controller acts in a similar manner as the TC-48-20 controller in that a PID algorithm computes the duty cycle for the PWM output. The AC output is passed to the MOSFET gates in the motor driver along with a binary signal which determines the polarity of the Peltier. Controller behavior was programmed in C/C++.

XRD Specimen Holder Design

Specimen size limitations in the X-ray diffractometer prevented the use of the large cylindrical specimens the dewing corrosion apparatus was designed around, so a new holder was developed to hold smaller specimens within a body close to the same size as

the cylindrical specimens. A cross-sectional view of the apparatus is shown in Figure 41. The specimen holder holds a $0.5 \times 0.5 \times 0.08$ inch³ ($12.7 \times 12.7 \times 2$ mm³) specimen within a square cutout in the center of an aluminum body with a 1.25-inch-diameter \times 0.625-inch-thick (31.7 mm \times 15.9 mm) cylindrical specimen. Aluminum was chosen for its thermal conductivity and corrosion resistance. The specimen was coated with Xylan to prevent galvanic effects between the aluminum and the steel. A magnet within a stainless steel part embedded within the aluminum holds the specimen to the holder. Threads in the aluminum body and the stainless steel part allow for specimen height adjustment. Lubrication was applied to the threads to prevent galling. A hole slightly offset from center was drilled to place a thermistor near the steel specimen for temperature control. The aluminum body was fitted into a PEEK sleeve designed to provide a seal with the stainless steel glass cell lid. O-rings were embedded within the body and PEEK sleeve to prevent gas leakage.

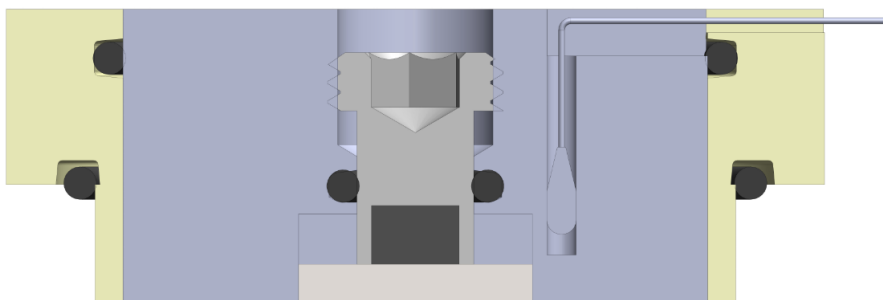


Figure 41: Cross-section view of the XRD specimen holder. Image courtesy of Cody

Shafer.

APPENDIX B: CALCULATIONS

Three primary specimen mass measurements were taken for each specimen: (1) initial mass, m_i (g); (2) post-extraction mass, m_e (g); and (3) mass after corrosion product removal, m_f (g). The procedures for calculating the general corrosion rate, measured specimen mass, and theoretical specimen mass from those measurements are detailed in the following sections.

Corrosion Rate

The corrosion rate is calculated with Equation 53:

$$CR = 365 \frac{m_i - m_f}{t \rho_{\text{steel}} A_s} \quad (53)$$

where:

CR = Corrosion rate (mm/yr)

t = Experiment duration (days)

ρ_{steel} = Steel density (kg/m³)

A_s = Wetted steel surface area (m²)

Measured Corrosion Product Mass

The measured corrosion product mass is the mass of corrosion product removed per unit area. The measured corrosion product mass, in g/m², is calculated with Equation 54:

$$m_{\text{meas}} = \frac{m_e - m_f}{A_s} \quad (54)$$

Theoretical Corrosion Product Mass

The theoretical corrosion product mass is less straightforward to calculate than the measured corrosion product mass. The theoretical corrosion product mass is the mass of corrosion product that would be produced based on the mass of steel lost due to corrosion. The X65 steel includes alloying elements (*i.e.*, C, Mn, Cu, Ni, etc.), so the measured corrosion product mass should account for these species. The steel components are grouped into three categories: iron, carbon, and other (which includes all other alloying elements). The mass lost due to corrosion in these three categories is calculated by multiplying the total mass lost due to corrosion by the mass fraction (x) of that category:

$$\Delta m = m_i - m_f \quad (55)$$

$$m_{\text{Fe}} = x_{\text{Fe}} \Delta m \quad (56)$$

$$m_{\text{C}} = x_{\text{C}} \Delta m \quad (57)$$

$$m_{\text{other}} = x_{\text{other}} \Delta m \quad (58)$$

Carbon within the steel is assumed to all be present as iron carbide (Fe_3C). Realistically, some carbon will be interstitially intercalated through the ferrite, however this mass is assumed to be small and therefore negligible. The mass of iron carbide is therefore determined by Equation 59. The mass of iron available for iron carbonate, iron sulfide, or iron oxide production is thereby the difference in the total mass of Fe and the mass of Fe within the iron carbide (Equation 60). M_i is the molar mass of species i .

$$m_{\text{Fe}_3\text{C}} = \frac{m_{\text{C}} M_{\text{Fe}_3\text{C}}}{M_{\text{C}}} \quad (59)$$

$$m_{\text{Fe,CP}} = m_{\text{Fe}} - 3 \frac{m_{\text{Fe}_3\text{C}} M_{\text{Fe}}}{M_{\text{Fe}_3\text{C}}} \quad (60)$$

The dominant corrosion product is ultimately dependent upon the conditions in which the corrosion product is developed. The corrosion product with identity j is assumed to be Fe_2O_3 in oxic environments, FeS in sour conditions, and FeCO_3 in sweet conditions. The mass of the iron corrosion product with n moles of Fe per mole j produced is calculated as follows:

$$m_j = \frac{m_{\text{Fe,CP}} M_j}{n M_{\text{Fe}}} \quad (61)$$

The total theoretical mass of corrosion product per unit area is calculated by summing the individual corrosion product components and dividing by the specimen area as in Equation 62.

$$m_{\text{theor}} = \frac{m_j + m_{\text{Fe}_3\text{C}} + m_{\text{other}}}{A_s} \quad (62)$$

Maximum Possible Black Powder Production Rate

The theoretical mass of corrosion product is extrapolated over a straight, 42 in. (1.07 m) ID, 100 km pipeline with area A_{pipe} for the experimental duration to determine the maximum possible black powder production rate, \dot{m}_{BP} .

$$\dot{m}_{\text{BP}} = \frac{m_{\text{theor}} A_{\text{pipe}}}{t} 10^{-3} \quad (63)$$

Error Analysis

Corrosion rate and corrosion product mass measurements are highly dependent upon gravimetric measurements. Mass measurements were all conducted on a Mettler Toledo AB204-S, which has a readability and repeatability (standard deviation) of 0.1 mg. The uncertainty in the mass measurement was propagated throughout the corrosion rate and corrosion product mass measurements with the assistance of the Python package

Uncertainties [60]. The Uncertainties package uses linear error propagation theory to calculate the standard deviation of a mathematical expression with inputs that include a probability distribution function. The calculated results were reported using a 95% confidence interval.

APPENDIX C: ADDITIONAL MICROSCOPY

Many more SEM images were taken than those shown in Chapter 5. The images selected for viewing in the main body of the text were selected based on how representative the micrograph is of the specimen at large and their content in relation to understanding black powder formation. Additional SEM surface microscopy is shown in this appendix for context. The micrographs are grouped by experiment condition and, unless specified otherwise, were taken after the specimen was extracted.

Dewing Corrosion

0 mbar H₂S – High WCR

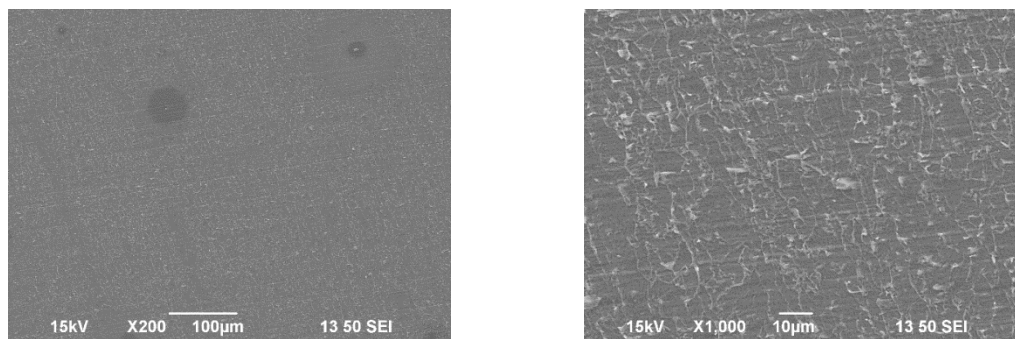


Figure 42: Conditions: p_{H₂S}: 0 mbar, p_{CO₂}: 0.96 bar, WCR: 0.05 ml/m²/s, Steel

Temperature: 15°C, Gas Temperature: 30°C, Duration: 3 days.

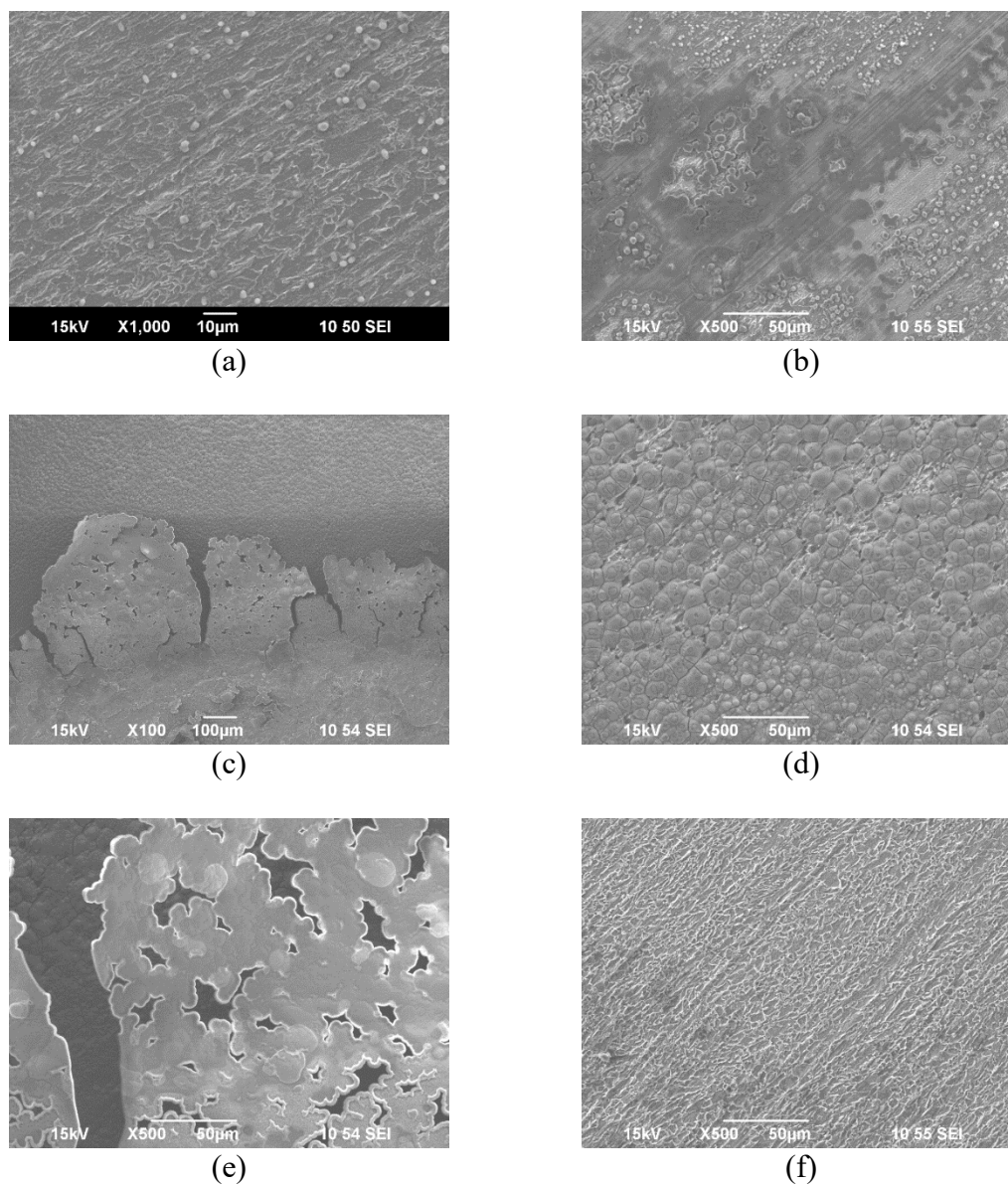
0 mbar H₂S – Low WCR

Figure 43: Conditions: p_{H₂S}: 0 mbar, p_{CO₂}: 0.96 bar, WCR: 0.015 ml/m²/s, Steel Temperature: 25°C, Gas Temperature: 30°C, Duration: 3 days. Images (a) and (b) were from the same test as that shown in Chapter 5, whereas images (c)-(f) were from a test

with inconclusive gravimetric measurements. The corrosion product in the inconclusive test was of a similar morphology to the CO₂/O₂ test.

0.1 mbar H₂S – High WCR

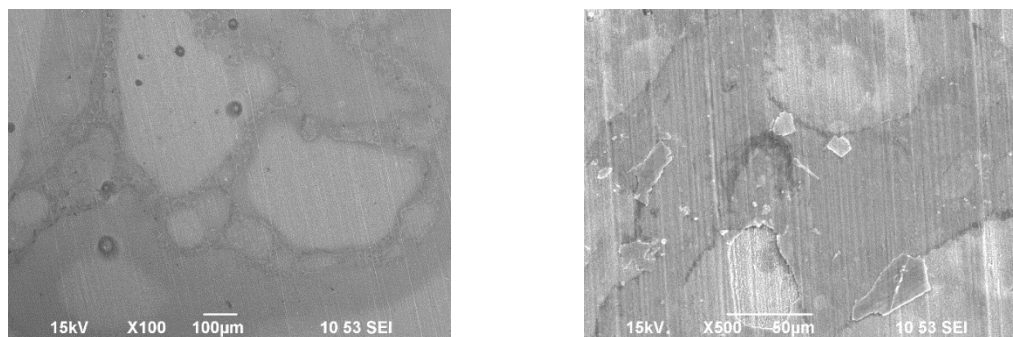


Figure 44: Conditions: pH₂S: 0.1 mbar, pCO₂: 0.96 bar, WCR: 0.05 ml/m²/s, Steel
Temperature: 15°C, Gas Temperature: 30°C, Duration: 3 days.

0.1 mbar H₂S – Low WCR

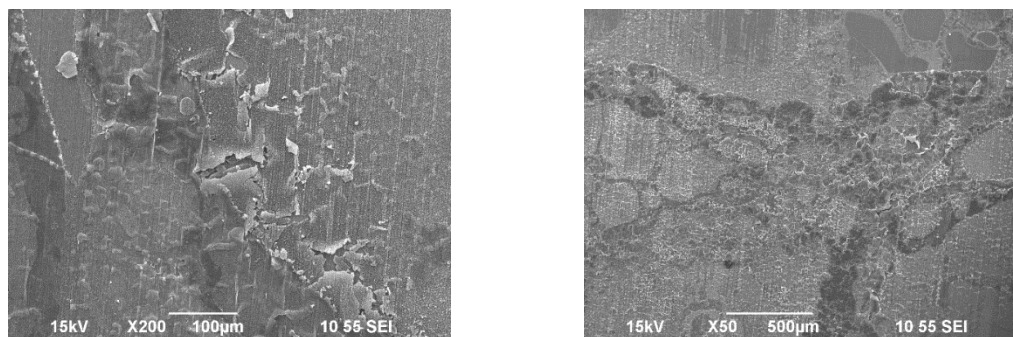


Figure 45: Conditions: pH₂S: 0.1 mbar, pCO₂: 0.96 bar, WCR: 0.015 ml/m²/s, Steel
Temperature: 25°C, Gas Temperature: 30°C, Duration: 3 days.

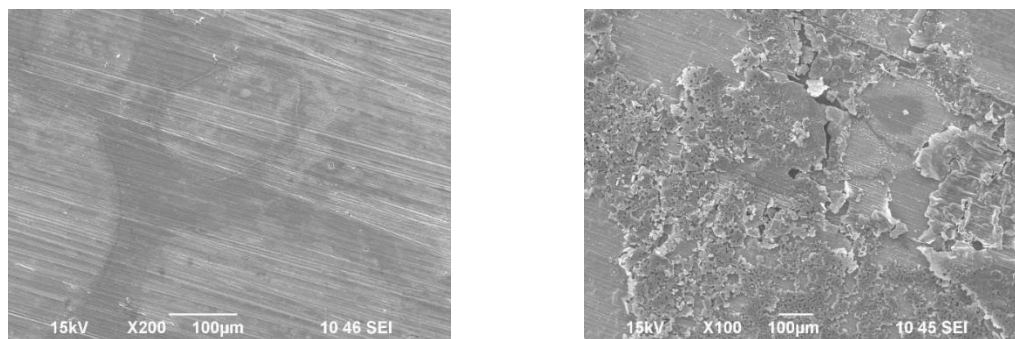
0.3 mbar H₂S – High WCR

Figure 46: Conditions: p_{H₂S}: 0.3 mbar, p_{CO₂}: 0.96 bar, WCR: 0.05 ml/m²/s, Steel
Temperature: 15°C, Gas Temperature: 30°C, Duration: 3 days.

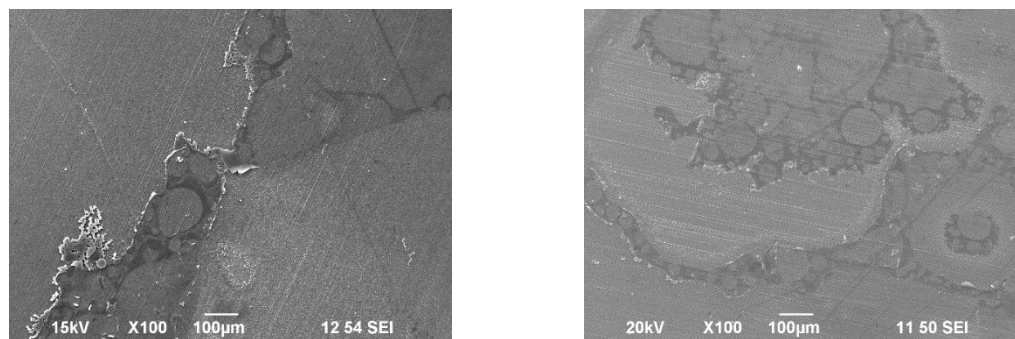
0.3 mbar H₂S – Low WCR – 6 hours

Figure 47: Conditions: p_{H₂S}: 0.3 mbar, p_{CO₂}: 0.96 bar, WCR: 0.015 ml/m²/s, Steel
Temperature: 25°C, Gas Temperature: 30°C, Duration: 6 hours.

0.3 mbar H₂S – Low WCR – 1 day

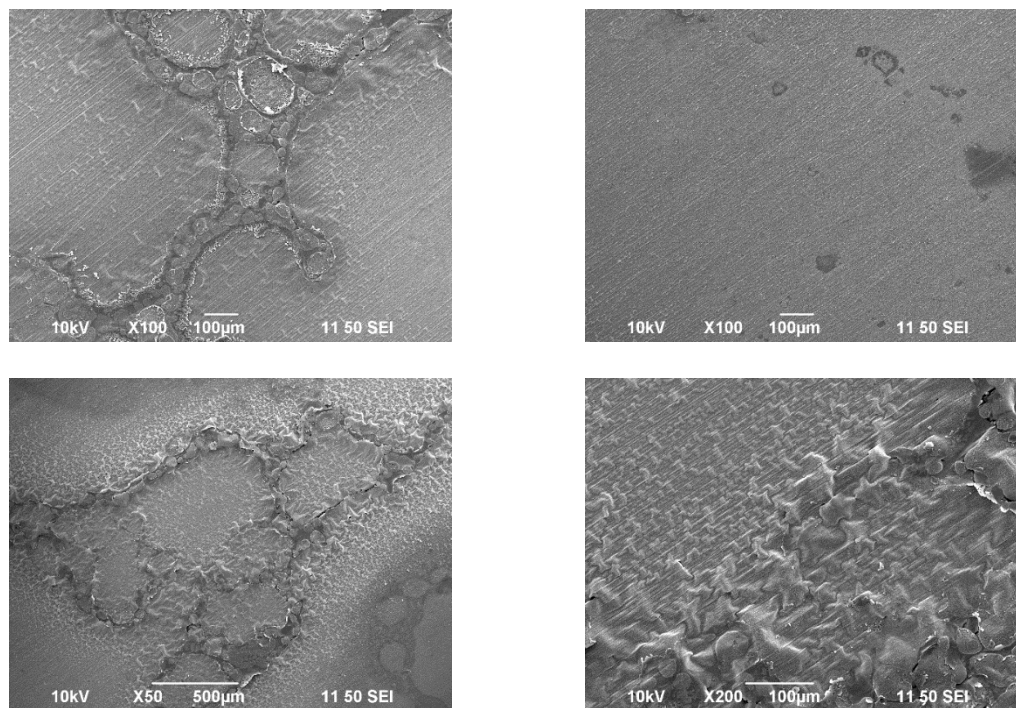


Figure 48: Conditions: pH₂S: 0.3 mbar, pCO₂: 0.96 bar, WCR: 0.015 ml/m²/s, Steel

Temperature: 25°C, Gas Temperature: 30°C, Duration: 1 day.

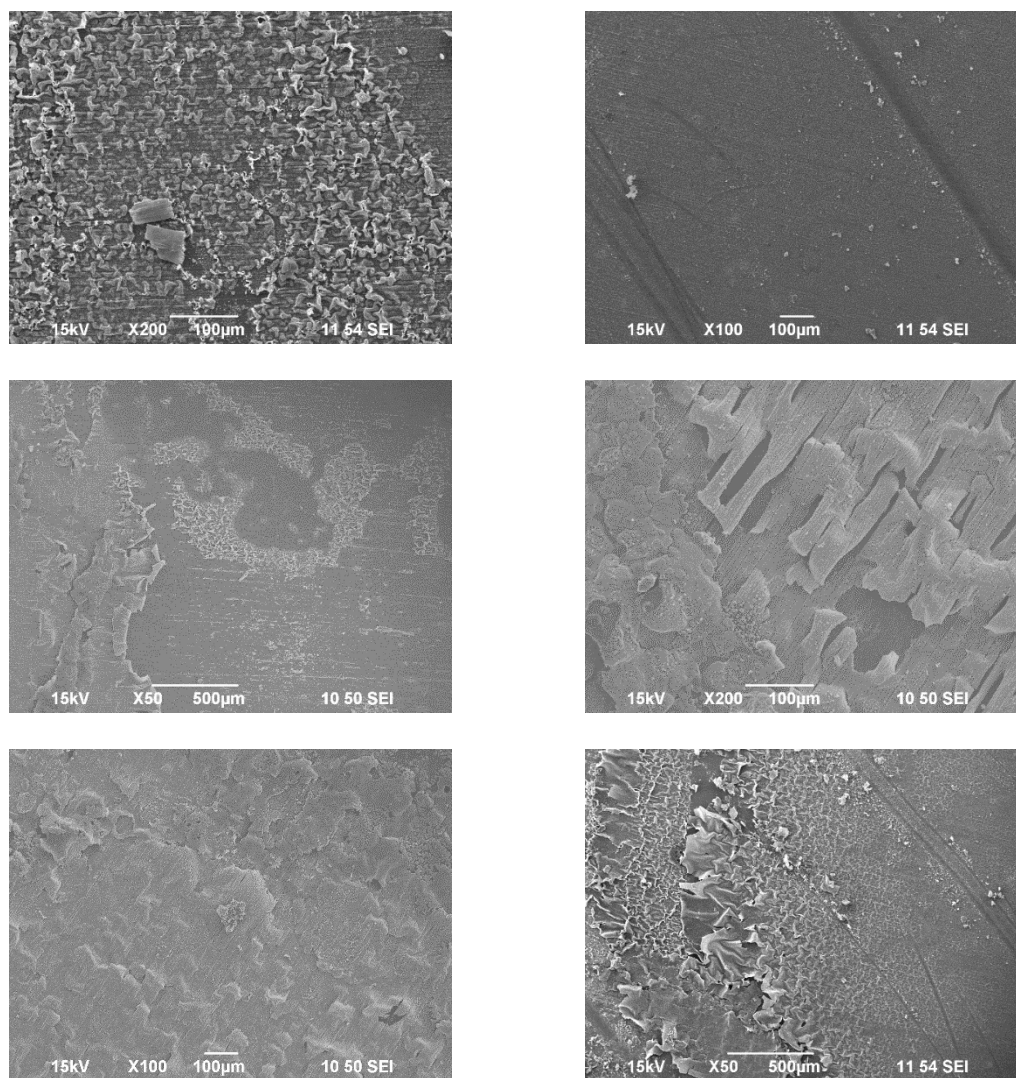
0.3 mbar H₂S – Low WCR – 3 days

Figure 49: Conditions: p_{H₂S}: 0.3 mbar, p_{CO₂}: 0.96 bar, WCR: 0.015 ml/m²/s, Steel

Temperature: 25°C, Gas Temperature: 30°C, Duration: 3 days.

0.3 mbar H₂S – Low WCR – 7 days

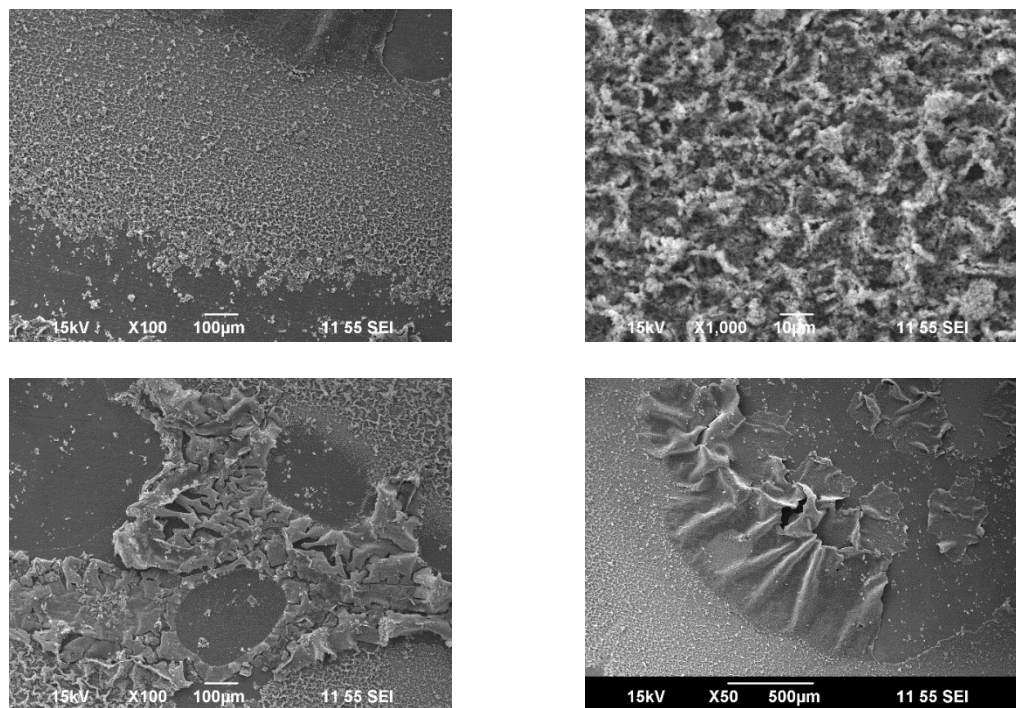


Figure 50: Conditions: pH₂S: 0.3 mbar, pCO₂: 0.96 bar, WCR: 0.015 ml/m²/s, Steel

Temperature: 25°C, Gas Temperature: 30°C, Duration: 7 days.

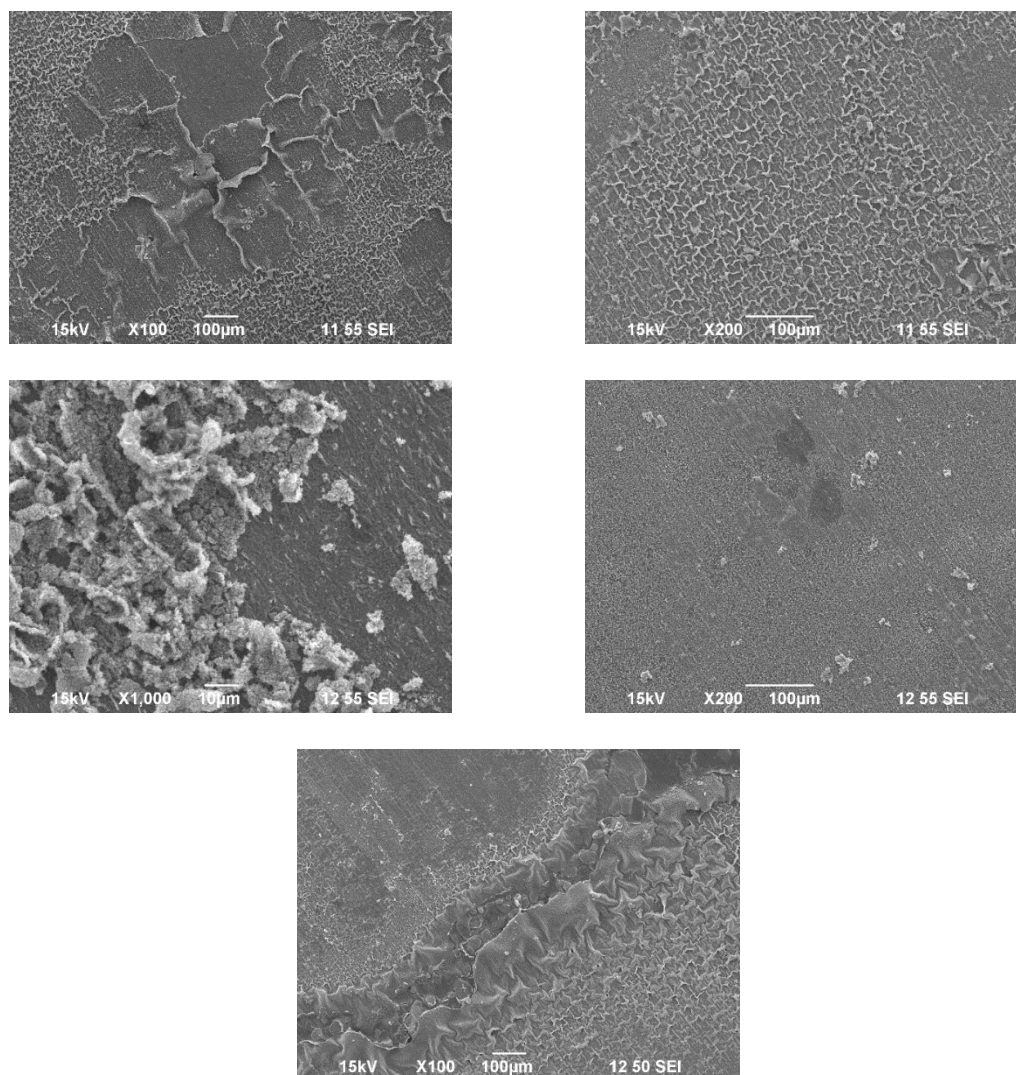
0.3 mbar H₂S – Low WCR – 10 days

Figure 51: Conditions: p_{H₂S}: 0.3 mbar, p_{CO₂}: 0.96 bar, WCR: 0.015 ml/m²/s, Steel
Temperature: 25°C, Gas Temperature: 30°C, Duration: 10 days.

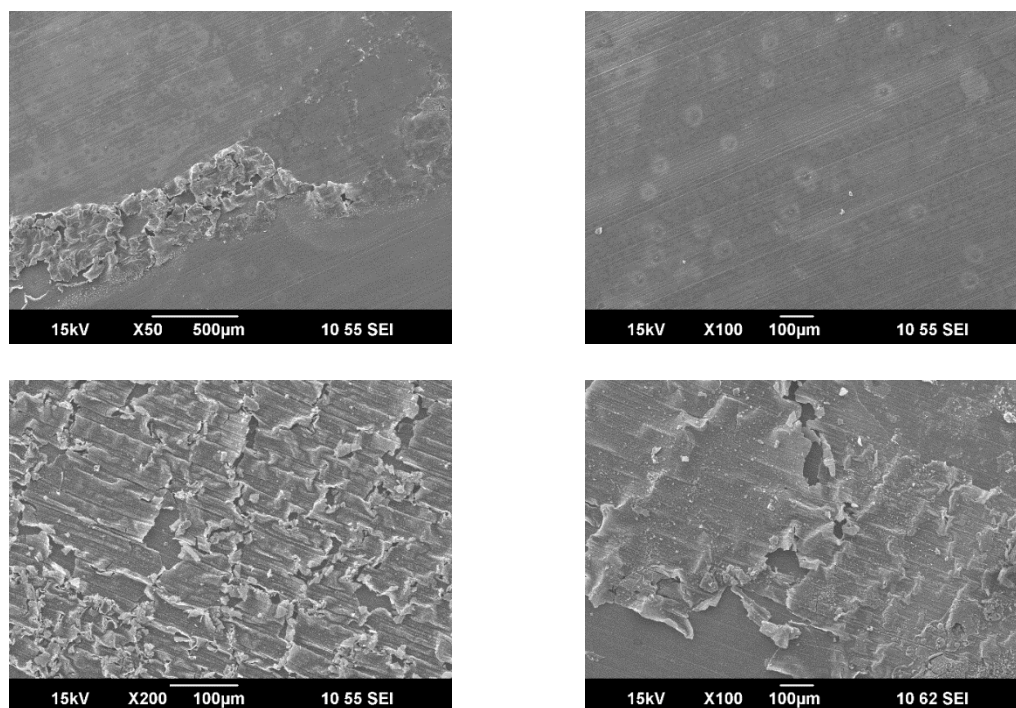
1.0 mbar H₂S – High WCR

Figure 52: Conditions: p_{H₂S}: 1.0 mbar, p_{CO₂}: 0.96 bar, WCR: 0.05 ml/m²/s, Steel

Temperature: 15°C, Gas Temperature: 30°C, Duration: 3 days.

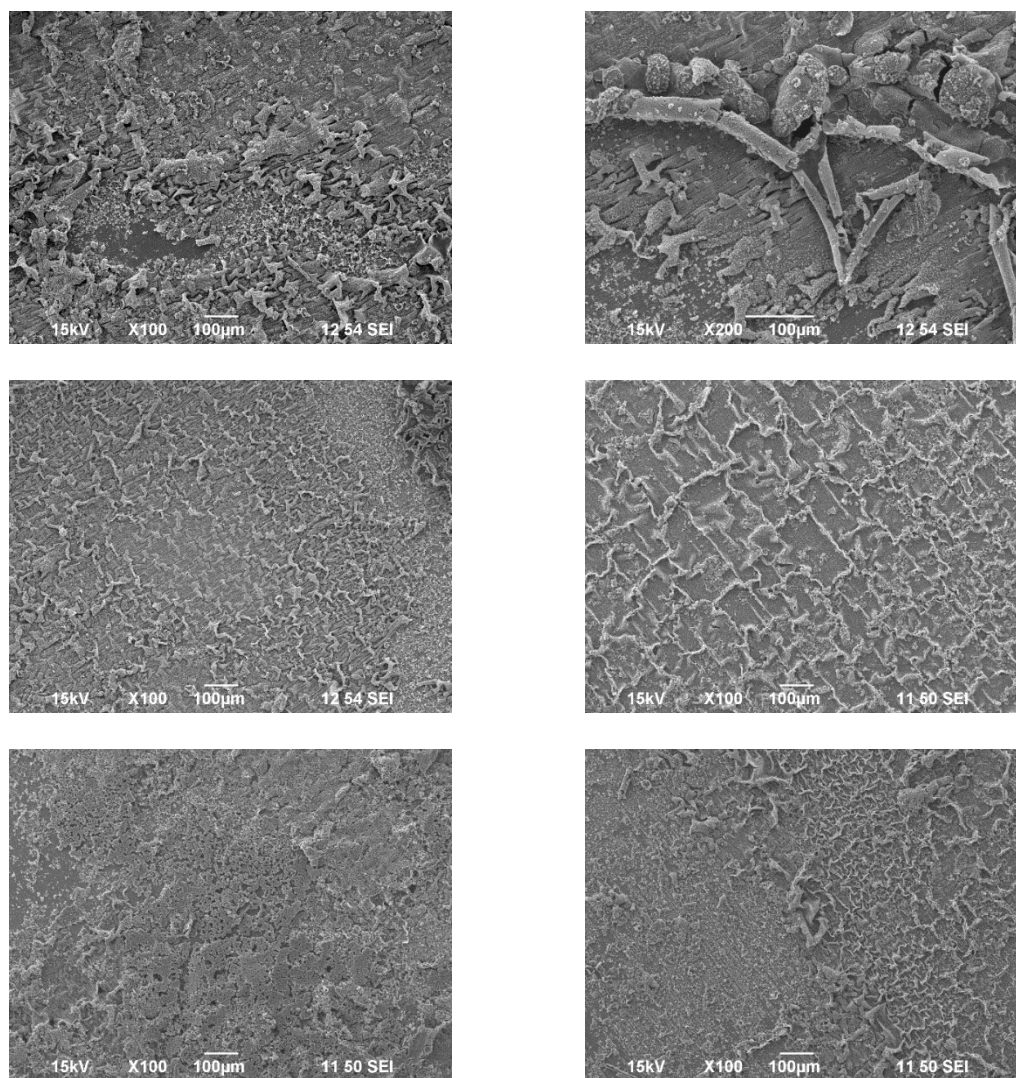
1.0 mbar H₂S – Low WCR

Figure 53: Conditions: p_{H₂S}: 1.0 mbar, p_{CO₂}: 0.96 bar, WCR: 0.015 ml/m²/s, Steel
Temperature: 25°C, Gas Temperature: 30°C, Duration: 3 days.

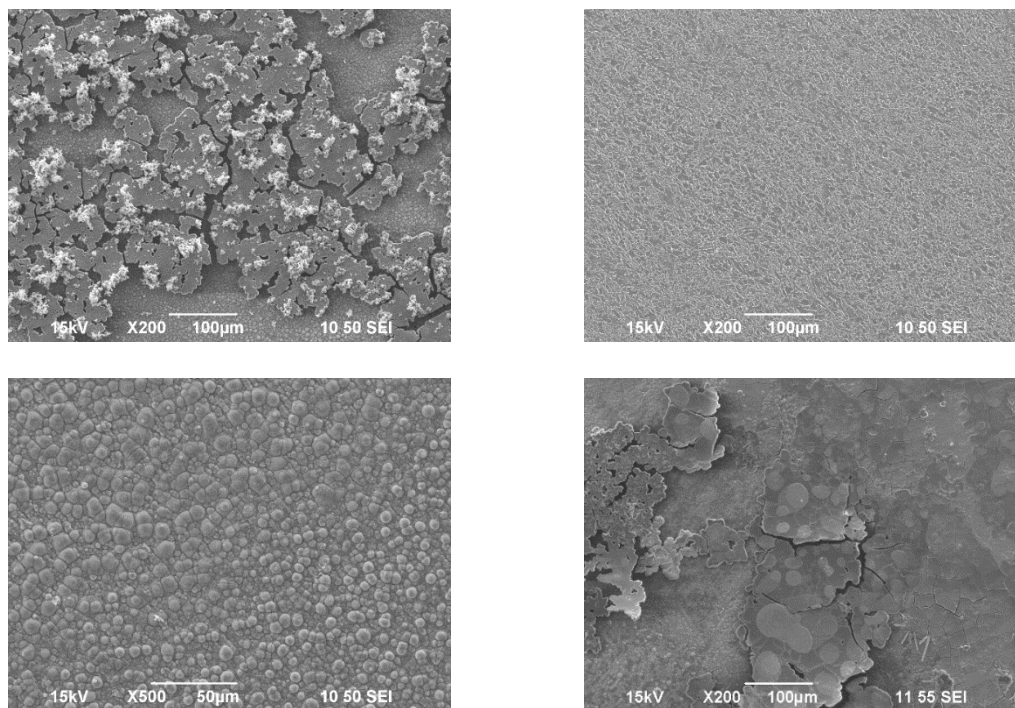
10 mbar O₂ – Low WCR – 3 days

Figure 54: Conditions: p_{H₂S}: 0.3 mbar, p_{CO₂}: 0.96 bar, WCR: 0.015 ml/m²/s, Steel

Temperature: 25°C, Gas Temperature: 30°C, Duration: 6 hours.

0.3 mbar H₂S – Temperature Cycling – 3 days

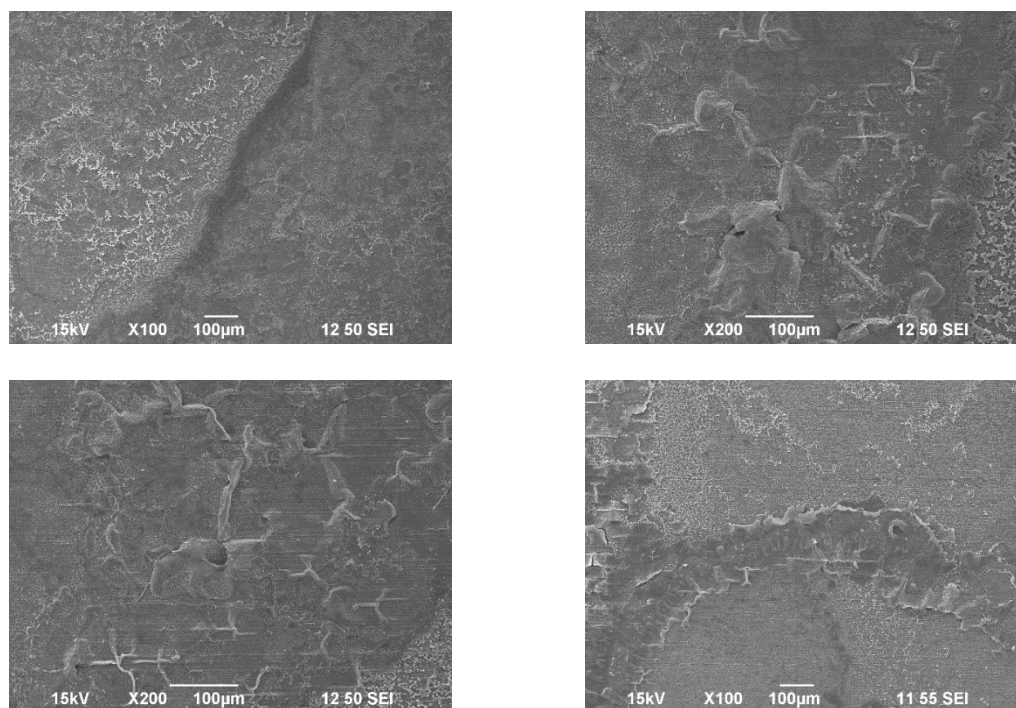


Figure 55: Conditions: p_{H₂S}: 0.3 mbar, p_{CO₂}: 0.96 bar, WCR: 0.015/0 ml/m²/s, Steel
Temperature: 25/40°C, Gas Temperature: 30°C, Duration: 3 days, Cycle Period: 1 day.

0.3 mbar H₂S – Temperature Cycling– 7 days

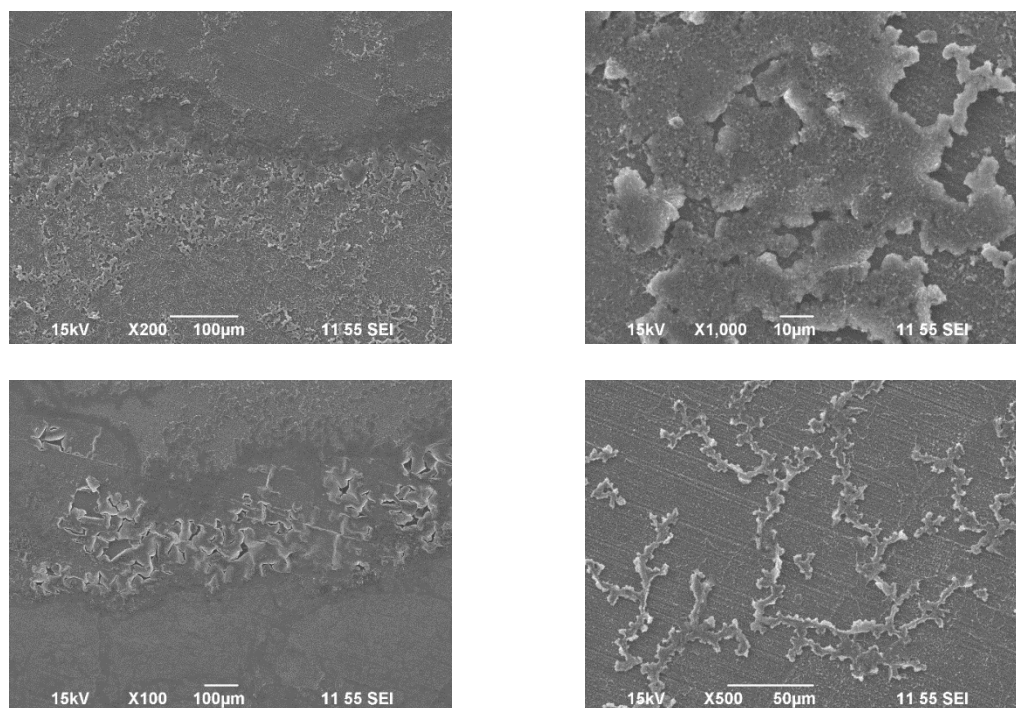


Figure 56: Conditions: p_{H₂S}: 0.3 mbar, p_{CO₂}: 0.96 bar, WCR: 0.015/0 ml/m²/s, Steel
Temperature: 25/40°C, Gas Temperature: 30°C, Duration: 7 days, Cycle Period: 1 day.

Hygroscopic Corrosion

0 mbar H₂S – 75% RH – 3 days

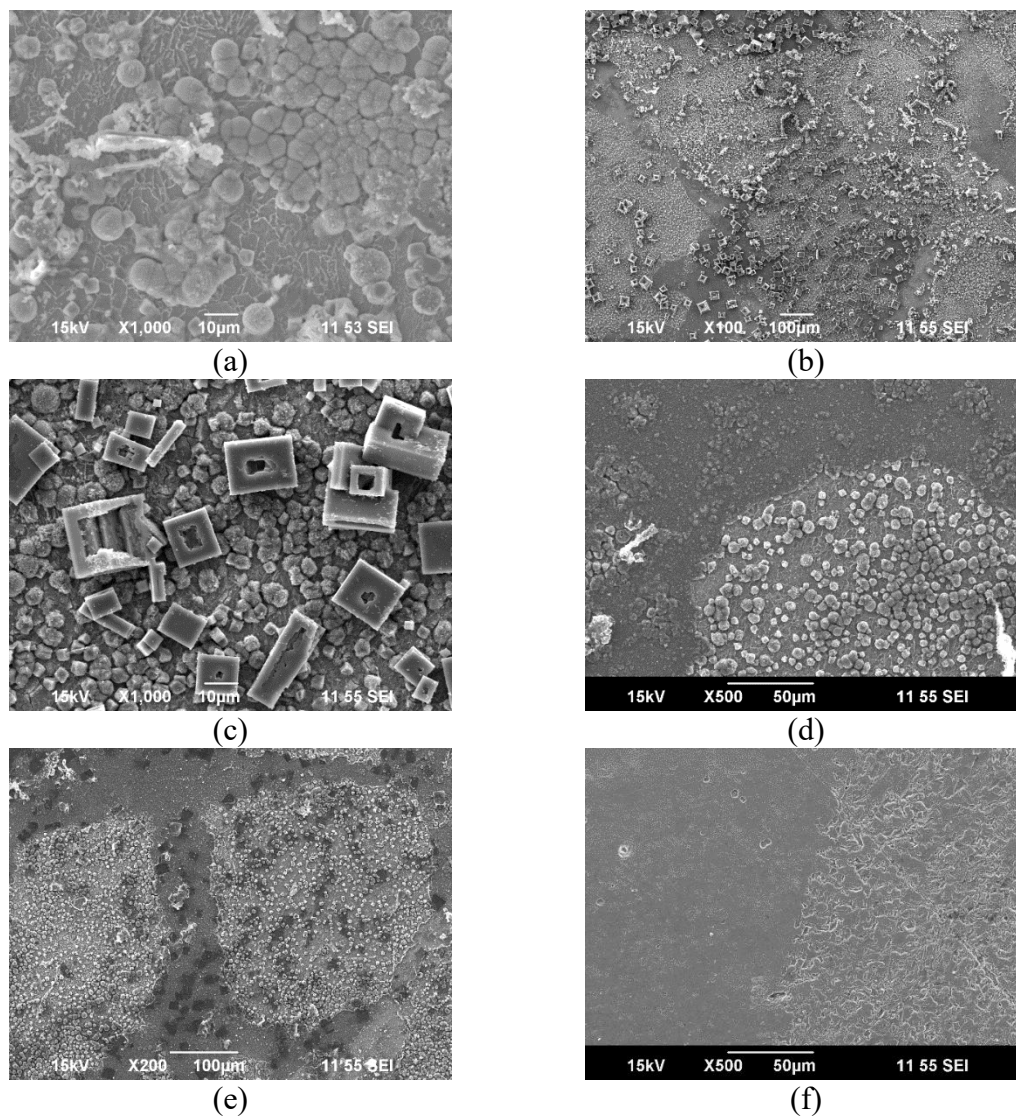


Figure 57: Conditions: pH₂S: 0 mbar, pCO₂: 0.96 bar, RH: 75%, Temperature: 25°C, Duration: 3 days, Salt Layer Composition: NaCl. (d) and (e): after DI water rinse, (f): after Clarke.

0 mbar H₂S – 58% RH – 3 days

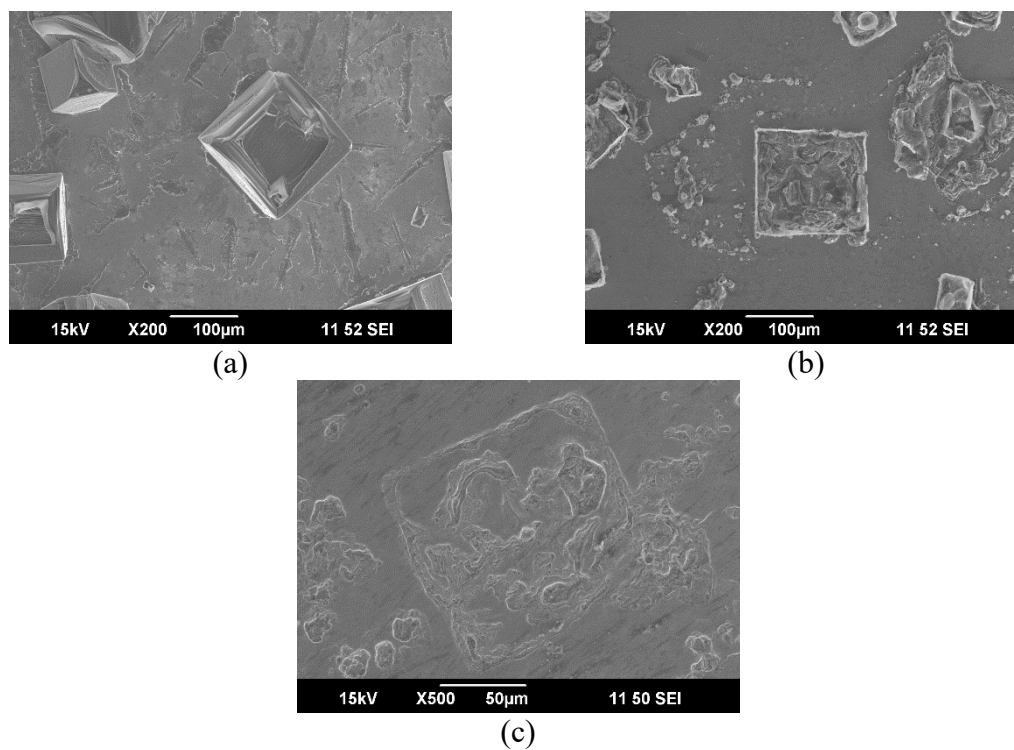


Figure 58: Conditions: p_{H₂S}: 0 mbar, p_{CO₂}: 0.96 bar, RH: 58%, Temperature: 25°C, Duration: 3 days, Salt Layer Composition: NaCl. Micrograph (a): after extraction, (b): after DI water rinse, and (c): after Clarke.

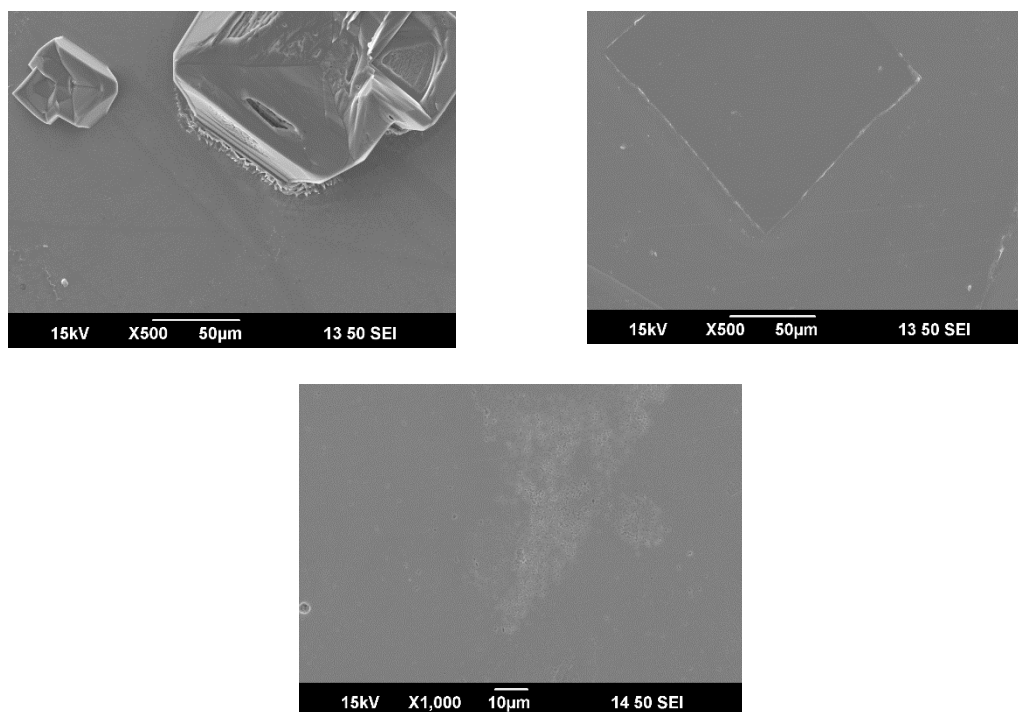
0 mbar H₂S – 33% RH – 3 days

Figure 59: Conditions: p_{H₂S}: 0 mbar, p_{CO₂}: 0.96 bar, RH: 33%, Temperature: 25°C, Duration: 3 days, Salt Layer Composition: NaCl. Micrograph (a): after extraction, (b): after DI water rinse, and (c): after Clarke.

0.1 mbar H₂S – 75% RH – 3 days

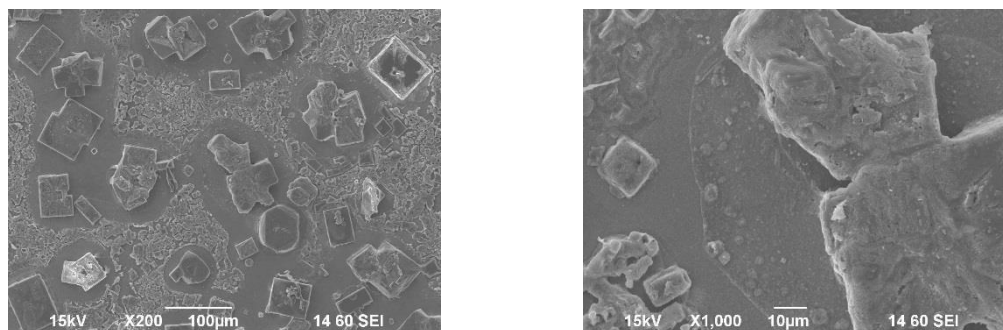


Figure 60: Conditions: p_{H₂S}: 0.1 mbar, p_{CO₂}: 0.96 bar, RH: 75%, Temperature: 25°C,
Duration: 3 days, Salt Layer Composition: NaCl

0.1 mbar H₂S – 58% RH – 3 days

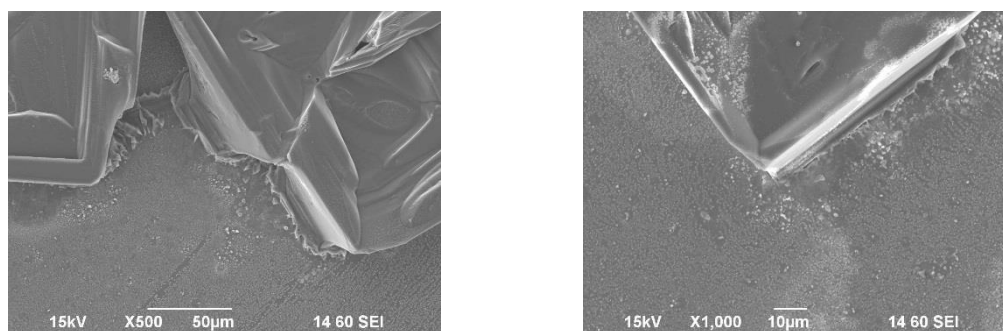


Figure 61: Conditions: p_{H₂S}: 0.1 mbar, p_{CO₂}: 0.96 bar, RH: 58%, Temperature: 25°C,
Duration: 3 days, Salt Layer Composition: NaCl.

0.1 mbar H₂S – 33% RH – 3 days

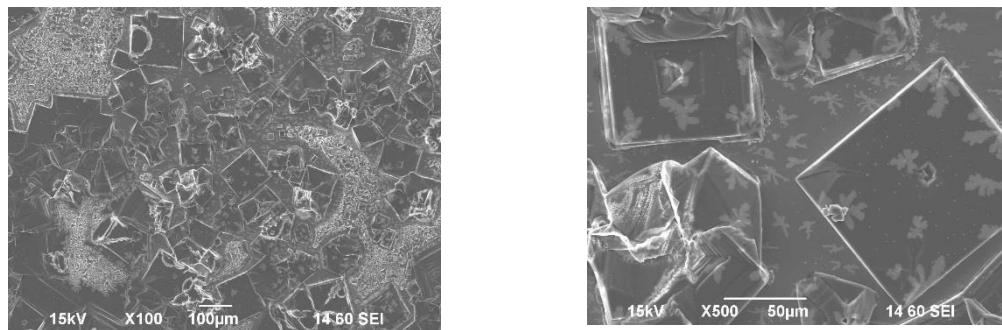


Figure 62: Conditions: p_{H₂S}: 0.1 mbar, p_{CO₂}: 0.96 bar, RH: 33%, Temperature: 25°C,
Duration: 3 days, Salt Layer Composition: NaCl.

0.3 mbar H₂S – 75% RH – 3 days

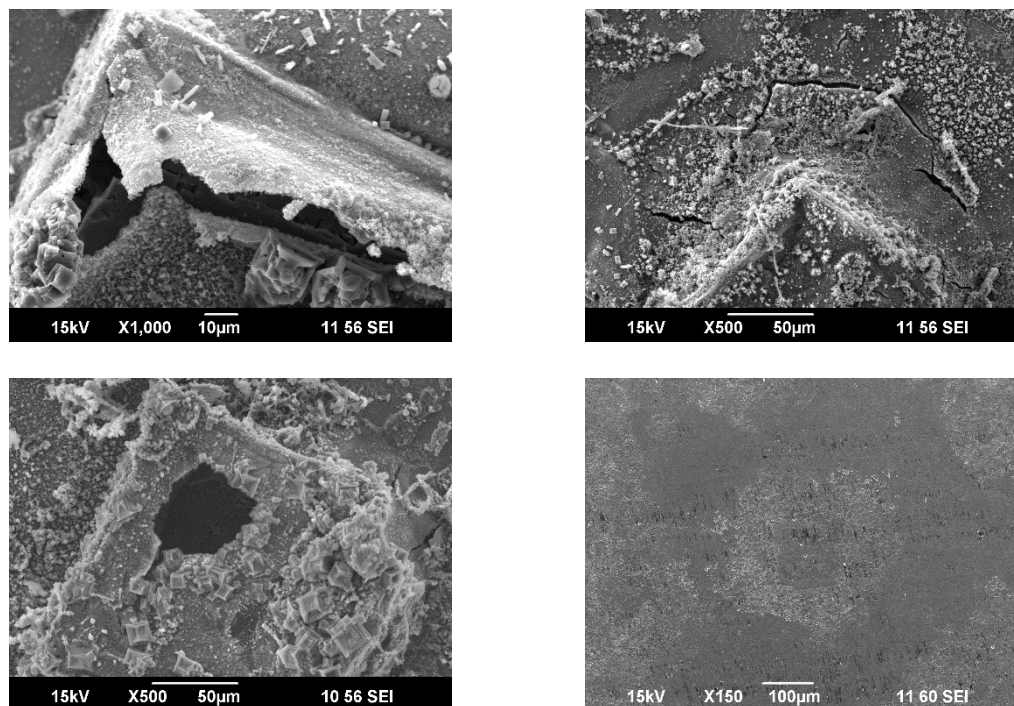


Figure 63: Conditions: p_{H₂S}: 0.3 mbar, p_{CO₂}: 0.97 bar, RH: 75%, Temperature: 25°C,

Duration: 3 days, Salt Layer Composition: NaCl.

0.3 mbar H₂S – 58% RH – 3 days

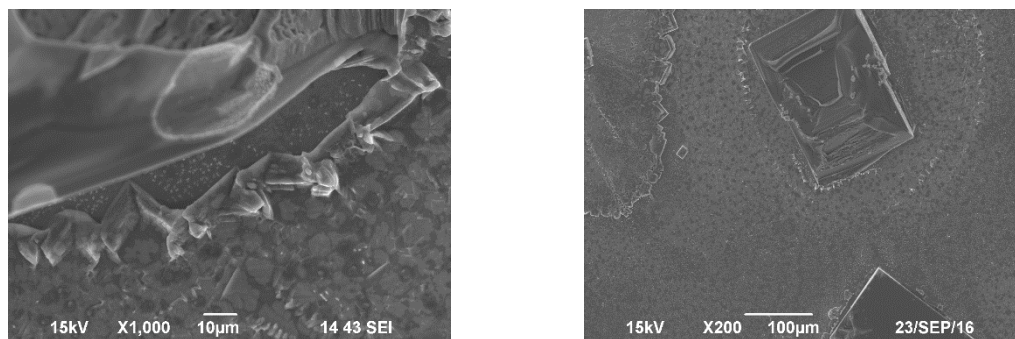


Figure 64: Conditions: pH₂S: 0.3 mbar, pCO₂: 0.97 bar, RH: 58%, Temperature: 25°C,
Duration: 3 days, Salt Layer Composition: NaCl.

0.3 mbar H₂S – 33% RH – 3 days

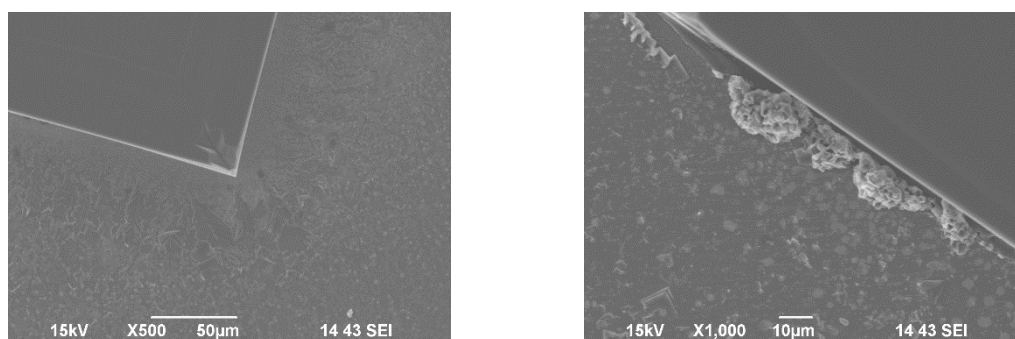


Figure 65: Conditions: pH₂S: 0.3 mbar, pCO₂: 0.97 bar, RH: 33%, Temperature: 25°C,
Duration: 3 days, Salt Layer Composition: NaCl.

1.0 mbar H₂S – 75% RH – 3 days

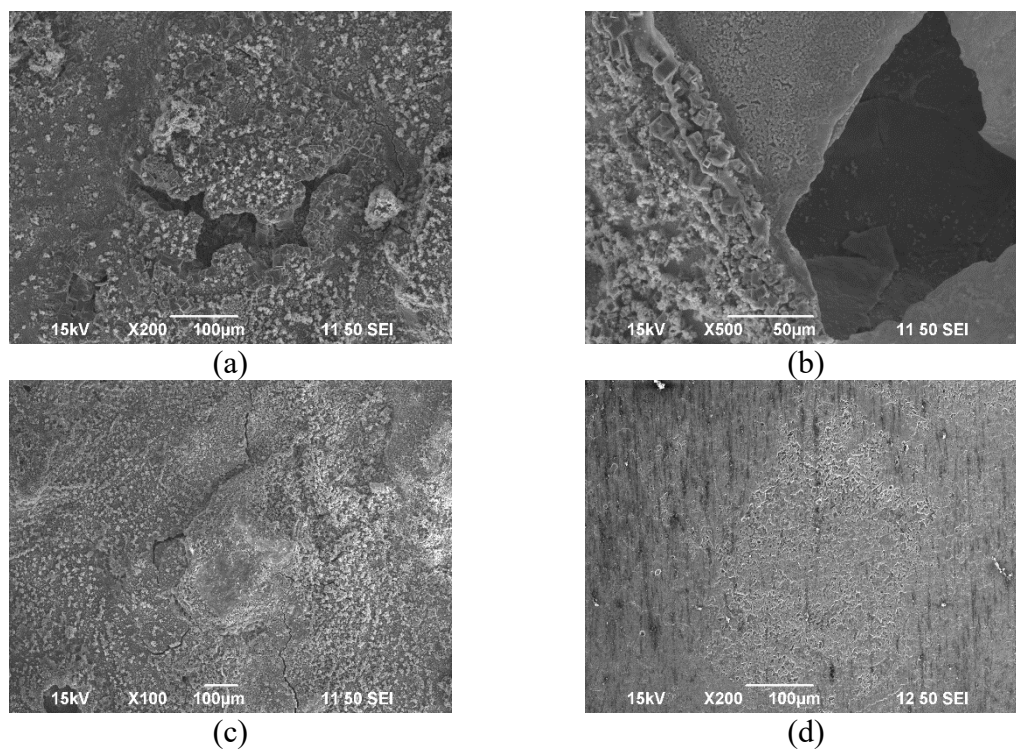


Figure 66: Conditions: p_{H₂S}: 1.0 mbar, p_{CO₂}: 0.97 bar, RH: 75%, Temperature: 25°C, Duration: 3 days, Salt Layer Composition: NaCl. (c): after DI water rinse, (d): after Clarke.

1.0 mbar H₂S – 58% RH – 3 days

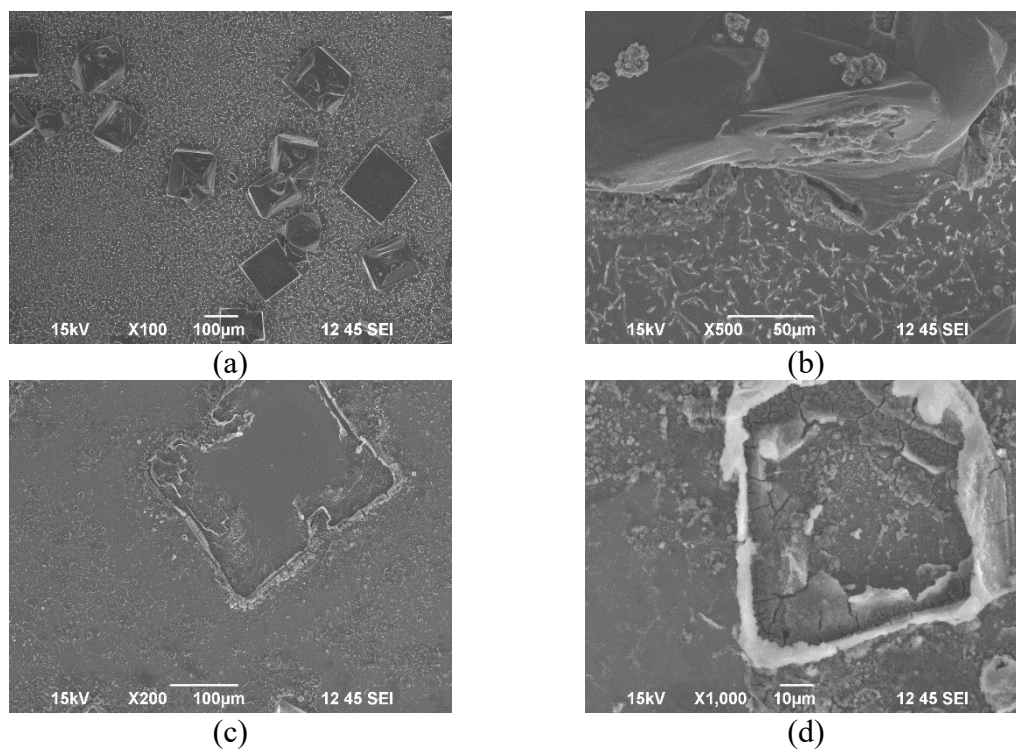


Figure 67: Conditions: p_{H₂S}: 1.0 mbar, p_{CO₂}: 0.97 bar, RH: 58%, Temperature: 25°C, Duration: 3 days, Salt Layer Composition: NaCl. Micrographs (c) and (d): after DI water rinse.

1.0 mbar H₂S – 33% RH – 3 days

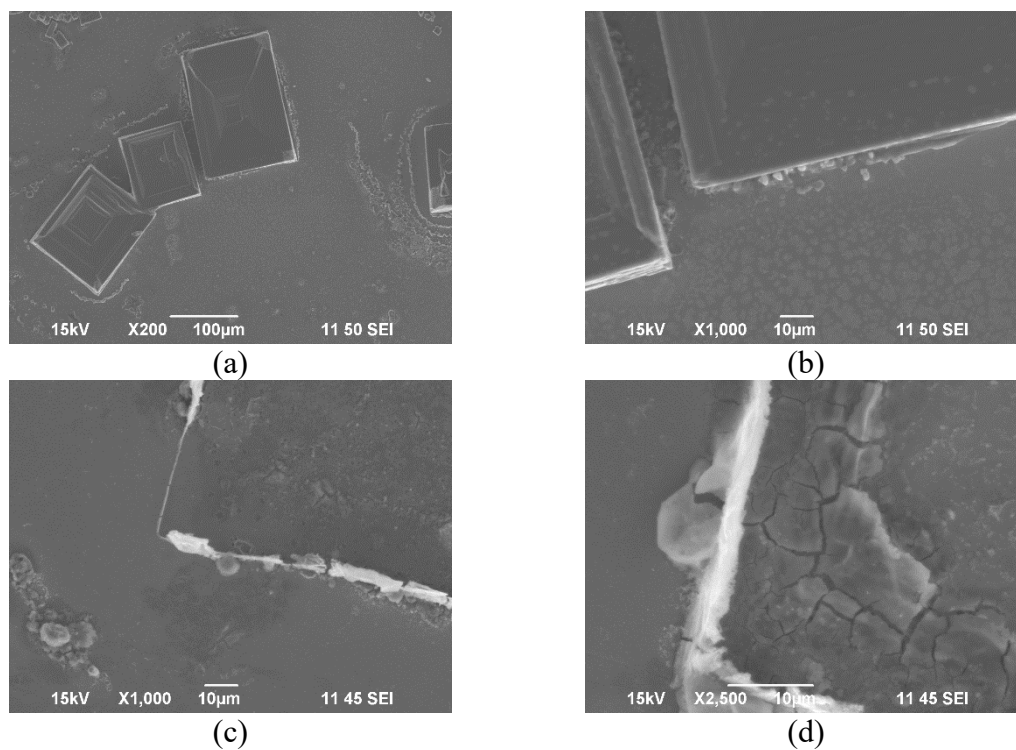


Figure 68: Conditions: p_{H₂S}: 1.0 mbar, p_{CO₂}: 0.97 bar, RH: 33%, Temperature: 25°C, Duration: 3 days, Salt Layer Composition: NaCl. Micrographs (c) and (d): after DI water rinse.



OHIO
UNIVERSITY

Thesis and Dissertation Services